

Journal Pre-proof

Noble metal-free single-atom electrocatalysts and reactor engineering for enhanced hydrogen peroxide generation via two-electron oxygen reduction reaction

Jingqin Ji, Hui Wang, Yanlan Zhao, Yan Wang, Kaifeng Wang, Yuexin Cui, Ridha Djellabi, Chuan Xia, Xu Zhao, Xiangming He



PII: S2667-1417(25)00086-2

DOI: <https://doi.org/10.1016/j.esci.2025.100456>

Reference: ESCI 100456

To appear in: *eScience*

Received Date: 23 April 2025

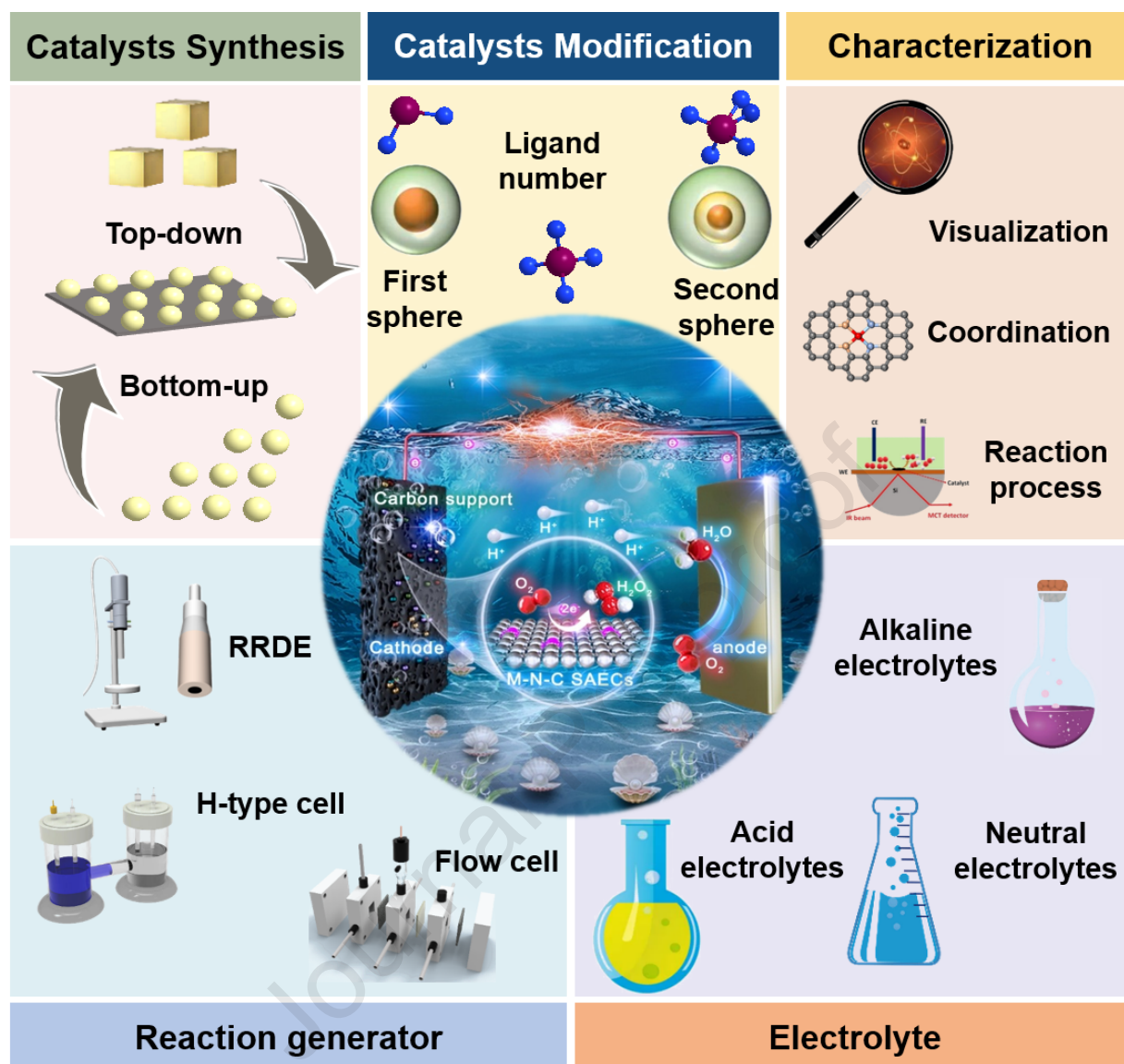
Revised Date: 13 June 2025

Accepted Date: 17 July 2025

Please cite this article as: J. Ji, H. Wang, Y. Zhao, Y. Wang, K. Wang, Y. Cui, R. Djellabi, C. Xia, X. Zhao, X. He, Noble metal-free single-atom electrocatalysts and reactor engineering for enhanced hydrogen peroxide generation via two-electron oxygen reduction reaction, *eScience*, <https://doi.org/10.1016/j.esci.2025.100456>.

This is a PDF file of an article that has undergone enhancements after acceptance, such as the addition of a cover page and metadata, and formatting for readability, but it is not yet the definitive version of record. This version will undergo additional copyediting, typesetting and review before it is published in its final form, but we are providing this version to give early visibility of the article. Please note that, during the production process, errors may be discovered which could affect the content, and all legal disclaimers that apply to the journal pertain.

© 2025 The Authors. Publishing services by Elsevier B.V. on behalf of Nankai University and KeAi.



Noble metal-free single-atom electrocatalysts and reactor engineering for enhanced hydrogen peroxide generation via two-electron oxygen reduction reaction

Jingqin Ji^{a,b,h,1}, Hui Wang^{c,1}, Yanlan Zhao^{d,h}, Yan Wang^{a,b}, Kaifeng Wang^e, Yuexin Cui^{a,b}, Ridha Djellabi^f, Chuan Xia^g, Xu Zhao^{a,b*}, Xiangming He^{h*}

^a State Key Laboratory of Environmental Aquatic Chemistry, Research Center for Eco-Environmental Sciences, Chinese Academy of Sciences, Beijing 100085, China

^b University of Chinese Academy of Sciences, Beijing 100085, China

^c College of Environmental Science and Engineering, Hunan University, Changsha 410082, China

^d College of Resources and Environmental Engineering, Guizhou University, Guiyang 550025, China

^e School of River and Ocean Engineering, Chongqing Jiaotong University, Chongqing 400074, China

^f College of Science and General Studies, Department of Chemistry, Alfaisal University, Al Takhassusi Road, Riyadh, 11533, Saudi Arabia

^g School of Materials and Energy, University of Electronic Science and Technology of China, Chengdu 611731, China

^h Institute of Nuclear & New Energy Technology, Tsinghua University, Beijing 100084, China

¹ These authors contribute equally to this article.

* Corresponding author: zhaoxu@rcees.ac.cn (X. Zhao); hexm@tsinghua.edu.cn (X.M. He).

Abstract

The generation of hydrogen peroxide (H₂O₂), a compound with diverse applications, via the two-electron (2e⁻) oxygen reduction reaction (ORR) has garnered extensive attention in both laboratory research and industrial settings. The integration of non-noble metals such as Co, Fe, Ni, Zn, Mn, Mo, or Bi into nitrogen-doped carbon (M–N–C) matrices with defined structures and active metal center sites has emerged as a promising approach for fabricating electrocatalysts for the ORR. This review uncovers the latest advancements in the development of noble metal-free single-atom electrocatalysts (M–N–C SAECs) and electrochemical reactors aimed at enhancing and stabilizing H₂O₂ production from the 2e⁻ ORR. Firstly, the review explores the basics of the ORR for H₂O₂ production and the impact of electrochemical conditions. Subsequently, the synthesis strategies and characterization methods of various M–N–C SAECs are examined in depth. In addition, the structural attributes of both conventional and altered M–N–C SAECs are meticulously investigated, and the importance of engineering and optimizing reactors to elevate H₂O₂ yields is highlighted. This review identifies the challenges and technological hurdles in bridging the gap between laboratory-scale research and practical, real-world applications.

Keywords

Hydrogen peroxide; Two-electron oxygen reduction reaction; Noble-metal-free electrocatalysts;
Single-atom electrocatalysts; Electrosynthesis

Journal Pre-proof

Abbreviations

1D	one-dimensional
$^1\text{O}_2$	singlet oxygen
2D	two-dimensional
2e^- ORR	two-electron oxygen reduction reaction
3D	three-dimensional
AC-HAADF/STEM	aberration-corrected high-angle annular dark field/scanning transmission electron microscopy
AEM	anion exchange membrane
AI	artificial intelligence
ATR-FTIR	attenuated total reflectance infrared absorption spectroscopy
CEM	cation exchange membrane
CL	catalyst layer
CNTs	carbon nanotubes
COF	covalent organic framework
DACs	diatomic catalysts
DFT	density functional theory
EDS	energy dispersive X-ray spectroscopy
EELS	electron energy loss spectroscopy
EIS	electrochemical impedance spectroscopy
EXAFS	extended X-ray absorption fine structure
FE	Faradaic efficiency
GDEs	gas diffusion electrodes
GDL	gas diffusion layer
H_2O_2	hydrogen peroxide
HER	hydrogen evolution reaction
IEM	ion exchange membrane
IR	infrared
KL	Koutecky–Levich
LCA	life cycle assessment
LMCT	ligand-to-metal charge transfer
LSV	linear sweep voltammetry
M–N–C SAECs	noble metal-free single-atom electrocatalysts
MEA	membrane electrode assembly
ML	machine learning
MOFs	metal–organic frameworks
n	transferred electrons
OER	oxygen evolution reaction
OFGs	oxygen functional groups
PEM	proton exchange membrane
RRDE	rotating ring-disk electrode
SAEC	single-atom electrocatalyst
SE	solid electrolyte
SECM	scanning electrochemical microscopy
TOF	turnover frequency
WOR	water oxidation reaction
XAFS	X-ray absorption fine structure
XANES	X-ray absorption near edge structure
XPS	X-ray photoelectron spectroscopy

1. Introduction

The increasing global demands from industrial, agricultural, and domestic sectors have imposed significant pressure on natural resources, leading to environmental degradation and economic concerns. As a result, sustainable technologies that convert waste into value-added products have gained considerable attention in green chemistry and environmental science [1–4]. One key area of research is the synthesis of hydrogen peroxide (H_2O_2), a compound with diverse applications ranging from wastewater treatment and disinfection to pulp and paper, chemical synthesis, semiconductor cleaning, aerospace technology, and even first-aid kits, as illustrated in **Fig. 1** [5–8]. Conventionally, industrial H_2O_2 is produced via the anthraquinone oxidation–reduction cycle, which relies on pressurized hydrogen, palladium catalysts, and energy-intensive distillation steps, generating chemical residues and posing logistical and safety concerns [9,10]. An alternative is decentralized H_2O_2 production using gas-phase H_2 and O_2 [11,12], but the explosion risk hinders its practical implementation.

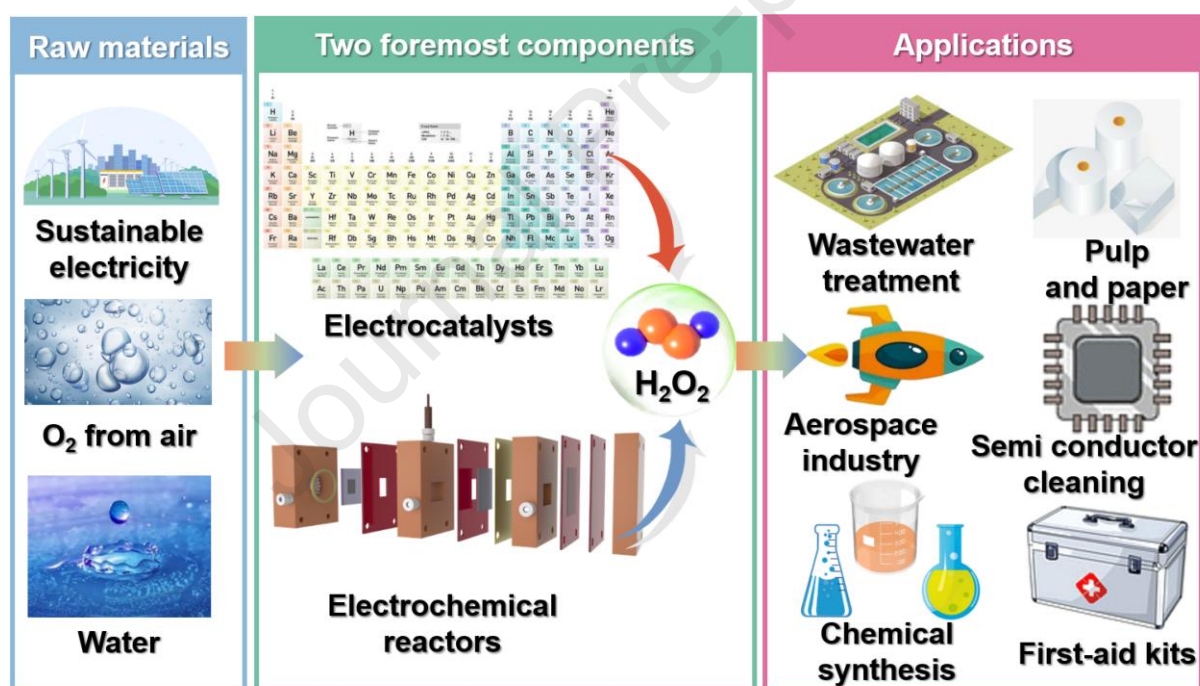


Fig. 1. The approaches for electrochemical H_2O_2 synthesis and its various applications.

In contrast, the two-electron ($2e^-$) electrochemical oxygen reduction reaction (ORR) offers a green and modular route for H_2O_2 generation under ambient conditions, using water, oxygen, and electricity as inputs [13–15]. This approach benefits from: (i) mild reaction conditions, (ii) decentralized on-demand production, and (iii) compatibility with renewable electricity. As represented in **Fig. 1**, the two foremost components of the electrocatalytic procedure, namely the electrocatalyst and electrochemical cell, have seen significant advancements leading to

recent successes in H_2O_2 electrosynthesis. Catalyst design plays a particularly pivotal role in determining ORR performance. As depicted in **Fig. 2**, considerable efforts have been devoted in recent years to the development of novel and efficient electrocatalysts. While precious metal-based systems, such as Hg-Au or Pd-based electrodes, have historically dominated H_2O_2 electrosynthesis [16–21], their high cost and limited availability impede large-scale deployment. Carbon-based materials, especially those doped with nitrogen, have garnered interest as alternatives due to their tunable electronic properties, high conductivity, and low cost [22–27]. N-doping enhances ORR activity by modifying the local electronic structure and promoting selective O_2 adsorption [28–30].

Some of the most attractive choices for the 2e^- ORR based on nitrogen-doped carbon electrocatalysts are single-atom electrocatalysts (SAECs) with atomically separated reactive sites inserted in nitrogen-doped carbon substrates with precisely structured frameworks [31–34]. Since their conceptualization in 2011 [36], SAECs have attracted attention due to their unique electronic structure, high atomic utilization, and tunable coordination environment, which collectively improve catalytic selectivity and activity [35–43]. Notably, their preference for end-on O_2 adsorption minimizes O–O bond cleavage, favoring the 2e^- ORR over the competing 4e^- pathway [44,45].

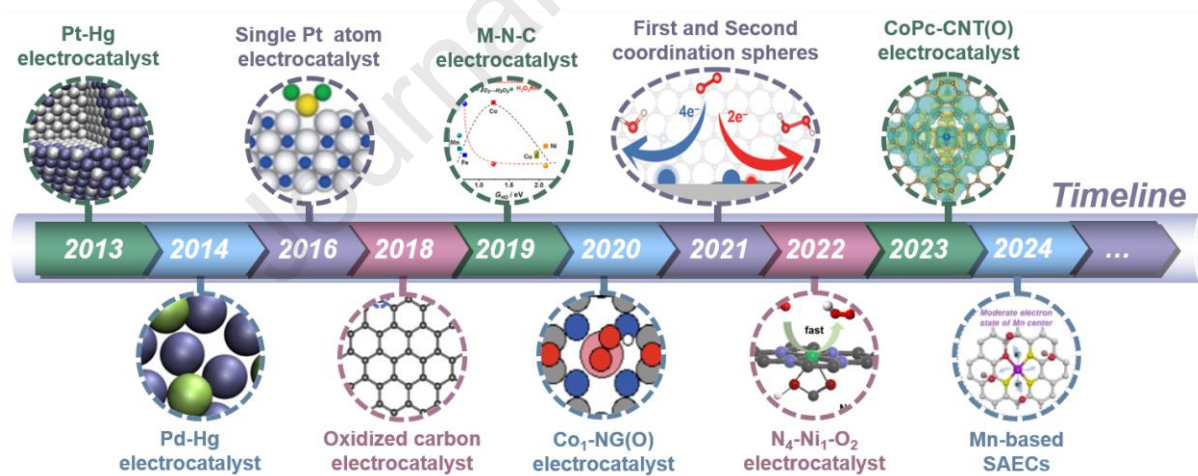


Fig. 2. Timeline showing the development of electrocatalysts for the electrosynthesis of H_2O_2 from O_2 in the last 10 years. Reprinted with permission [15], Copyright 2013, Springer Nature. Reprinted with permission [21], Copyright 2014, American Chemical Society. Reprinted with permission [46], Copyright 2016, Wiley. Reprinted with permission [23], Copyright 2018, Springer Nature. Reprinted with permission [47], Copyright 2019, American Chemical Society. Reprinted with permission [48], Copyright 2020, Springer Nature. Reprinted with permission [49], Copyright 2021, American Chemical Society. Reprinted with permission [50], Copyright 2022, Wiley. Reprinted with permission [51], Copyright 2023, Springer Nature. Reprinted with permission [52], Copyright 2024, Wiley.

While several reviews have discussed the advances in SAECs for H_2O_2 synthesis [53–57],

there has been limited exploration of the inherent correlations between the featured configuration of the electrocatalysts and the properties of M–N–C SAECs (M = non-precious metal) for the $2e^-$ ORR. Historically, precious-metal-based electrocatalysts have dominated the ORR field due to their low overpotential and stable operation at high current densities [58,59]. However, the scarcity of precious metals results in high production costs, thereby constraining their large-scale manufacture [60,61]. Conversely, the natural abundance of non-precious metals, such as Fe, Mn, Ni, and Co, offers an economical source for synthesizing M–N–C SAECs [62,63]. The catalytic efficiency of M–N–C SAECs can even exceed that of their noble metal counterparts through targeted modifications, such as regulating the coordination structure of the metal center, adjusting the higher layer coordination atoms, and introducing oxygen functional groups (OFGs) [64,65].

This review, therefore, as shown in **Fig. 3**, addresses this gap by focusing on reaction principles, synthetic strategies, characterization techniques, structure–performance correlations, electrocatalyst optimization, and device regulation in the context of M–N–C SAECs. We explore the fundamentals of direct H_2O_2 production by the $2e^-$ ORR, highlighting the engineering and optimization strategies of M–N–C SAECs at the atomic level. We also summarize the advanced characterization techniques for detecting the microstructures of M–N–C SAECs. This is followed by a thorough discussion of how the metal atomic centers, carbon substrates, and coordination environments of M–N–C SAECs affect their behavior for the $2e^-$ ORR, along with strategies for fine-tuning microstructures. Given the critical role of electrochemical reactors in the ORR process, the latest advancements in reactor setup to boost H_2O_2 generation are also comprehensively summarized. Finally, we critically address the main technology issues and challenges in terms of materials design and reactors, to promote the transfer of this class of processes to real-world applications.

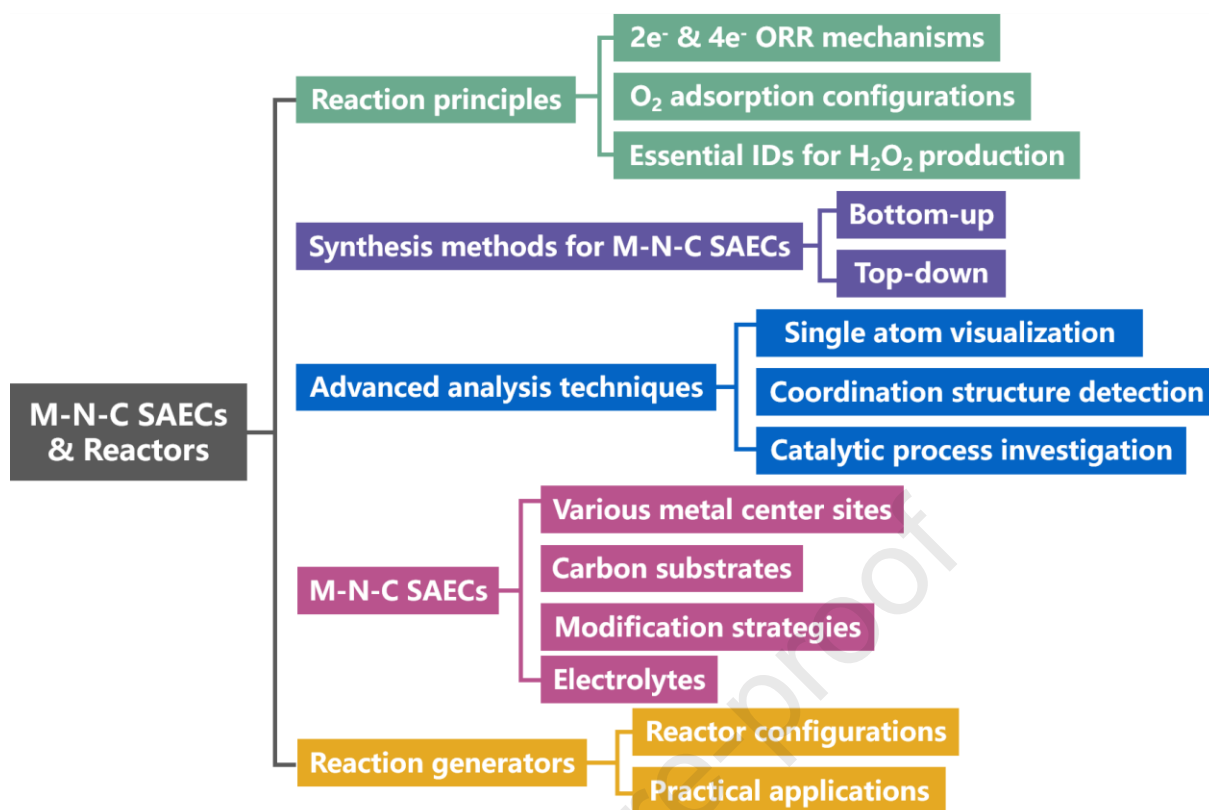


Fig. 3. The main content of this review (reaction principles, synthesis approaches, analysis techniques, various M–N–C SAEs, and reaction generators).

2. Understanding of H₂O₂ electrochemical production mechanisms

2.1. Principles of H₂O₂ generation via 2e[−] ORR

The interactions and adsorption/desorption dynamics of mediators at the reactive sites are essential for ORR properties. In general, the ORR follows either a dissociation or a binding pathway, as depicted in **Fig. 4**. On conventional enclosed metallic interfaces like Pt nanoparticles, the O–O bond breaks as O₂ attaches to separate reactive metal sites, allowing a dissociation pathway [66]. By comparison, the M–N–C SAEC is composed of atomically isolated metal sites without contiguous reactive sites, making the binding pathway more favorable geometrically [67]. The ORR path relies on whether the O–O bond remains intact, following either the 4e[−] process to generate OH[−]/H₂O or the 2e[−] route to produce OOH/H₂O₂ [68–70]. Normally, a longer retention duration is ideal for the 4e[−] ORR. Conversely, attenuated adsorption favors H₂O₂ production by promoting the desorption of OOH* [67]. As a result, preserving the O–O bond is crucial for producing H₂O₂ [71–73]. Engineering the most favorable reactive site to modulate interactions with oxygenated products is vital for the 2e[−] ORR; doing so relies on the specific local coordination of the metallic sites, such as the employed electrode

potentials, and the electrolyte pH. The equations for the formation of H_2O_2 in media of various pHs are as follows [13]:

In acidic solutions



In alkaline solutions



Water oxidation reaction (WOR):

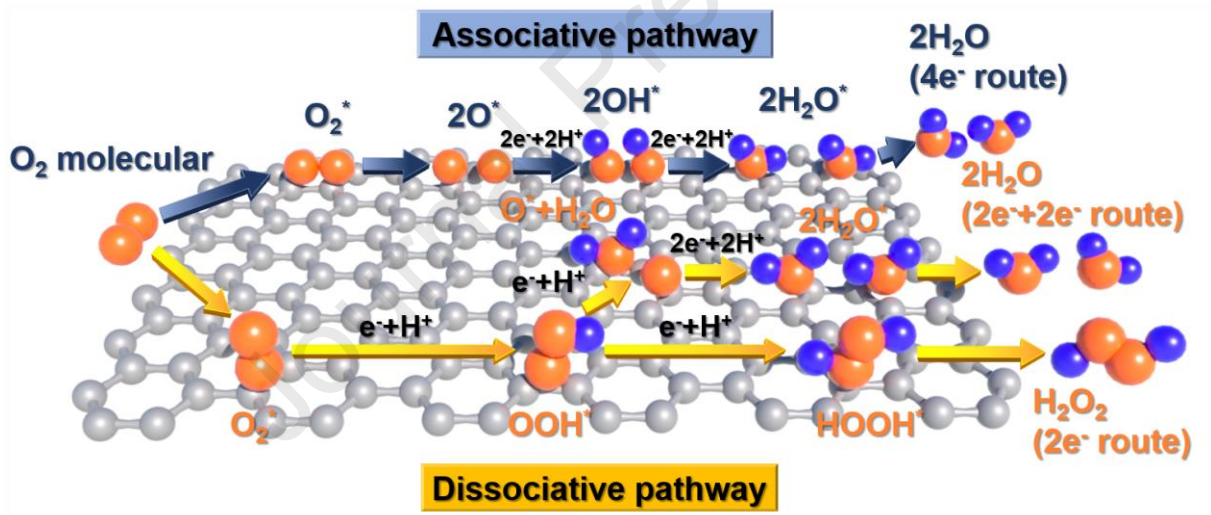


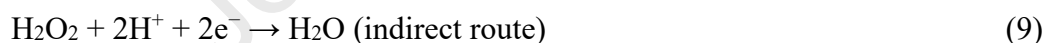
Fig. 4. ORR process via dissociative or binding pathways.

The 2e^- ORR for the generation of H_2O_2 involves two combined electron–proton transitions and a reactive agent (OOH^*) [74]. In acidic solutions, the process begins with O_2 moieties attached to the reactive sites, reaching protons and electrons to produce OOH^* , as shown in **Equation (1)**, then being transferred to form H_2O_2 , as shown in **Equation (2)**. In contrast, in alkaline conditions, H_2O_2 undergoes hydrolysis to form HO_2^- , as shown in **Equation (5)**. The persistence of H_2O_2 in aqueous environments is pH-dependent, with H_2O_2 exhibiting greater stability in acidic conditions than in alkaline ones [13]. This pH sensitivity reflects the protons' preference for binding to either the previous or the following oxygen atom

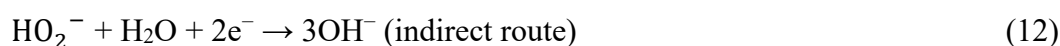
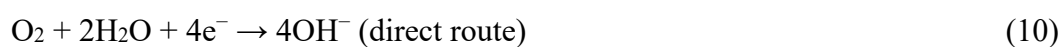
in the OOH^* complex. For instance, in single cobalt atomic catalysts, a lower potential facilitates the attachment of protons to the former O, thus enhancing H_2O_2 selectivity. By comparison, in some electrocatalysts, the proton favors the latter O, diminishing H_2O_2 selectivity in acidic environments [75]. The choice of pH environment should also consider the downstream application requirements. In summary, an optimal $2e^-$ catalyst ought to exhibit maximal sorption of O_2 and detachment of OOH^* to guarantee ideal reactivity, while minimizing the breakdown of OOH^* into O^* and OH^* . Notably, H_2O_2 can also be electrochemically generated through the $2e^-$ WOR, as shown in **Equation** (6), though this method is less feasible due to the inherent instability of H_2O_2 during the WOR [76].

In the fuel cell field, the $4e^-$ ORR has been the major focus for decades [77–79]. In the $4e^-$ ORR, the oxygen moiety undergoes electrochemical reduction through the intake of four protons and electrons, resulting in the formation of water and the simultaneous production of an electrical potential [67]. The $4e^-$ ORR procedure can proceed either directly via a four-electron route at one specific site ($\text{O}_2/\text{H}_2\text{O}$) or indirectly through two different sites ($\text{O}_2/\text{H}_2\text{O}_2/\text{H}_2\text{O}$), involving the desorption of H_2O_2 intermediates, as depicted in **Fig. 4**. Both pathways ultimately lead to the same result. In addition, the $4e^-$ ORR routes are different in acidic and alkaline solutions, as described in **Equations** (7)-(12) [80].

In acidic solutions



In alkaline solutions



2.2. Oxygen adsorption geometry configurations

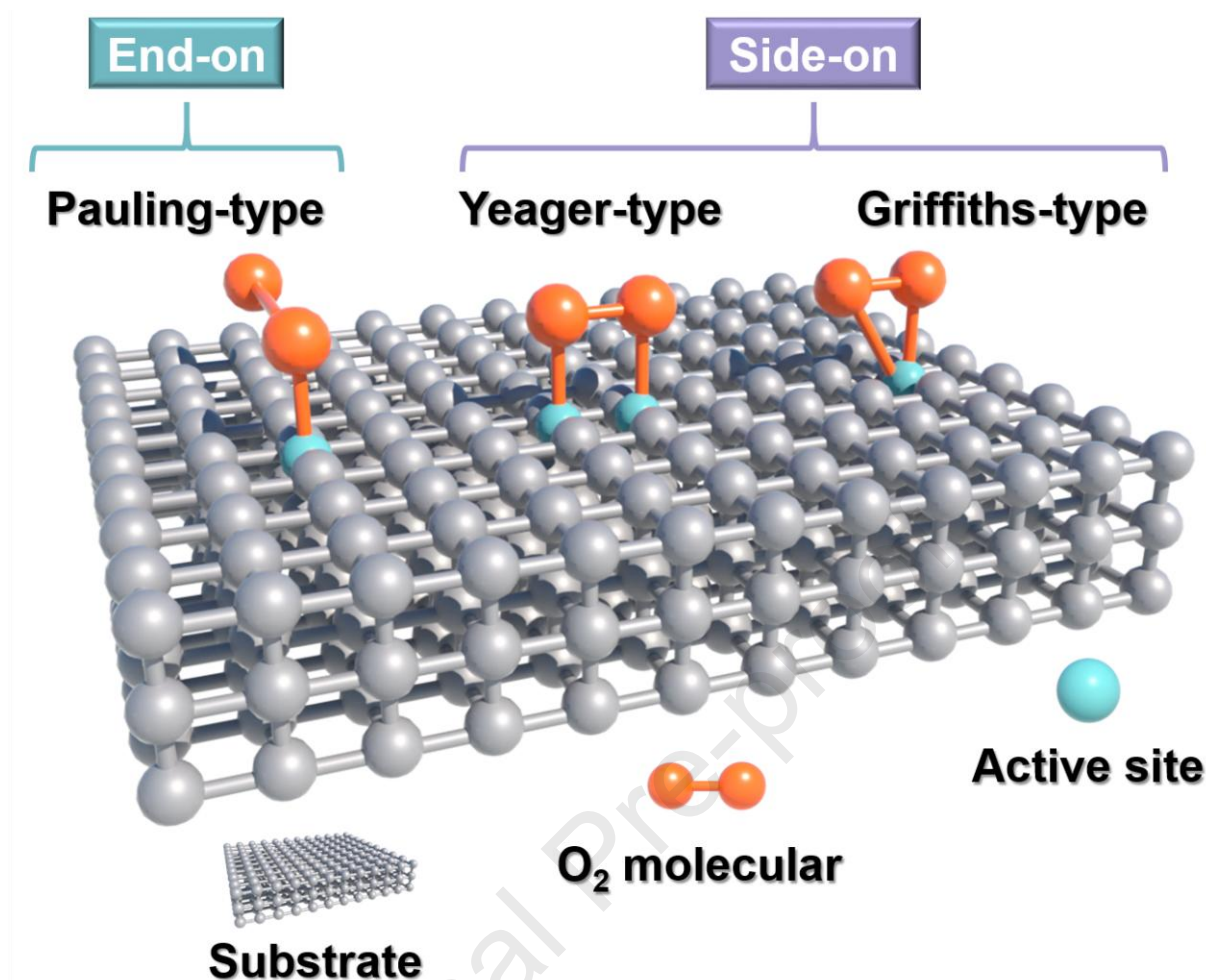


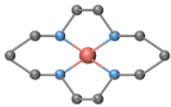
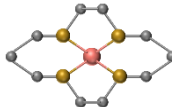
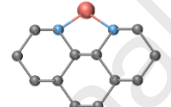
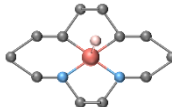
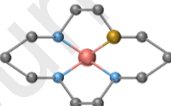
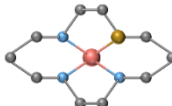
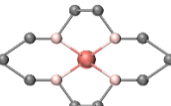
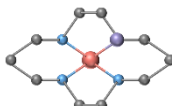
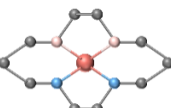
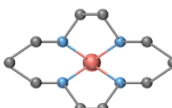
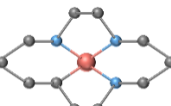
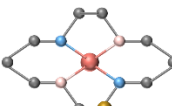
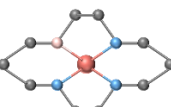
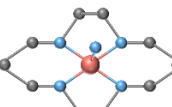
Fig. 5. Three representative O₂ adsorption configurations on active sites.

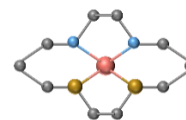
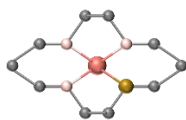
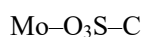
Oxygen sorption patterns, O–O bond lengths and catalytic behaviors rely strongly on the configurations of reactive sites, making the geometrical constituents of the reactive sites vital for the 2e[−] ORR. Typically, as presented in **Fig. 5**, non-dispersed metallic reactive centers show two architectural O₂ adhesion conformations: Griffiths-type and Yeager-type. The Griffiths-type conformation involves the sorption of O₂ by a sole metallic center, while the Yeager-type features the sorption of O₂ by two adjacent metallic centers [44,81]. However, these adsorption models are unfavorable for the conversion of O₂ to H₂O₂. Interestingly, the Pauling-type O₂ sorption configuration, which is less adsorptive and more suitable for the 2e[−] ORR, was noted in SAECs [44]. As the metal reactive sites are scattered at the atomic scale, the likelihood of O–O bond breakage is markedly reduced, highlighting the inherent advantage of SAECs in 2e[−] ORR-mediated H₂O₂ production [45].

The types of O₂ adsorption are heavily influenced by the structures of M–N–C SAEC supports. Various models incorporating a carbon-embedded Fe–N₄ (shown in **Table 1**) fraction

have been put forward to elucidate the variations in ORR properties observed among Fe–N–C SAECs [82]. A variety of substrates would lead to distinct O₂ adsorption configurations, despite having the same active sites. Density functional theory (DFT) calculations indicated that as the surrounding Fe–N₄ carbon atoms decreased, the incorporation intensity of O₂ increased, leading to a side-on adsorption conformation. The incorporation intensity and O₂ adhesion conformation could be forecasted by studying the arrangement of Fermi levels around the Fe non-bonding d-orbitals. This predictive insight could offer directions for the engineering of M–N–C SAECs. To conclude, enhancing selectivity is not limited to the traditional method of modulating OOH* intermediates but can also be accomplished via geometric modifications. Thus, a thorough comprehension of catalytic structures is crucial for the informed engineering of M–N–C SAECs with desired catalytic properties.

Table 1. Different coordination configurations of central metals and their structural schematic diagrams.

Configuration	Structural schematic	Configuration	Structural schematic
Fe–N ₄		Mo–S ₄ –C	
Co–N ₂		O–Co–N ₂ C ₂	
FeN ₃ S ₁		Co ₁ S ₁ N ₃	
Co–O ₄		Co ₁ P ₁ N ₃	
Ni–N ₂ O ₂		Co ₁ N ₁ N ₃	
ZnO ₃ C		Zn–N ₂ O ₂	
Zn–N ₃ O		Co–N ₅	



Red ball: central metal atom; Blue ball: N atom; Pink ball: O atom; Yellow ball: S atom; Purple ball: P atom.

2.3. Essential identities used for H_2O_2 generation via 2e^- ORR

It is essential to ascertain the efficiency of H_2O_2 generation to evaluate catalytic performance accurately. The internal parameters for evaluating ORR efficiency include turnover frequency (TOF), overpotential, and turnover number [45]. The recommended method for comparing H_2O_2 production activity is to consider the TOF value, as it represents the activity of each reactive site under certain reaction conditions [81,83]. In addition, the production of H_2O_2 is intricately controlled by the kinetics of the reaction. To determine the kinetic current density for H_2O_2 production, it is necessary to adjust for mass-transport restrictions using the Koutecky–Levich (KL) formula [84–86]. The overall efficiency is further influenced by thermodynamic efficiency, quantified as the ratio of the Gibbs energy change to the enthalpy change in the complete cell reaction [45].

Selectivity is a pivotal concern in catalytic reactions involving multiple pathways. For H_2O_2 production, selectivity is commonly reported in two distinct manners: Faradaic efficiency (FE), as illustrated in **Equation (13)**, and molar fraction. The former is computed using H-type cell or flow cell analysis, representing the percentage of charge transformed to H_2O_2 over the total charge passed [87]. The latter is commonly expressed as the molar fraction, a definition often established through measurements conducted by a rotating ring-disk electrode (RRDE) [23]. Wang et al. [88] proposed distinct definitions for two selectivity types. Their reported data indicated variations in these definitions, and they introduced an equation (see **Equation (14)**) to express the relationship between molar fraction and FE. The result emphasized the significance of reporting FE as H_2O_2 selectivity over molar fraction, due to its enhanced ability to reflect the catalyst's selectivity more accurately.

The quantity of transferred electrons (n) stands as a significant parameter in the ORR, not only serving as an indicator of oxygen conversion efficiency but also offering insights into the principles of ORR. The n value is the average number of electrons ultimately acquired by an O_2 molecule during the ORR. Throughout the ORR process, an O_2 molecule can acquire either two or four electrons, resulting in the formation of H_2O_2 or H_2O (as HO_2^- and OH^- in alkaline electrolyte). In practical terms, a low n value paves the way for an economical and secure

method to generate H_2O_2 [74,89,90]. Typically, there are two commonly employed experimental techniques for determining n : the RRDE method and the KL method. Through the RRDE test, n can be calculated from **Equation** (15). Qiao's group[91] discovered a correlation between n and angular velocity, highlighting substantial disparities in results between the KL and the RRDE method. Their mathematical modeling indicated that the KL approach was ill-suited for identifying the number of electrons shifted in the ORR, given the complex, multi-step nature of the reaction. The study underscored the reliability of the RRDE method, emphasizing the importance of calibrated collection efficiency and using a suitable ring electrode to ensure reliability from both theoretical and experimental perspectives.

There are many methods to determine the concentration of H_2O_2 in solution, the most used of which is the cerium sulfate $[\text{Ce}(\text{SO}_4)_2]$ titration technique. A yellow solution of Ce^{4+} will be reduced by H_2O_2 to colorless Ce^{3+} , per **Equation** (16) [23,92]. The measurement of Ce^{4+} concentration is conducted both before and following the addition of H_2O_2 , with the concentration of H_2O_2 being identified based on the moles of H_2O_2 present: $M(\text{H}_2\text{O}_2) = 2M(\text{Ce}^{4+})$, where $M(\text{Ce}^{4+})$ represents the moles of Ce^{4+} utilized. Besides the $\text{Ce}(\text{SO}_4)_2$ titration approach, the H_2O_2 concentration can alternatively be determined using potassium titanium oxalate [93], potassium permanganate titration [76,94], and iodometric titration [95,96].

$$\text{FE} = \frac{\text{Generated } \text{H}_2\text{O}_2}{\text{Theoretical generated } \text{H}_2\text{O}_2} \times 100\% \quad (13)$$

$$\text{Molar fraction} = \frac{2\text{FE}}{1+\text{FE}} \times 100\% \quad (14)$$

$$n = \frac{4I_D}{I_D + I_R/N} \quad (15)$$



In the foregoing, I_R represents the current of the ring, I_D denotes the current of the disk, and N signifies the collection efficiency in the RRDE.

3. Approaches to synthesize M–N–C SAECs for H_2O_2 generation

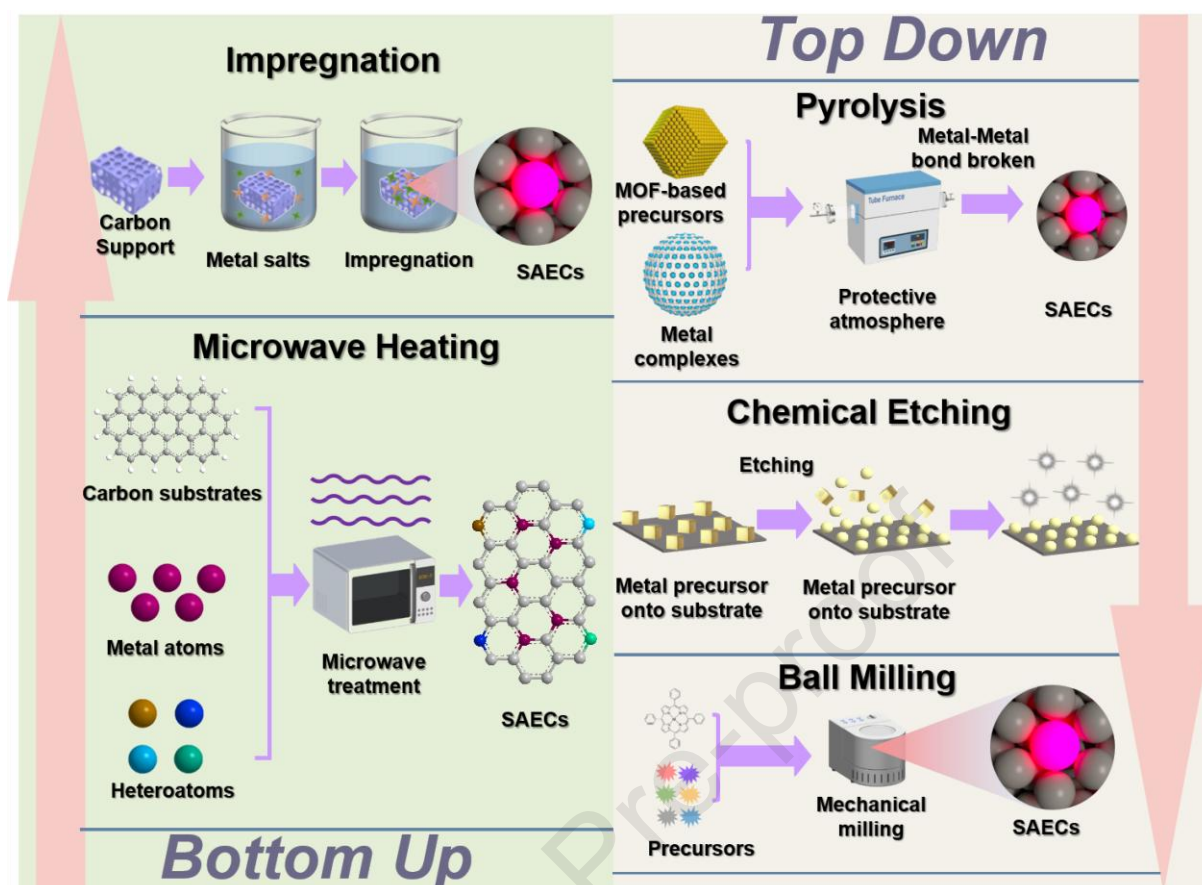


Fig. 6. Synthetic methods for M-N-C SAEs: bottom-up and top-down strategies.

Achieving the atomic-level dispersion of metal species generally requires maintaining an adequate interatomic distance. Over the years, numerous studies have explored various synthesis pathways to engineer M-N-C SAEs, as shown in Fig. 6, which categorizes them into two main types: bottom-up and top-down methods [97,98]. In the bottom-up approaches, precursors adhere to solid matrices through methods like immersion and then undergo reduction to form SAEs. This technique encompasses various processes, such as hydrothermal reactions, impregnation, and microwave-assisted methods. In contrast, top-down approaches generally involve the employment of nanoparticles anchored on a substrate or bulk metal as primary precursors, then converted to individual atoms under certain circumstances, such as pyrolysis and mechanical force [99]. Distinct from the $4e^-$ ORR, enhancing the selectivity towards the $2e^-$ ORR necessitates the suppression of O-O bond cleavage. Consequently, as shown in Fig. 7, during the synthesis processes for M-N-C SAEs, precursor concentration critically governs the ORR pathways. Decreased metallic precursor concentrations enhance atomic dispersion across substrates, favoring the end-on O_2 adsorption that preserves O-O bonds and promotes the $2e^-$ ORR route. Conversely, elevated precursor levels induce side-on O_2 adsorption

configurations, triggering O–O bond cleavage and the $4e^-$ pathway [100].

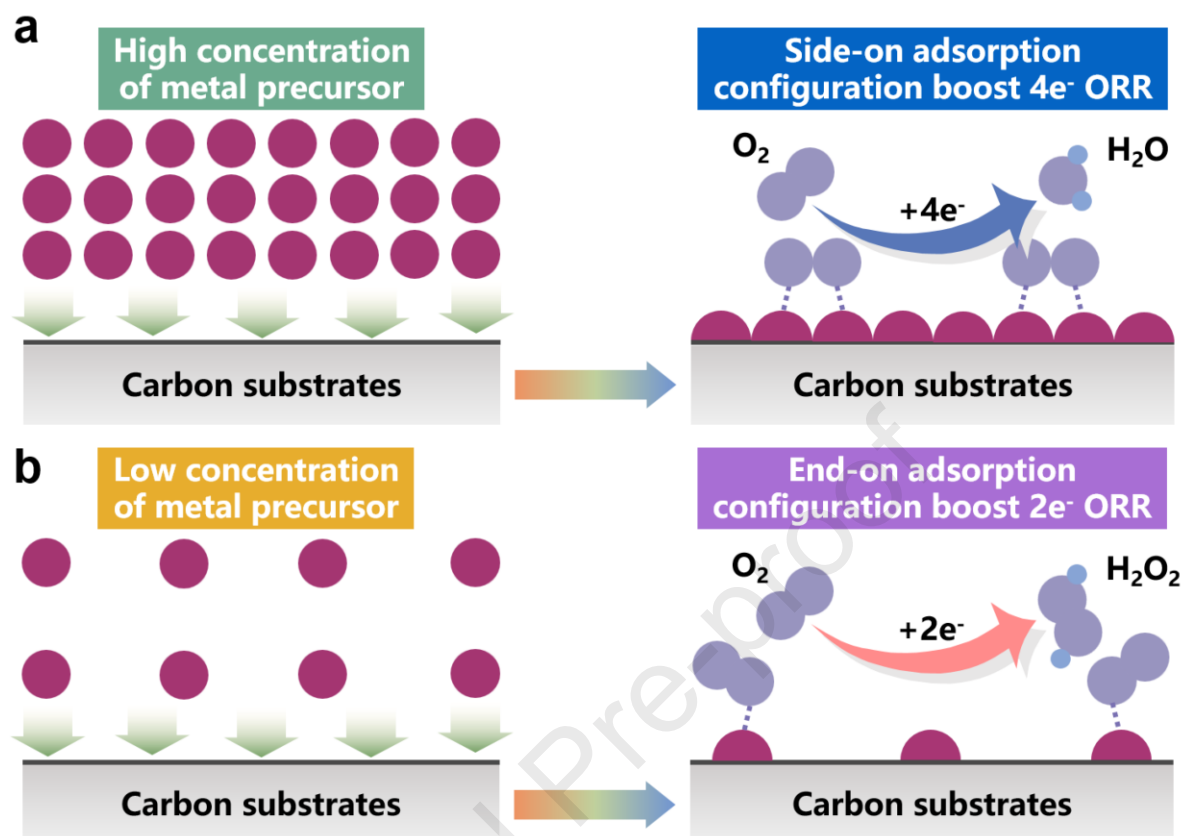


Fig. 7. (a) A high concentration of metal precursor facilitates the side-on adsorption configuration of O_2 to boost the $4e^-$ ORR. (b) A low concentration of metal precursor facilitates the end-on adsorption configuration of O_2 to boost the $2e^-$ ORR.

3.1. Bottom-up approaches

In the bottom-up synthesis approach, the starting precursors are selected from mononuclear metal complexes. Two direct and effective methods to meet this objective are significantly reducing the metal loading or selecting a suitable substrate with a high surface area to increase the interatomic spacing of the metal atoms [101]. For SAECs with high metal loading content, there are several methods to avoid the movement and clustering of individual metal sites. For instance, heteroatoms (like N, P, and S) with unshared electron pairs exhibit a robust coordination ability with metallic species. These atoms behave as ligand sites for the attachment and anchoring of mononuclear metallic complexes as well as for the resulting individual metallic atoms [102–104]. Another strategy for the synthesis of SAECs is to properly engineer defects on the carriers. Such defects on the substrates can influence the neighboring ligand circumstances, creating vacancies and unsaturated ligand sites, and these features can be used to trap mononuclear metal complexes [105–107]. Simultaneously, defects can stabilize

individual metal atoms through robust electron-transfer reactions [108,109]. When designing defects for SAECs, it is crucial to determine the specific types of defects. Additionally, reducing the thermal motion of metal atoms is beneficial, as it helps prevent their movement and aggregation, thereby contributing to the favorable synthesis of SAECs [110]. Consequently, significant advancements have been achieved in preparing SAECs by freezing metal precursors and generating SAECs at low temperatures.

3.1.1. Impregnation strategy

The impregnation technique, a widely used method, involves immersing support materials into a metal salt solution, then removing the excess solution. The catalyst is subsequently obtained through drying, calcination, and activation. In this bottom-up approach, the target metal species initially adheres to the support's surface, particularly at defect sites [111–113]. Following this, the metal gradually permeates the support, establishing ligand bonds with chalcogen atoms. The final count of single atoms is influenced by various factors, such as the impregnation temperature, duration, precursor concentration, and the surface area of the substrate [114]. The impregnation method is valued for its simplicity, mild reaction conditions, and universal applicability [115]. Enlightened by theoretical investigations, Tian et al. [116] synthesized the atomic dispersion of cobalt on a carbon substrate through a straightforward impregnation–calcination method with the aid of ligands. The catalysts demonstrated 95% selectivity, achieving a H_2O_2 generation rate of $1.72 \text{ mol g}_{\text{cat.}}^{-1} \text{ h}^{-1}$ with a FE exceeding 90%.

3.1.2. Microwave heating strategy

The microwave heating technique represents an innovative bottom-up approach for the preparation of SAECs. It streamlines the acceleration of chemical reactions, enabling the direct synthesis of nanomaterials or single-atom structures from molecular precursors [111]. This method stands out for its efficacy in producing nanoscale materials, due to its time-saving nature and the minimal occurrence of side reactions [117]. Duan et al. [118] developed an innovative microwave strategy that enables the rapid production of Co–N–C SAECs on nitrogen-doped graphene within a mere two seconds. This expeditious microwave process triggers the simultaneous occurrence of graphene oxide reduction, nitrogen incorporation, and transition metal introduction. The microwave thermal shocking approach has also emerged as a favored method for electrocatalyst synthesis with atomically dispersed metals. Gong et al. [119] utilized a one-step microwave heat shock approach to synthesize Co–N–C SAECs with a low-

coordinated Co–N–C structure. The resulting Co–N–C SAECs have Co–N₂ structures (shown in **Table 1**), along with numerous epoxy moieties. These electrocatalysts exhibited outstanding properties for H₂O₂ production, with 91.3% selectivity and an onset potential as high as 0.8 V.

In short, for the synthesis of M–N–C SAECs through the bottom-up approach, the following key factors should be considered: (i) Selecting appropriate mononuclear metal complexes as metal precursors, based on their support properties; (ii) implementing effective methods to spatially separate mononuclear metal complexes and hinder mobility; and (iii) ensuring robust interactions or intensive electron transfer among the resulting single metallic atoms and the ligand atoms from the substrate to secure the stability of the M–N–C SAEC.

3.2. Top-down approaches

In contrast, the fundamental goal of the top-down strategy is to sever the metal–metal ligands, thereby releasing atomically dispersed metal species. Following this, a sturdy new bond is forged between the newly liberated metal atoms and the substrate's anchoring sites. The liberation of atomically dispersed metal particles from metallic nanoparticles or bulk metal surfaces generally requires substantial energy, which intensifies the thermal motion of the metallic species and supplies the necessary energy to break the existing metal–metal bonds [120–122].

3.2.1 Pyrolysis strategy

Elevated-temperature pyrolysis stands out as a highly efficient top-down method for creating M–N–C SAECs [123–125]. Based on variations in precursors, these techniques can be categorized into two main groups: (1) pyrolysis of targeted metal-containing compounds, predominantly metal–organic framework (MOF)-based precursors; and (2) pyrolysis of non-uniform metal-containing compounds, metal-containing organic polymers, and blends of metal and carbon resources. In the pyrolysis procedure, the careful selection of temperature and injected gases is essential. In a representative synthesis procedure, the precursor usually involves metals (e.g., Co, Fe, Ni), carbon components, and dopant or ligand atoms (e.g., N, S). These mixtures are often processed in protective environments such as N₂ and Ar. It is also crucial to consider the proper processing atmosphere. A favorable choice is oxidizing environmental conditions, as this is preferable for developing volatile metal oxides [126,127]. A flowing ammonia atmosphere promotes the formation of volatile metal complexes with ammonia on the metallic nanoparticles or massive metal surfaces through robust Lewis acid

interactions [128,129]. These features are essential for trapping mobile atomically distributed metallic particles and establishing robust interactions among the metal atoms and the ligand sites, thereby suppressing agglomeration [127].

3.2.2. Chemical etching strategy

Chemical etching represents a practical and direct top-down technique for redistributing nanoparticles on carbon substrates as individual atoms, embedding larger clusters onto the substrate before dispersing them as single atoms [130]. The process for preparing M–N–C SAECs through chemical etching involves a series of steps. Initially, the metal precursors are spread onto the substrate, ensuring an even distribution of the metal across the support. Following this, the deposited material undergoes chemical etching in a controlled setting with a specific chemical etchant, such as an acid or oxidizing agent. This step selectively eliminates atoms from the metal precursor, leaving behind single atoms anchored to the support's surface. After etching, a thorough cleansing removes any residual etchant and byproducts, which is crucial for the catalyst's purity and stability [131,132]. Hu and co-workers [133] prepared Co–N–C SAECs featuring exclusively edge-hosted Co–N₂ configurations through oxidative etching to obtain a microporous configuration rich in Co–N_x moieties, boosting acidic 2e[−] ORR performance to a FE of 92% in 0.1 M HClO₄ electrolyte.

3.2.3. Ball milling strategy

Ball milling, as a typical top-down physical synthesis strategy, has been widely used in the preparation of SAECs. This method relies on the mutual collision and friction of grinding balls and abrasive materials in a high-energy ball mill to physically pulverize large solid materials into smaller particles [134]. Commonly, the milling media utilized in ball milling processes consist of ZrO₂, agate, or stainless steel. The ball milling process induces the breaking and reforming of chemical bonds, enabling the nanoscale modification of materials. Under specific conditions, it can even achieve single-atom dispersions [134]. Leveraging this method, Strasser and colleagues [47] successfully produced a range of M–N–C catalysts (M = Mn, Fe, Co, Ni, Cu). Structural characterization of these M–N–C SAECs revealed similar characteristics across the range, with variations mainly in the metal nature of the active sites. Performance tests were carried out in 0.1 M HClO₄ and demonstrated that the selectivity of the Co–N–C SAECs for H₂O₂ was 80%, equivalent to that of the precious metal catalysts working under identical conditions.

In conclusion, the advent of M–N–C SAECs constitutes a significant breakthrough in the electrochemical ORR, leveraging various synthesis strategies to achieve enhanced performance. **Table 2** and **Fig. 8** compare the strengths and limitations of bottom-up and top-down synthesis strategies. **Table 3** offers a comparison of diverse synthesis methods, assessing energy consumption, production yield, capital expenditure, technical intricacy, and commercialization potential. Bottom-up methods offer precise control over M–N–C SAECs' configuration, enhancing $2e^-$ ORR selectivity and mitigating metal atom aggregation. However, these processes are highly intricate, requiring meticulous parameter regulation, which limits their scalability. In contrast, top-down approaches simplify synthesis by extracting metal atoms from bulk materials, reducing costs and enabling scalable production. Despite these advantages, top-down synthesis faces challenges in controlling atomic-level structures, often leading to nanocluster formation, low metal loading, and potential catalyst deactivation due to the incorporation of impurities. In summary, bottom-up approaches excel in tailoring metal active sites for $2e^-$ ORR mechanism studies, whereas top-down are favored for industrial production. Future research should focus on refining top-down synthesis techniques by introducing protective atmospheres and adjusting the physicochemical properties of ball-milled beads to enhance catalyst purity and performance for large-scale implementation.

Table 2. The merits and demerits of bottom-up and top-down methods for M–N–C SAEC synthesis.

Methods	Merits	Demerits
Bottom-up	(i) Precise regulation of coordination environments at single-atom sites. (ii) High dispersion of metal atoms through precursor modulation.	(i) Complex synthesis steps, need to strictly control the reaction conditions. (ii) Vulnerable to structural heterogeneity in large-scale production.
Top-down	(i) Simple process, direct peeling single atomic sites from the bulk material (ii) Lower cost, suitable for large-scale preparation.	(i) Difficult to precisely control the chemical state of single-atom sites. (ii) Impurities may affect catalytic performance.

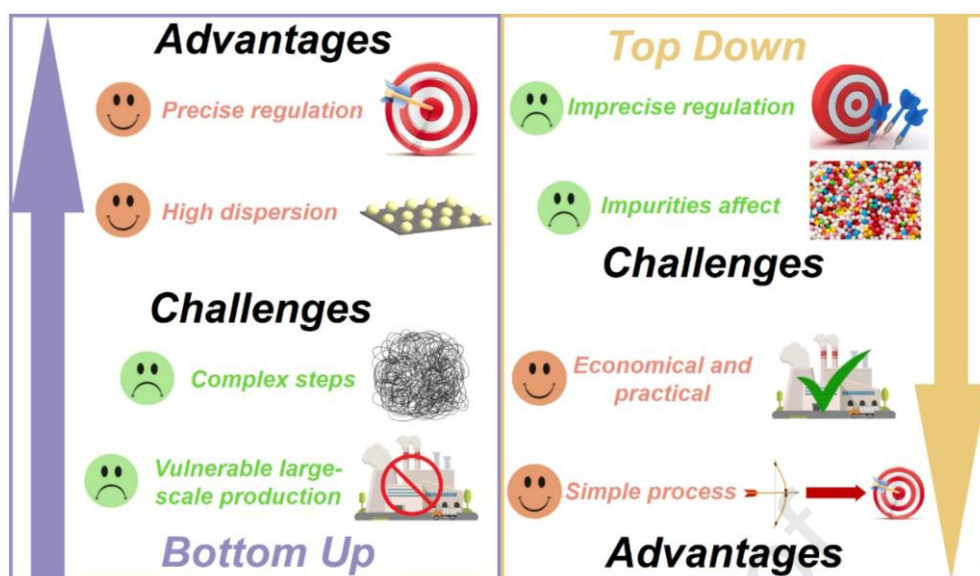


Fig. 8. The advantages and challenges of bottom-up and top-down methods for M–N–C SAEC synthesis.

Table 3. Detailed comparison of various methods for M–N–C SAEC synthesis.

Methods	Energy consumption	Production yield	Capital expenditure	Commercialization potential
Impregnation	Low to moderate	Moderate to high	Low	High (Widely used in industry)
Microwave heating	Moderate to high	Moderate	High	Low (Requires special equipment)
Pyrolysis	High	Moderate to high	Moderate to high	Moderate (High cost limitation)
Chemical etching	Low	Low to moderate	Moderate	Low (Complex process control)
Ball milling	Moderate to high	High	Moderate to high	Moderate (Limited to certain materials)

4. Advanced analysis techniques for M–N–C SAECs

Identifying these single atoms at an atomic level poses significant challenges, necessitating tools with exceptionally high spatial resolution. Over the past few decades, advancements in techniques have led to atom-scale resolution capabilities. These advanced methods allow for the differentiation of ensemble-level signals emanating from all reactive species, thereby mitigating the risk of data misinterpretation and ensuring an accurate representation of the genuine active atomic species.

4.1. Techniques for single-atom visualization

4.1.1. Advanced electron microscope technologies

Advancements in microscopy technology have enabled the direct visualization of nanoparticles or atoms situated on catalyst supports. Among the arsenal of electron microscopy techniques, aberration-corrected high-angle annular dark field/scanning transmission electron microscopy (AC-HAADF/STEM) stands out for its ability to elucidate the intricate distributions and exact positions of single atoms within a catalyst. This is achieved through a combination of both bright and dark field imaging methods, where aberration correctors play a pivotal role in enhancing the resolution of electron microscopes [135]. Such improvements are essential for distinguishing atoms positioned closely together, a necessity for identifying the single atoms that often constitute the active sites of these catalysts. In HAADF-STEM, an annular detector is used to collect electrons scattered by the sample, especially those scattered at larger angles. This approach is inherently sensitive to the atomic number of the sample, enabling it to distinguish between different types of atoms based on the principle that heavier atoms scatter electrons to higher angles more effectively [136]. Consequently, AC-HAADF/STEM proves to be especially useful for examining carbon-supported SAECs, wherein the quantity of atoms at the metal sites significantly exceeds that of the atoms on the support [137]. As a result, it has been widely used to distinguish the individual non-precious metal sites supported on carbon-based substrates [112,138,139].

Despite its advantages, the applicability of AC-HAADF/STEM to SAECs is limited by several inherent constraints. The technique struggles to differentiate between adjacent transition metals (e.g., Fe vs. Co), due to their similar atomic numbers, and it is largely insensitive to light elements like nitrogen, which are crucial for elucidating coordination environments. Additionally, atoms buried beneath thick carbon layers, obscured by heavy dopants, or located in subsurface regions are often undetectable. The limited field of view of the method compromises its ability to provide statistically representative information. Moreover, AC-HAADF/STEM requires high-vacuum conditions, which differ significantly from operational electrochemical environments. This discrepancy, along with susceptibility to electron beam-induced artefacts, hampers its ability to capture dynamic changes such as active site reconstruction or transient intermediate formation during catalysis.

4.1.2. Complementary technologies

Distinguishing atomically dispersed sites from their supports becomes problematic when the supports include metal elements, such as metal oxides. To overcome this limitation, ancillary techniques such as energy dispersive X-ray spectroscopy (EDS) or electron energy loss spectroscopy (EELS) are frequently employed alongside HAADF-STEM to facilitate a comprehensive understanding of the catalyst [140]. EDS typically operates by directing an electron beam at samples, prompting them to release characteristic X-rays, and facilitating a qualitative assessment of their composition [141]. When an atom remains stationary, it enables the chemical differentiation of individual atomic sites, nanoscale structures, and their supporting materials. Due to its relatively poor detection efficiency at low count rates, EDS faces challenges in differentiating metal atoms whose atomic numbers are similar to or lower than those of the supporting atoms. Conversely, EELS, with its superior detection efficiency and spatial resolution, is becoming an increasingly valuable complement to STEM characterization, particularly for identifying light elements [142]. EELS involves bombarding a specimen with a beam of high-energy electrons. When electrons traverse a sample, they interact with its atomic structure, causing some of them to lose energy. The lost energy is measured and recorded as a spectrum, reflecting the unique elemental composition and chemical bond types within the material. Analysis of this energy loss spectrum enables the determination of the sample's composition, chemical states, and electronic structure. EELS is capable of distinguishing between single atoms and nanoparticles based on their chemical composition, and it is especially proficient at differentiating between various non-metal elements.

4.2 Techniques for detecting coordination structures in M–N–C SAECs

4.2.1. X-ray absorption fine structure spectroscopy

The development of electron microscopy technologies has made it possible to visualize dispersed metal atoms within SAECs. However, these methods fall short of revealing the coordination structure or the bond lengths of the individual metal centers. X-ray absorption fine structure (XAFS) spectroscopy has emerged as a powerful technique for characterizing the structural and electronic properties of materials at the atomic level, making it particularly valuable for the study of SAECs [143]. This technique involves measuring the absorption of X-rays as a function of energy. When X-rays are absorbed by an atom, they can cause the ejection of an electron from an inner shell (typically the K or L shell). As the energy of the incident X-

rays is varied, the absorption intensity shows fine structure beyond the edge where core-level electrons are excited. XAFS encompasses two main components: extended X-ray absorption fine structure (EXAFS) and X-ray absorption near edge structure (XANES), each providing complementary information about the catalyst, as demonstrated in Fig. 9a [144].

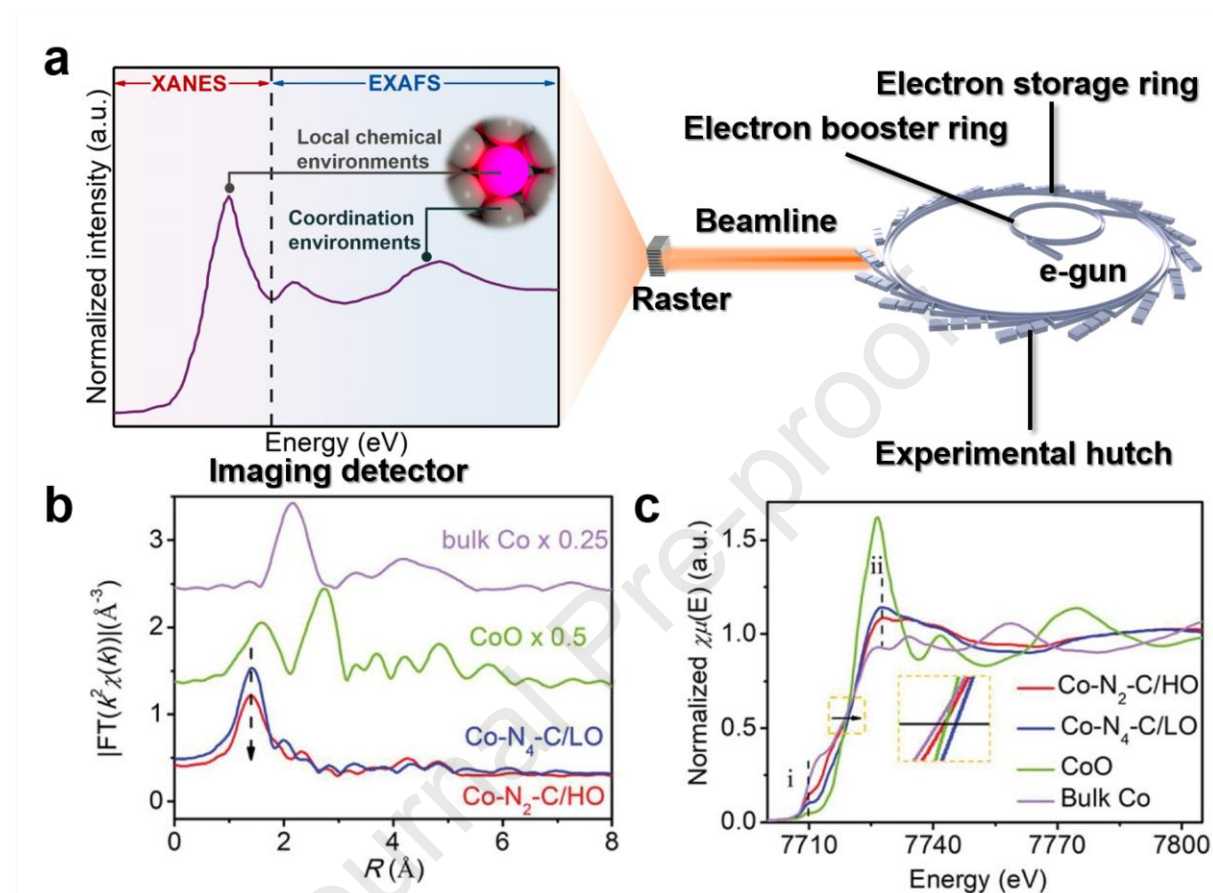


Fig. 9. (a) The principle of XAFS, and a schematic representation of the regions in XANES and EXAFS. (b) FT magnitudes of Co K-edge EXAFS for Co-N₂-C/HO, Co-N₄-C/LO, and the reference samples. (c) K-edge XANES spectra of Co-N₂-C/HO, Co-N₄-C/LO and reference samples; reprinted with permission [119], Copyright 2022, Wiley.

EXAFS is notably used to determine the absence of metal–metal bonds within SAECs based on the uniformity of their atomic structure, distinguishing isolated atoms from small atomic clusters, like dimers and trimers. Within current capabilities, the uniformity adjustment during atomic structure analysis can potentially blur the distinction between solitary atoms and small groupings. Due to its sensitivity limits, EXAFS may not always distinctly distinguish between single atoms and such minimal clusters [145]. In contrast, XANES provides detailed information about the electronic states of atoms and their local chemical environment by measuring the X-ray absorption intensity as a function of energy near the absorption edge. This technique is adept at discerning the oxidation state, coordination geometry, and electronic

structure of the absorbing atom [146]. In particular, by employing suitable benchmarks, XANES facilitates determining bond lengths and coordination numbers through a fitting process, thereby yielding accurate structural details about SAECs [41]. Gong and co-workers [119] used XAFS for detecting the normal Co–N₄ moiety and the low-coordinated Co–N₂ structure. Through EXAFS analysis, both configurations showed a principal peak at approximately 1.4 Å, indicative of Co–N coordination. Notably, there were no discernible peaks related to Co–Co interactions, as shown in **Fig. 9b**. Furthermore, the Co–N₂ structure exhibited a significantly reduced peak intensity for Co–N coordination compared to the Co–N₄ structure, indicating a diminished nitrogen coordination number at the cobalt center. Further insights were gained from XANES analysis, as demonstrated in **Fig. 9c**, where, in contrast to Co–N₄, a noticeably diminished peak ii (1s→4p_{xy} transitions) was evident in Co–N₂. This reduction indicated a flawed graphene structure and a sparse coordination environment surrounding the Co atoms in the Co–N₂ structure.

Nevertheless, XAFS (XANES/EXAFS) techniques have inherent limitations for characterizing SAECs. The ensemble averaging effect makes it difficult to detect minor species or low-concentration elements. Furthermore, XAFS demonstrates limited sensitivity to light coordinating elements (such as C, N, O) that are crucial for understanding the metal center coordination environments of SAECs. Conventional XAFS, being inherently static, often fails to capture transient intermediates unless performed under operando conditions. Additionally, the spatial resolution of XAFS is inadequate for probing local micro-environmental heterogeneities, including pH gradients near active sites. Recent developments in time-resolved and quick XAFS have partially addressed dynamic monitoring but introduce complexities in spectral deconvolution, often necessitating complementary computational modeling.

4.2.2. X-ray photoelectron spectroscopy

X-ray photoelectron spectroscopy (XPS) is a prevalent method for analyzing the chemical states and electronic structures of surface materials and has been extensively applied to SAECs for probing their chemical states and the electronic environment of their surroundings [147,148]. XPS operates on the principle of the photoelectric effect, wherein X-rays irradiate a material, causing electrons to be ejected from its surface. Electrons' binding energy can be calculated by measuring the kinetic energy they emit from the material's surface, which is unique to specific elements and their chemical states. By analyzing these binding energies, it is possible to identify and quantify the elements present on the material's surface [149]. XPS can directly assess the

chemical state and electronic environment of the metal atoms in SAECs, offering critical information about the metal atoms' oxidation state and their interactions with the supporting material [41].

However, XPS also faces notable limitations with respect to characterizing SAECs. It struggles with the accurate quantification and assignment of chemical states in M–N–C species due to pronounced peak overlaps, especially among first-row transition metals. Additionally, the technique is prone to causing beam-induced damage and unintended surface reduction/oxidation during analysis. Crucially, XPS lacks the capability to provide direct structural insights into coordination environments or bond distances, fundamentally limiting its ability to resolve critical atomic-scale configurations.

4.3. Techniques for catalytic process investigation

4.3.1. *In situ* infrared spectroscopy

Infrared (IR) spectroscopy involves irradiating a sample with IR light, causing vibrational transitions in the molecules; each type of bond within a molecule absorbs characteristic frequencies, and by measuring these frequencies, we can determine the specific structure within the catalyst [150]. The utilization of IR spectroscopy significantly enhances the detailed examination of catalyst configurations and their mechanisms, proving particularly beneficial in analyzing surface-bound intermediate products due to its capacity for detecting heterogenous species. The versatility of IR spectroscopy is further expanded when it is applied as *in situ* electrochemical micro IR spectroscopy or diffuse reflectance Fourier transform IR spectroscopy, techniques that enhance the understanding of dynamic chemical processes on catalysts [151]. Specifically, attenuated total reflectance and differential reflectance spectroscopy are common configurations used to enhance sensitivity and facilitate measurements under electrochemical conditions [152].

Within the investigation of mechanisms underlying the M–N–C SAEC-catalyzed $2e^-$ ORR, *in situ* attenuated total reflectance infrared absorption spectroscopy (ATR-FTIR) serves as a pivotal tool for assessing the interactions between catalytic intermediates and catalysts. By monitoring disappearances and alterations in shape, it is possible to pinpoint the rate-determining step within a catalytic cycle, providing critical insights into the reaction processes [153,154]. As shown in **Fig. 10**, the distinction between $2e^-$ and $4e^-$ ORR pathways lies in their intermediate adsorption configurations and dynamic evolution. ATR-FTIR is prioritized to

capture the OOH^* intermediate adsorption behavior, where the characteristic vibrational peaks ($1200\text{--}1300\text{ cm}^{-1}$) serve as direct indicators of H_2O_2 selectivity. As illustrated in **Fig. 10a**, the absorption bands at about 1254 cm^{-1} and 1384 cm^{-1} can be assigned to the O–O stretching vibration of the OOH^* intermediate and the OOH bending pattern of the surface adsorbed $^*\text{H}_2\text{O}_2$, respectively [49,154,155]. Generally, when overpotential increases, this band intensifies, validating the OOH^* -mediated 2e^- ORR pathway [52,155]. Li and colleagues [153] performed *in situ* ATR-FTIR to gain a mechanistic understanding of Fe–N–C SAECs in the 2e^- ORR. As shown in **Fig. 10b**, by integrating S species into the asymmetric active site of FeN_3S_1 (shown in **Table 1**), a significant enhancement in the proton spillover was achieved, which facilitated the swift generation of the crucial OOH^* intermediate and expedited the entire kinetics of H_2O_2 electrosynthesis.

4.3.2. *In situ* Raman spectroscopy

In situ Raman spectroscopy has emerged as a pivotal tool for characterizing electrochemical reactions, offering detailed insights into catalyst structures, dynamics, and electronic properties under operational conditions [156–158]. In contrast to IR spectroscopy, which necessitates the molecule's polarity for the excitation light source, Raman spectroscopy does not have such a prerequisite, making it a complementary technique to IR. This difference allows Raman spectroscopy to analyze a wide array of chemical substances, since it is based on the vibrational and rotational energy levels of a molecule, which remain constant across various conditions. However, traditional Raman spectroscopy faces challenges when it comes to capturing detailed surface structure information during heterogeneous catalysis, due to its low sensitivity. To address these challenges, advanced methods like surface-enhanced Raman spectroscopy, needle-tip-enhanced Raman spectroscopy, and shell-isolated nanoparticle-enhanced Raman spectroscopy have been developed. These techniques significantly boost the sensitivity of Raman spectroscopy, enabling the precise detection of individual molecules on catalyst surfaces [159–161]. The 2e^- ORR process proceeds without O–O cleavage, whereas O–O breakage is a key step in the 4e^- ORR process. Leveraging *in situ* Raman spectroscopy is paramount for monitoring the dynamics of O–O bond cleavage, particularly by tracking the evolution of the metal center's oxidation states and the critical role played by transient O^*/OH^* intermediates [162].

To monitor the dynamic changes surrounding M–N–C SAEC metal centers in the 2e^- ORR, researchers have employed *in situ* Raman spectroscopy, which is capable of furnishing

microstructural insights on the molecular scale. Dong and co-workers [52] used it to dynamically monitor alterations in carbon structure within Mn–N–C SAECs. **Fig. 10c** illustrates the variation in carbon structure that took place during the $2e^-$ ORR process; **Fig. 10d** shows there was a significant decline in all Raman bands at the beginning of the reaction, indicating the absence of the OOH^* intermediate on the carbon atoms, as oxidized carbon atoms ought to exhibit a more robust Raman response. As the reaction proceeded, a noticeable upward trend was observed in the Raman bands, illustrating the electron transfer dynamics taking place between the central Mn metal sites and the adjacent carbon atoms.

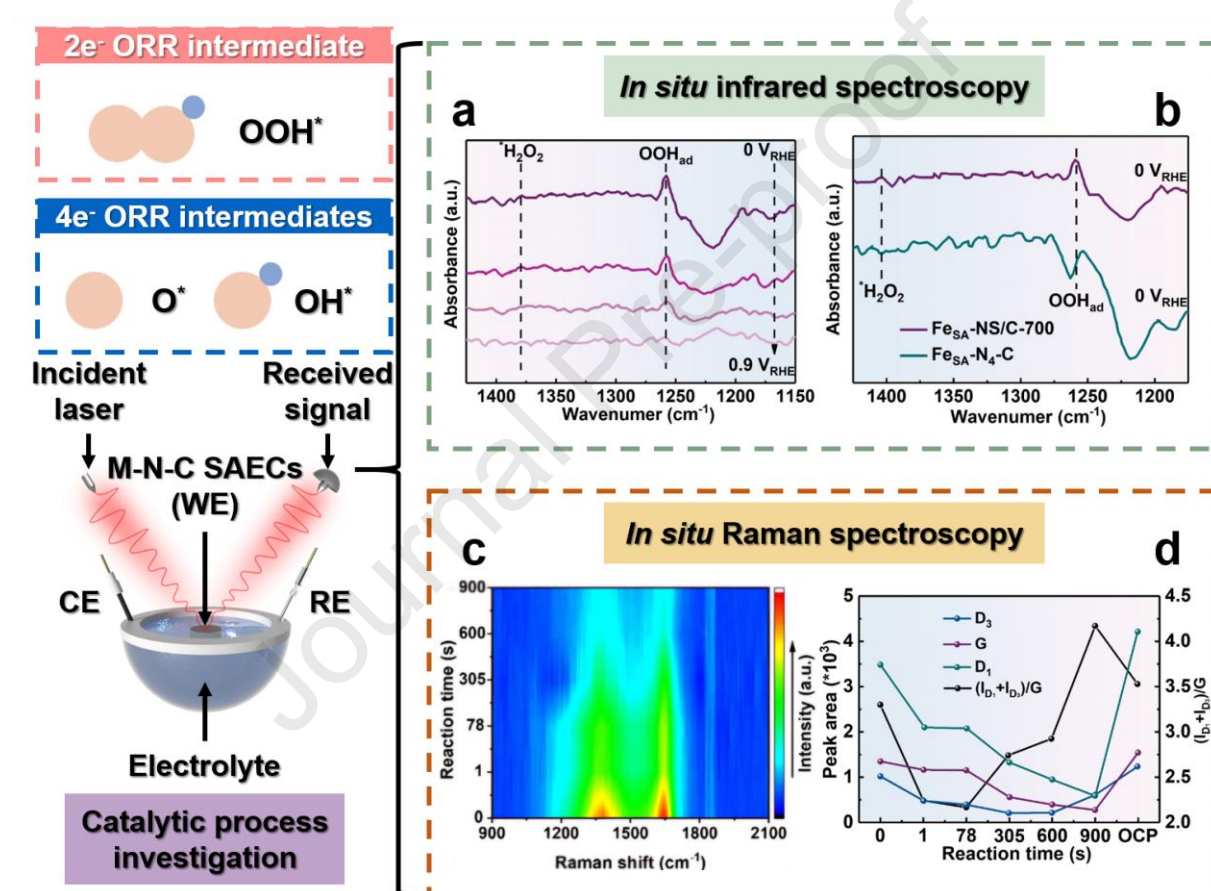


Fig. 10. *In situ* techniques used for detecting critical intermediates in the $2e^-$ ORR (OOH^*) and $4e^-$ ORR (O^* , OH^*). (a) *In situ* ATR-FTIR spectra recorded during the electrocatalytic synthesis of H_2O_2 . (b) Enlarged *in situ* ATR-FTIR spectra of FeSA-NS/C-700 and FeSA-N₄-C; reprinted with permission [153], Copyright 2023, Wiley. (c) *In situ* Raman spectra recorded over Mn–NO–C_H surfaces. (d) Peak area and area ratio of $(D_1 + D_3)/G$ for Mn–NO–C_H electrocatalysts as a function of reaction time; reprinted with permission [52], Copyright 2024, Wiley.

In summary, rapid advances in characterization methods are enabling us to gain a comprehensive understanding of M–N–C SAECs' atomic-scale structures and properties. AC-HAADF/STEM facilitates the direct visualization of individual metal atoms on carbon-based

substrates but lacks chemical/electronic detail and is susceptible to inflicting beam-induced damage, particularly on beam-sensitive species. Complementary techniques like EDS and EELS further enhance the analysis of SAEs' elemental composition, supplementing electron microscopy but still falling short in resolving the local coordination environments of active sites. X-ray spectroscopy techniques such as XAFS and XPS fill the gap by providing a thorough characterization of the metal centers in M–N–C SAEs. However, XAFS lacks spatial resolution and struggles with dynamics/heterogeneity, while XPS interpretation often relies on structural context provided by the other techniques. Therefore, a synergistic application of these complementary methods is essential to overcome individual limitations and construct a comprehensive understanding of the structure–function relationships in M–N–C SAEs. Additionally, *in situ* FT-IR and Raman spectroscopy have been employed for detecting the OOH* intermediate in real time and monitoring catalyst structural changes during the M–N–C SAE-catalyzed $2e^-$ ORR process. These spectroscopic techniques illuminate the reconfiguration behavior of catalysts under operational conditions, offering insights into the dynamics of the active site during catalysis.

5. M–N–C SAEs for H₂O₂ production

5.1. Dispersed metal center sites of M–N–C SAEs

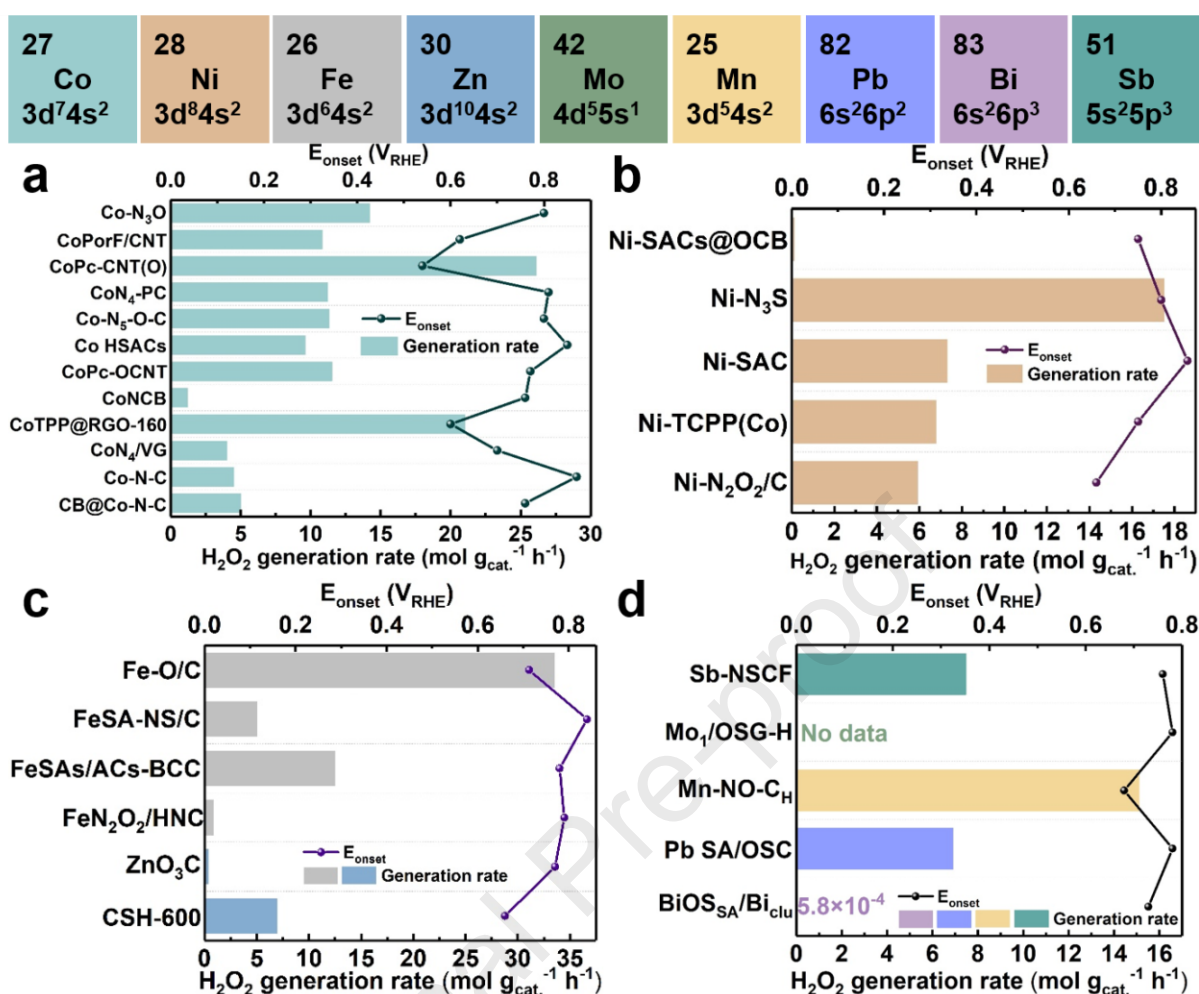


Fig. 11. H_2O_2 generation rate and onset potential of most novel M-N-C SAECs newly reported, with (a) Co metal center site, (b) Ni metal center site, (c) Fe and Zn metal center site, (d) Mo, Mn, Pb, and Bi metal center site; data adapted from ref. [51,52,165–174,92,175–181,112,139,153–155,163,164].

In the majority of instances, individual metal atoms in separation typically engage in direct interactions with intermediates during the ORR [182]. Hence, the characteristics of M-N-C SAECs are significantly influenced by the central metals. Modifying the central metal offers a straightforward and effective approach for customizing the properties of M-N-C SAECs. **Fig. 11** reveals that different metal active centers lead to varying catalytic activity and selectivity for the $2e^-$ ORR. As depicted in **Fig. 12a**, the Co-N₄ complex within the typical M-N₄ structures stands out on the volcano plot due to its moderate adsorption strength for OOH^* , highlighting its significant involvement in and selectivity toward the $2e^-$ pathway. Furthermore, **Fig. 12b** shows that Co-N-C SAECs exhibit superior $2e^-$ ORR selectivity in RRDE tests (the ring current is at its peak, while the disk current remains comparatively low), aligning well with the theoretical calculations. **Fig. 12c**, which is based on both computational and experimental findings, further demonstrates the selectivity of common M-N₄ configurations in SAECs for

the ORR with different electron transfer numbers. In this case, Fe-N₄ and Mn-N₄ exhibit strong adsorption of OOH*, leading to O-O bond cleavage and a preference for the 4e⁻ ORR pathway. On the other hand, Co-N₄ shows optimal selectivity for the 2e⁻ ORR due to its balanced adsorption of key intermediates. In contrast, Ni-N₄ and Cu-N₄ have weaker adsorption energies for OOH* intermediates, resulting in lower ORR selectivity. These findings suggest that among conventional SAECs featuring the M-N₄ configuration, Co-N-C exhibits the highest selectivity for the electrosynthesis of H₂O₂.

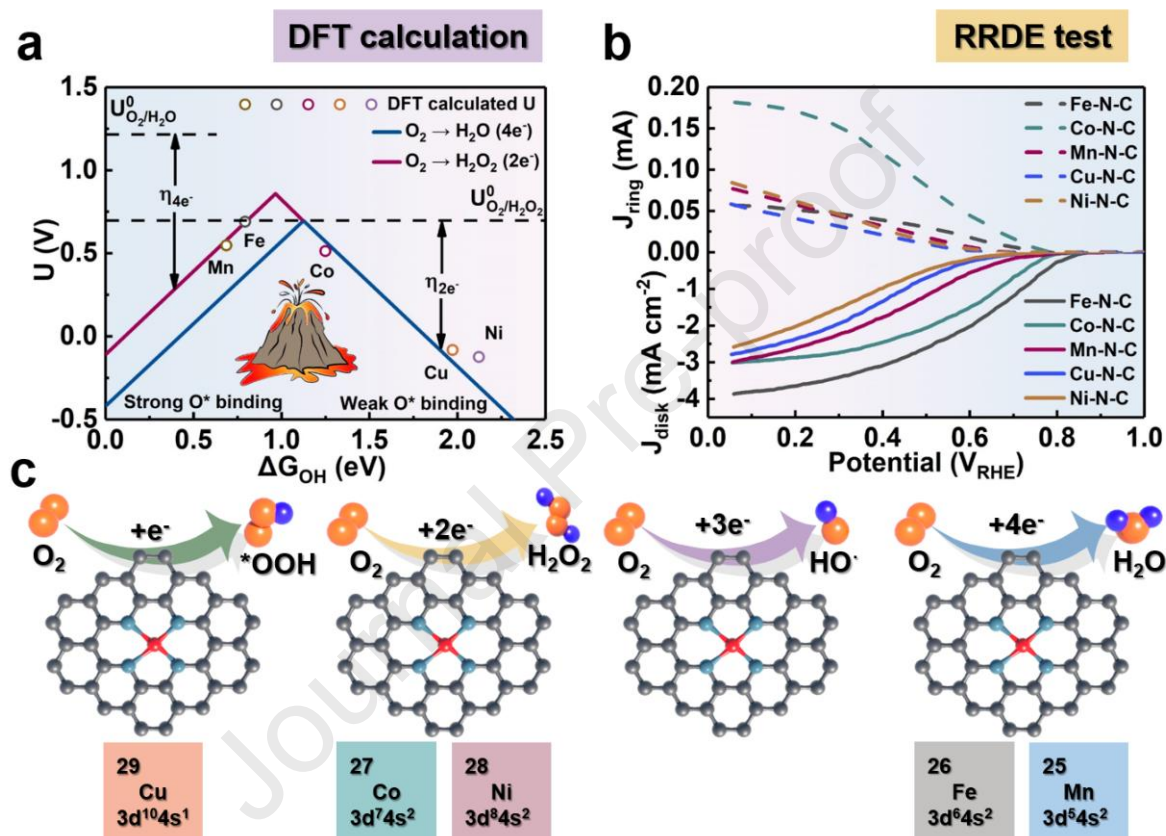


Fig. 12 (a) Activity-volcano curves of ORR via the 2e⁻ or 4e⁻ pathway. (b) Linear sweep voltammetry (LSV) in an RRDE setup; reprinted with permission[47], Copyright 2019, American Chemical Society. (c) Schematic of the ORR along the 1e⁻, 2e⁻, 3e⁻, or 4e⁻ pathways on M-N₄ SAECs anchored in carbon-based substrate.

5.1.1. Co-based metal center sites

Their catalytic characteristics make Co-N-C SAECs the preferred type of catalyst for H₂O₂ generation when compared to other M-N-C SAECs. This is because an optimally aligned d-band center is essential for enhancing catalytic properties [183]. The Co-N-C SAEC synthesized by Jung and coworkers [48] demonstrated a kinetic current intensity of 2.8 mA cm⁻² and a mass activity of 155 A g⁻¹ (at 0.65 V_{RHE}) while exhibiting negligible activity degradation across 110 hours for H₂O₂ production. Cao et al. [155] developed a Co-N-C SAEC

that achieved an unparalleled H_2O_2 generation rate exceeding $11 \text{ mol g}_{\text{cat}}^{-1} \text{ h}^{-1}$ at a current density of 300 mA cm^{-2} with 96–100% FE (as shown in **Fig. 13a**). Overall, these studies reveal that among the various transition metal-based materials, those containing cobalt tend to follow a predominant 2e^- pathway, demonstrating enhanced selectivity and activity. The electrocatalytic generation of H_2O_2 exhibits significant practical utility in environmental remediation applications. Notably, Zhang's group recently developed a cobalt–oxygen coordinated porous carbon catalyst ($\text{Co-O}_4\text{@PC}$, shown in **Table 1**) that exhibits exceptional compatibility with the Fenton process due to its efficient H_2O_2 production [138]. RhB organic dye and *S. aureus* were used as model contaminants. The study demonstrated that fresh RhB solution underwent 85.7% degradation after the generated H_2O_2 was added at a constant potential of 0.6 V for 1 h. The *S. aureus* was completely eradicated by adding the generated H_2O_2 and $10 \text{ }\mu\text{M}$ FeSO_4 , underscoring its strong potential for wastewater treatment and sterilization.

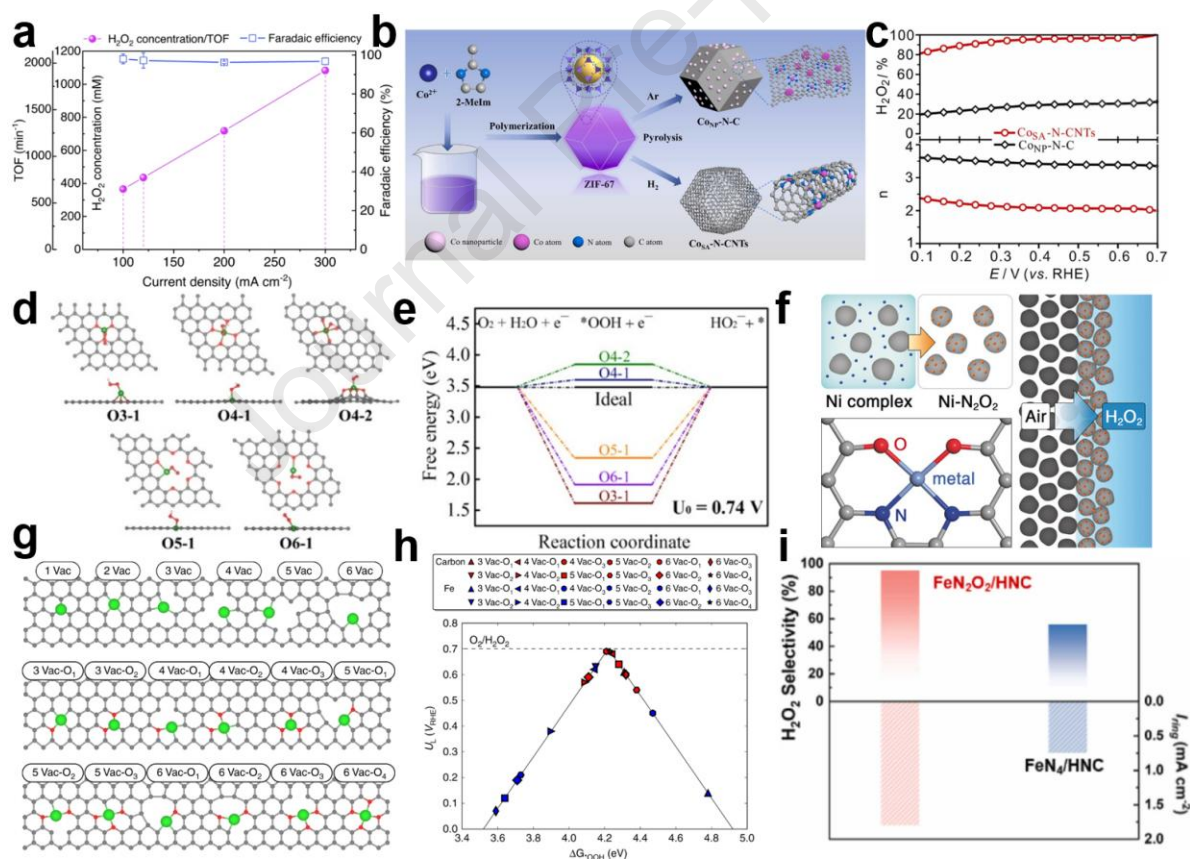


Fig. 13 (a) H_2O_2 concentration, FE, and TOF values of CoPc-OCNT at 100, 120, 200, and 300 mA cm^{-2} ; reprinted with permission [155], Copyright 2023, Springer Nature. (b) Schematic illustration of the preparation routes for CoSA-N-CNTs and CoNP-N-C catalysts. (c) Corresponding H_2O_2 selectivity and electron transfer number (n); reprinted with permission [184], Copyright 2022, Elsevier. (d) Top and side views of the OOH^* -adsorbed configurations on Ni-N-C SAEs. (e) Calculated free-energy diagram of oxygen reduction to HO_2^- ; reprinted with permission [185], Copyright 2020, American Chemical Society. (f)

Ni-N₂O₂ configuration and electrosynthesis of H₂O₂ using the three-phase flow cell device on the cathode; reprinted with permission [92], Copyright 2020, Wiley. (g) Optimized configurations for a single Fe atom coordinated in a two-dimensional carbon material with and without O species. (h) Volcano plot of the calculated ORR activity for the 2e⁻ pathway towards H₂O₂; reprinted with permission [186], Copyright 2019, Springer Nature. (i) Comparison of selectivity and ring current density between FeN₂O₂/HNC and FeN₄/HNC catalysts; reprinted with permission [176], Copyright 2022, Elsevier.

The creation of Co-N-C SAECs unavoidably results in the generation of cobalt nanoparticles. Zhang's team crafted cobalt nanoparticles enveloped within carbon substrates under an Ar atmosphere (denoted as CoNP-N-C) [184]. Additionally, they introduced cobalt atoms widely integrated into nitrogen-doped carbon nanotubes (CNTs) in an H₂ environment (denoted as CoSA-N-CNTs). Elevated temperatures (900–1000°C) induced H₂ etching, which enhanced the formation of voids and vacancies within the carbon substrates (as shown in **Fig. 13b**). This, in turn, helped to eliminate cobalt nanoparticles during the subsequent acid etching process, thereby preventing cobalt atoms from accumulating and mobilizing. It was inferred that the CoNP-N-C catalyst, containing residual cobalt nanoparticles, exhibited a marked preference for the 4e⁻ ORR pathway. In contrast, CoSA-N-CNTs, characterized by atomically dispersed Co atoms, followed the 2e⁻ ORR pathway with a selectivity exceeding 95%, underscoring the pivotal role of isolated Co atoms in the electrochemical generation of H₂O₂ (as shown in **Fig. 13c**). Hence, the local structures of Co-N-C SAECs vary depending on the precursors and synthesis approaches, which may lead to remarkable variations in the catalytic properties and potentially contradictory outcomes. It is crucial to conduct meticulous characterization of the geometric structures to accurately identify authentic active arrangements.

5.1.2. Ni-based metal center sites

The general properties of Ni-N-C SAECs for the ORR are found to be less optimal than those of Co SAECs. Within the course of the transition metal-catalyzed ORR process, Yang et al.'s groundbreaking research [187] introduced the occupancy of σ^* (eg) in the metal-oxygen ligand as a fundamental property indicator, drawing from molecular orbital theory. They attributed the reduced activity of molecular nickel phthalocyanine, featuring a fully loaded d_{z²} orbital, mainly to the attenuated Ni-O₂ interaction and hindered electron transfer, which thereby affected the activation of O₂. Similarly, the conventional pyridine/pyrrole N-ligand NiN₄ molecule exhibits a quasi-square planar geometry, and the key step in deciding the potential is the formulation of the intermediate OOH* [188].

The adhesion intensity of the OOH* on Ni sites is notably weak [20]. To enhance the inherent properties of Ni-N-C SAECs, previous research has primarily concentrated on

adjusting the metal-centered configurations to produce a range of NiN₄ variants [50,92]. Using DMF as both ligand and reducing agent, Ni–N–C SAECs embedded on oxygen defects were successfully prepared by Song et al. [185] and demonstrated 94% selectivity for the 2e[−] ORR within the range of 0.1–0.5 V_{RHE} in 0.1 M KOH electrolyte. Their investigation identified the Ni–O configuration as the active site for the 2e[−] ORR, with an optimal coordination number of 4 for the O atom (as shown in **Figs. 13d–e**). Elsewhere, Zhang et al. [92] introduced a novel pyrolysis approach guided by Schiff base ligands, enabling the construction of a well-defined tetradentate Ni–N₂O₂ structure (illustrated in **Fig. 13f** and **Table 1**). The resultant Ni–N₂O₂/C catalyst demonstrated 96% selectivity for H₂O₂, surpassing that of the NiN₄/C catalyst (62%) under 0.1 M KOH conditions. Additionally, when the N or C atoms in the configuration were substituted with O atoms, the SAECs showed better performance [94,178]. Following this principle, Xiao et al. [50] created a Ni–N–C SAEC embedded in CNTs, featuring a highly coordinated N₄NiO₂ configuration wherein the two oxygen atoms originated from the carboxyl group in the CNTs. This SAEC with a hexacoordinated structure demonstrated effectiveness in the 2e[−] ORR, with a FE of 96% under 200 mA cm^{−2} for 24 h of operation in 1 M KOH. The electrocatalytic synthesis of H₂O₂ via Ni–N–C SAECs demonstrates considerable practical potential, as evidenced by Liao's investigation [189]. Their design of a phthalocyanine-embedded covalent organic framework (BBL–PcNi COF) enabled efficient H₂O₂ production. To evaluate the antimicrobial efficacy of BBL–PcNi-generated 3.5 wt% H₂O₂ disinfectant, experiments were conducted in lake water. Remarkably, photochemical activation under broadband irradiation enabled the optimized H₂O₂ formulation (1:20 v/v dilution) to achieve 100% bacterial deactivation efficiency (initial load: 4.47 × 10⁴ CFU mL^{−1}).

5.1.3. Fe-based metal center sites

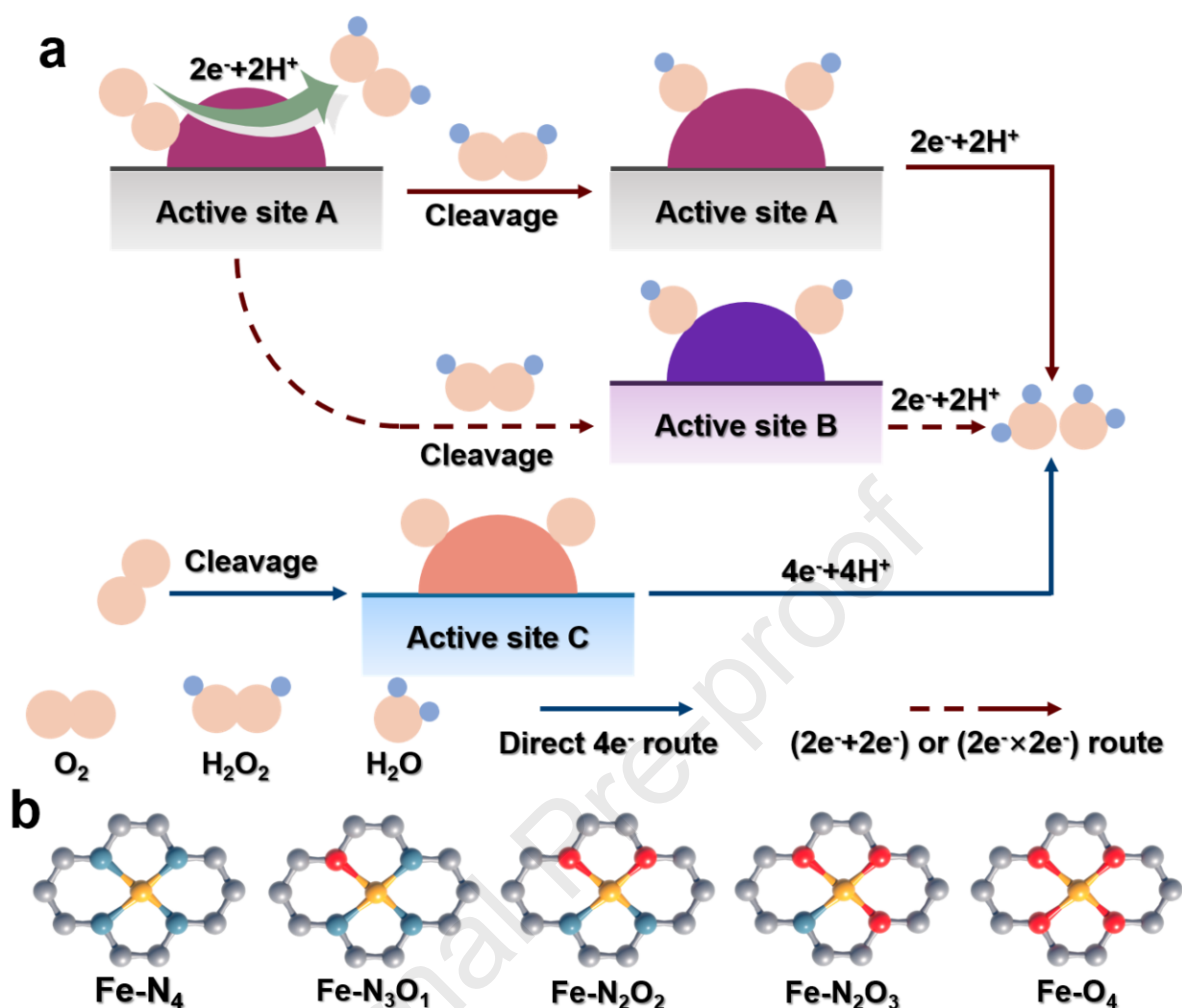


Fig. 14. (a) ORR mechanisms on Fe-N-C catalysts with single or several active sites. (b) Simulated model of single-atomic Fe moiety showing different types of (N, O)-coordination environments.

Fe-N-C SAEs have been extensively studied in relation to the ORR [79,190,191]. In 2014, Kattel and colleagues [192] published findings on ORR catalytic properties using non-noble Fe₁N₄-anchored graphene SAEs. They demonstrated that Fe₁N₄ hybrids can promote all conceivable ORR fundamental reactions and that their catalytic ability is competitive with that of noble metal catalysts. Through theoretical investigations, researchers revealed that the Fe-N-C SAEs exhibited a high affinity for the 4e⁻ pathway, with lower 2e⁻ selectivity [20,48]. Notably, the concurrent existence of various Fe particles in most catalysts has complicated the elucidation of their ORR performance, primarily owing to the cooperative influences of several sites. For instance, Choi and coworkers [193] discovered that the reactive sites responsible for H₂O₂ reduction were the Fe-N_x-C segment and the N-doped carbon layer coated with Fe particles. Conversely, nitrogen-doped carbon unaccompanied by iron particles showed a lack of activity. The presence of several active sites appears to be a prerequisite for catalyzing a

multi-electron ORR. As shown in **Fig. 14a**, this catalytic reaction can be processed either directly via a $4e^-$ route at a singular site (O_2/H_2O) or indirectly at two separate sites for the desorption of H_2O_2 intermediates ($O_2/H_2O_2/H_2O$). These active sites may have similar properties, resulting in a $2e^- \times 2e^-$ mechanism, or they may differ, giving rise to a bifunctional $2e^- + 2e^-$ mechanism.

Previous investigations have indicated that M–C–O molecules exhibit a robust ability to alter the inherent binding intensity. This capability allows them to modulate the catalytic route and reduce the adhesion of intermediates, unlike M–N–C molecules, thus facilitating the $2e^-$ ORR. As illustrated in **Fig. 14b**, substituting the N atom with O in the traditional Fe–N₄ coordination structure can improve the $2e^-$ ORR selectivity [194,195]. Jiang et al. [186] discovered that substituting N atoms with O atoms in the Fe–N–C conformation significantly strengthened OOH* incorporation at the C site. The linking between C and OOH* in the Fe–N–C configuration was found to be notably weaker than that observed in the Fe–C–O ligand (as shown in **Figs. 13g–h**). They created a range of SAECs embedded in CNTs and investigated the impact of the center atoms on ORR properties. This approach contrasts with the metal-free equivalents that solely incorporate oxygen dopants. In the series, the Fe–CNT variant with a 0.1 at% loading of iron demonstrated outstanding performance in H_2O_2 generation, achieving a selectivity of 95.4% in an alkaline electrolyte. Wu and colleagues [176] synthesized well-defined (O, N)-coordinated Fe SAECs (FeN₂O₂) attached to hollow nitrogen-doped carbon nanospheres, along with conducting a comprehensive exploration of their electrochemical properties for the conversion of O_2 to H_2O_2 . They discovered that electron redistribution within the M–O structure effectively reduced the d-band core of Fe, thus reducing the adhesion ability for intermediates and boosting the $2e^-$ ORR route. The resultant FeN₂O₂ moiety demonstrated remarkable specificity across a wide pH range, notably achieving 95% selectivity under alkaline conditions (as shown in **Fig. 13i**). In a word, although the Fe–N–C SAECs demonstrate superior ORR properties, their selectivity for H_2O_2 production is relatively low, unless the coordination environment of the Fe atoms is altered.

5.1.4. Zn-based metal center sites

The complete occupation of the 3d orbital of Zn prevents the generation of highly valent oxidized species that are detrimental to the reactors, which creates a favorable and secure production situation for large-scale H_2O_2 manufacture [196]. Modification of the spatial arrangement around the Zn atoms will enhance the $2e^-$ ORR performances of Zn–N–C SAECs.

Li et al. [178] reported that the $2e^-$ ORR properties of the engineered ZnO_3C configuration (shown in **Fig. 15a** and **Table 1**) featuring oxygen and carbon combinations significantly surpassed those of ZnN_4 . While ZnN_4 SAECs predominantly facilitated the $4e^-$ ORR route towards H_2O_2 formation, the precisely tuned local coordination of atomically separated Zn sites in ZnO_3C promoted a highly selective $2e^-$ ORR route. This resulted in the production of H_2O_2 with a nearly zero overpotential and remarkable selectivity (90%) in alkaline electrolytes (as shown in **Figs. 15b** and **c**). Computational analysis showed that the reduced electron concentration in ZnO_3C led to a decreased d-band center for Zn, altering the adhesion intensity of the OOH^* intermediate and favoring the $2e^-$ ORR process (as shown in **Fig. 15d**). More recently, Wei et al. [139] illustrated that cooperative interactions between the N_2O_2 primary coordination environment and the S atoms in the secondary coordination shell endowed isolated Zn sites with a tuned electronic configuration for the $2e^-$ ORR. The $Zn-N_2O_2$ configuration, stabilized by outer-layer S atoms (shown in **Fig. 15e** and **Table 1**), exhibited a highly desirable Gibbs free energy for the key OOH^* intermediate, its adsorption, and its subsequent dissociation at the Zn center. This synergistic coordination environment promoted efficient H_2O_2 generation via the $2e^-$ pathway (as shown in **Fig. 15f**).

The coordination configuration of the single Zn active center and the metal loading content have a dramatic effect on the $2e^-$ ORR activity. Wei and coworkers [197] prepared $Zn-N-C$ SAECs with asymmetric structural characteristics using a pre-adsorption-anchoring and pyrolysis method. Following structural refinement, the SAEC Z-PPy-600 achieved an exceptionally high Zn loading (up to 11.34 wt.%). When Z-PPy-600 was employed, the generation rate of H_2O_2 in an H-type cell could attain $248 \text{ mmol g}_{\text{cat}}^{-1} \text{ h}^{-1}$ in the initial 5 h. They observed a positive relationship over a specific range of Zn loading. Interestingly, additional growth in the percentage of Zn content resulted in a decrease in catalytic properties, suggesting that the single-atom loading rate was not the sole contributor to selectivity. They found that the comparatively low oxygen level in Z-PPy-700 hindered the generation of a greater number of asymmetrically aligned $Zn-N_3O$ active sites (shown in **Table 1**), and they demonstrated that the pivotal elements for optimizing its catalytic property toward the $2e^-$ ORR were the ultra-high loading of asymmetrically aligned $Zn-N_3O$ active sites. Broadly speaking, the integration of metal loading content with various modulation techniques has the potential to unlock novel possibilities in the creation of remarkably effective $Zn-N-C$ SAECs for the $2e^-$ ORR.

5.1.5. Other metal center sites

Non-noble metals like Mo, Pb, Mn, Bi, and Sn have rarely been explored for the $2e^-$ ORR. The latest study [179] demonstrated that a Mo-based SAEC featuring a distinctive O and S configuration, with a Mo loading exceeding 10 wt%, was effective for the $2e^-$ ORR. The SAEC was achieved by utilizing the integrated role of glucose chelation and defect capturing. It was observed that the specific atomic arrangement of $Mo_1/OSG-H$ complexes, like $Mo-S_4-C$ and $Mo-O_3S-C$ (shown in **Table 1**), significantly influenced the O_2 adhesion performance and reaction routes. Elsewhere, Zhou et al. [154] modulated the center Pb metal electronic structure by substituting the center metal coordination atoms with S and O (as shown in **Fig. 15g**), thereby tailoring the local coordination environment. This modification led to significantly enhanced catalytic performance, achieving an optimal activity for the $2e^-$ ORR (97% of FE and 6.9 mol $g_{cat}^{-1} h^{-1}$ under 400 mA cm^{-2} , shown in **Fig. 15h**) using Pb-based SAECs.

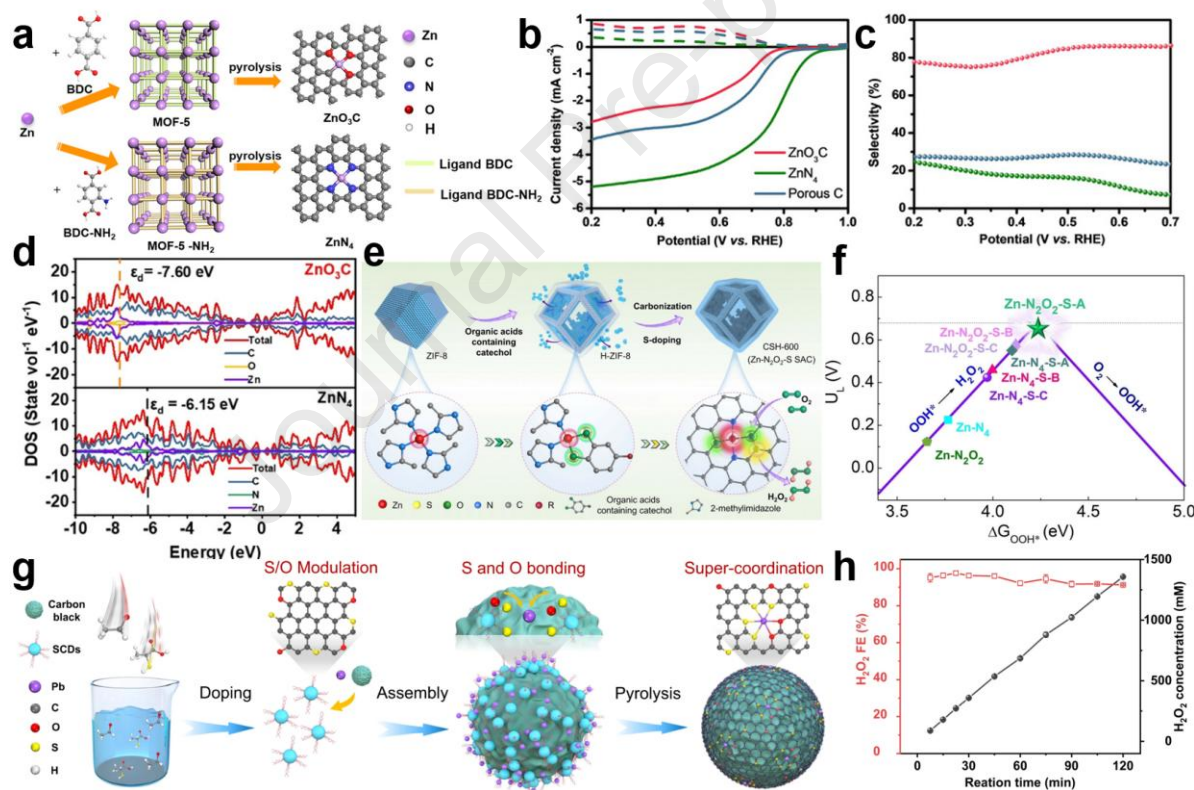


Fig. 15. (a) Illustration of the preparation process for electrocatalysts ZnO_3C and ZnN_4 . (b) LSV curves and (c) selectivity of ZnO_3C and ZnN_4 . (d) Calculated DOS of ZnN_4 and ZnO_3C ; reprinted with permission [178], Copyright 2022, Wiley. (e) Illustration of the synthetic procedures for the $Zn-N_2O_2-S$ catalyst. (f) Limiting potential volcano plot for the $2e^-$ ORR of various models; reprinted with permission [139], Copyright 2023, Wiley. (g) Schematic of the preparation route of Pb SA/OSC. (h) Accumulated H_2O_2 concentrations and Faradaic efficiencies of Pb SA/OSC at 200 mA cm^{-2} ; reprinted with permission [154], Copyright 2024, Springer Nature.

With respect to Mn-based SAECs, the occurrence of the $2e^-$ ORR has only infrequently

been documented, because of the high adsorption affinity of Mn metal centers towards OOH^* intermediates, similar to Fe metal centers. This pronounced affinity causes Mn SAECs to predominantly facilitate the $4e^-$ ORR, culminating in the conversion of O_2 to H_2O [198,199]. The selectivity of Mn SAECs has also been improved by tailoring the high-layer coordination environment for center Mn sites, which enabled a remarkable FE of 100% for the $2e^-$ ORR and an impressive H_2O_2 productivity rate of $15.1 \text{ mol g}_{\text{cat}}^{-1} \text{ h}^{-1}$ (as shown in **Fig. 16a**) [52]. In another study, Zhu et al. [180] introduced an SAEC centered on the p-block element Bi. This Bi-based SAEC featured isolated Bi sites ligated with O and S atoms, coupled with Bi nanoclusters (as shown in **Fig. 16b**). The catalyst was specifically engineered to favor the $2e^-$ ORR pathway for H_2O_2 production, achieving a selectivity of 90% at 0.3 V_{RHE} , and it could run continuously for up to 22 h in an H-type cell (as shown in **Fig. 16c**). Remarkably, both experiments and calculation analyses indicated that the active sites are constituted by Bi nanoclusters, rather than individual Bi atoms. Intriguingly, the absence of Bi single atoms led to a higher overpotential, underscoring that the enhanced property of the Bi nanocluster was facilitated by the precisely coordinated atomic separation of Bi sites. In a recent study, a class of single-site catalysts with OFG-coordinated p-block main-group metals was synthesized [200]. The investigation elucidated that OFGs facilitated the formation of electron-poor Sn sites through electronic interactions, which fine-tuned the adsorption properties of crucial intermediates, ultimately enabling the attainment of a substantial industrial current density of 300 mA cm^{-2} at a cell voltage of 1.17 V. Notably, the system exhibited an impressive energy efficiency of 43%, accompanied by robust stability spanning 200 h.

5.1.6. Dual-atom center sites

Diatomic catalysts (DACs) feature two distinct metals anchored on a support, enabling cooperative interactions to form dual-atom active sites [201]. Through the integration of alloy-like characteristics, DACs allow for precise tuning of the electronic environment around single-metal active sites, thereby achieving a nuanced optimization of catalytic reaction efficacy while concurrently impeding the aggregation of isolated atoms into metallic nanoparticles. Recent advancements in DACs have opened new frontiers in electrochemical H_2O_2 production via the $2e^-$ ORR [202–204]. Unlike conventional SACs, DACs benefit from synergistic electronic modulation and optimized O_2 adsorption configurations due to the proximity of paired metal centers. DACs can be categorized into four structural types: (i) systems featuring direct metal–metal bonding interactions; (ii) architectures incorporating heteroatom bridging moieties; (iii)

configurations exhibiting spatially isolated active sites; and (iv) structures with diatomic site coordination motifs embedded within organic framework matrices [205].

In a recent study, Liu et al. [202] reported an innovative Co–Zn DAC system wherein the Co and Zn centers are bridged via N ligands, thereby putting the Co–Zn DAC configuration into the (ii) category (as shown in **Fig. 16d**). Each metal center played a distinct functional role: Co sites facilitated the ORR, while Zn active sites steered the reaction pathway towards selective $2e^-$ reduction. Mechanistic investigations unveiled that the Zn exhibited a lower d-band center relative to the O 2p band, indicative of a more ionic or weakly covalent Zn–O interaction. In contrast to the Zn SAC, the Co–Zn DAC exhibited enhanced d–p orbital overlap and a narrower bandgap, facilitating enhanced adsorption and activation of the OOH^* intermediate. As a result, the Co–Zn DAC attained a superior TOF of 2.7 s^{-1} and 94.8% selectivity towards H_2O_2 electrosynthesis. In another study, Yu and co-workers [206] developed atomically dispersed Co/Mo sites anchored on mesoporous carbon hollow spheres (Co/Mo-MCHS) using a template-engaged strategy, as illustrated in **Fig. 16e**. In this configuration, the Co and Mo centers exhibit no direct covalent linkage, making the Co/Mo–MCHS a type (iii) DAC. Notably, the Mo centers—characterized by their pronounced electron-donating properties—induce localized electronic reconfiguration at adjacent Co coordination sites, which preferentially stabilizes the selective $2e^-$ ORR pathway. Charge density analysis revealed a reduced electron transfer (0.42 e) from the $Co_{clu}@Co/Mo-N-C$ composite to the OOH^* intermediate relative to the $Co_{clu}@Co-N_4C$ reference system (0.48 e), corroborating the attenuated interaction strength between catalytic sites and reaction intermediates in this DAC configuration. As a result, the Co/Mo-MCHS catalyst exhibited 90–95% selectivity for H_2O_2 production.

DACs can also be composed of mononuclear metal pairs. Niu et al. [203] fabricated a diatomic Co–Co catalyst, as shown in **Fig. 16f**; the diatomic Co active sites are bridged through a pair of oxygen ligands, making this a type (ii) DAC. The incorporation of a secondary Co metal into the coordination environment downshifted the d-band center, thereby weakening the OOH^* binding energy and suppressing O–O bond cleavage. This adjustment enabled a remarkable H_2O_2 selectivity of 95% and a productivity rate of $11.72\text{ mol g}_{cat}^{-1}\text{ h}^{-1}$ under 400 mA cm^{-2} in a flow-cell setup. Beyond d-block pairings, Du et al. [204] also synthesized a type (ii) DAC, Co–In DAC (**Fig. 16g**), wherein the Co and In centers were interconnected via N ligands. The oxygen-philic In atom facilitated the adsorption of hydroxyl species, thereby stabilizing the OOH^* intermediates on adjacent Co sites. This catalyst achieved a partial current

density of 1.92 mA cm^{-2} at $0.65 \text{ V}_{\text{RHE}}$ and reached a H_2O_2 production rate of $9.68 \text{ mol g}_{\text{cat.}}^{-1} \text{ h}^{-1}$ in flow conditions.

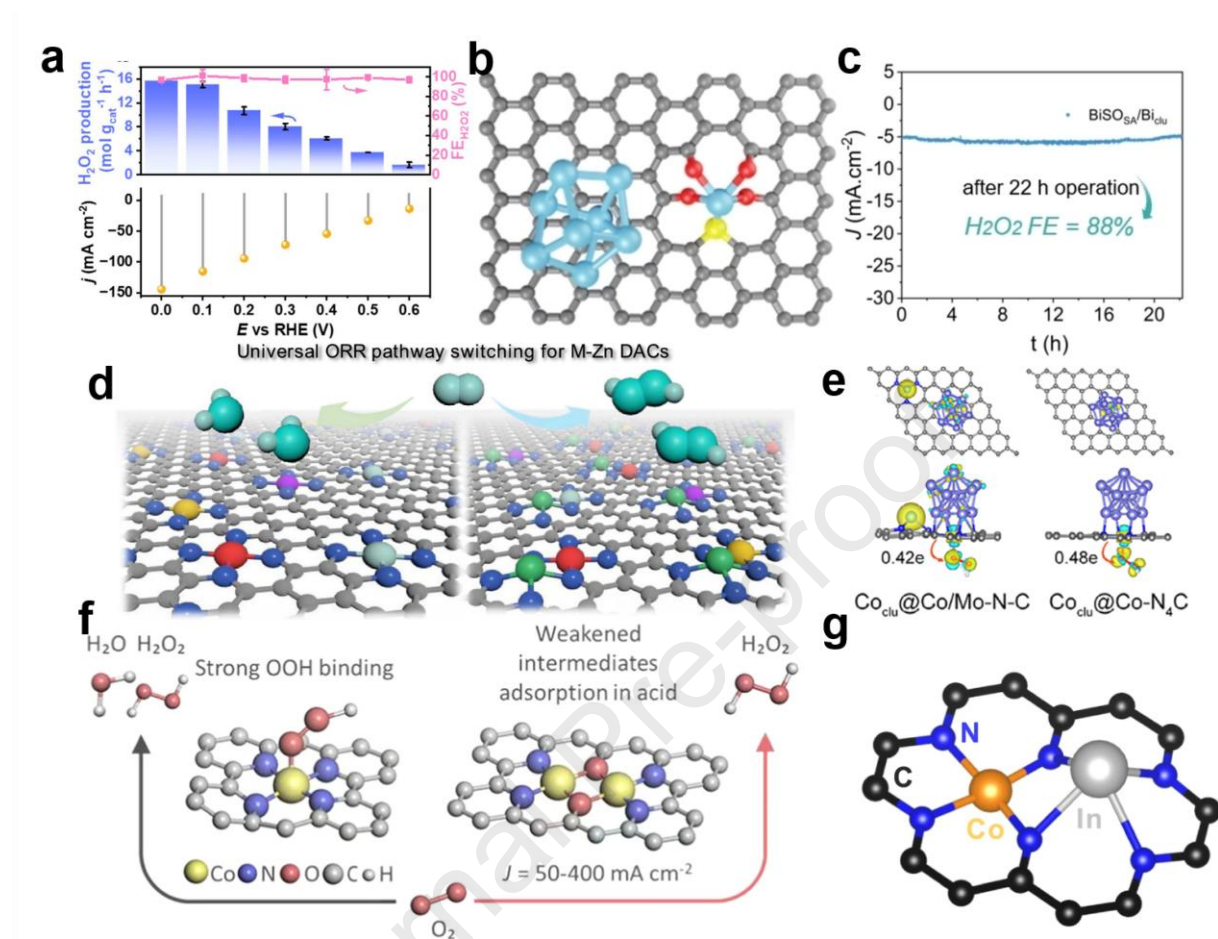


Fig. 16. (a) H_2O_2 production rate, FE, and current density at different potentials of Mn-NO-CH; reprinted with permission [52], Copyright 2024, Wiley. (b) Atomic structural model of $\text{BiOS}_{\text{SA}}/\text{Bi}_{\text{clu}}$. (c) Long-term stability test (about 22 h) of $\text{BiOS}_{\text{SA}}/\text{Bi}_{\text{clu}}$ at $0.55 \text{ V}_{\text{RHE}}$; reprinted with permission [180], Copyright 2024, Wiley. (d) Diagram for the Zn site to universally switch the 4e⁻ ORR selectivity in SACs to 2e⁻ ORR selectivity in M-Zn DACs; reprinted with permission [202], Copyright 2024, American Chemical Society. (e) Differential charge distributions on $\text{Co}_{\text{clu}}@\text{Co}/\text{Mo-N-C}$ and $\text{Co}_{\text{clu}}@\text{Co-N}_4\text{C}$ models with adsorption of OOH^* ; reprinted with permission [206], Copyright 2025, Wiley. (f) The incorporation of a secondary Co metal into the coordination environment weakened the OOH^* binding energy to enhance the 2e⁻ ORR selectivity; reprinted with permission [203], Copyright 2024, American Chemical Society. (g) Coordination structure of CoIn-N-C ; reprinted with permission [204], Copyright 2023, Springer Nature.

These investigations highlight that M-N-C SAECs are highly effective for the selective generation of H_2O_2 . Remarkably, their performance in some cases is comparable to that of noble metals. Within the M-N-C SAECs group, Co-N-C SAECs emerge as the most efficient candidates for the 2e⁻ ORR, due to their mild OOH^* adsorption properties. As compared in **Table 4**, the design of the metal active sites in M-N-C SAECs exhibits considerable variation for the 2e⁻ and 4e⁻ ORR pathways. Specifically, the 2e⁻ pathway favors metals such as Co and Ni, where their lower oxidation states and moderate OOH^* adsorption energy facilitate the

stabilization of the H_2O_2 intermediate while suppressing the O–O bond cleavage. Conversely, the 4e^- pathway leans on metals featuring higher oxidation states, such as Fe and Mn, which accelerate O_2 dissociation. Furthermore, the orbital hybridization of the metal center in its medium spin state enhances the kinetics of O–O bond breaking. Research on other types of M–N–C SAECs for the 2e^- ORR is limited but holds promise for future exploration. In a word, while Co–N–C SAECs exhibit superior 2e^- ORR catalytic performance, the optimal choice of M–N–C SAECs should align with the specific industrial requirements. In water treatment applications, Fe–N–C SAECs might be preferable, given concerns about the metal toxicity associated with Co. Similarly, Zn–N–C SAECs hold potential for practical production due to their high safety and stability. The properties of Mn–N–C SAECs can be flexibly adjusted, owing to the multiple valences of Mn (from +1 to +7). Furthermore, DACs typically exhibit bifunctional active sites, wherein each metallic site assumes a distinct functional role. For instance, one metallic site may function as the active center for the ORR, whereas the other site modulates the reaction pathway by stabilizing the OOH^* intermediate, thus promoting the selective 2e^- ORR process. Through meticulously designing diverse metallic active sites, it becomes feasible to engineer 2e^- ORR catalysts specifically tailored to various reaction systems. Ongoing advancements in this area are significantly broadening the scope and potential of H_2O_2 electrosynthesis.

5.2. Carbon substrates for M–N–C SAECs

Individual metal sites distributed at the atomic level are typically attached to the surface atoms of the supported substrates [207]. With their exceptional electric and thermal properties, carbon materials have assumed a crucial role in incorporating individual atomic metal species [194,208]. The graphitic frameworks they possess, characterized by a substantial surface area, serve to deter the aggregation of metals, ensuring remarkable catalyst stability and superior conductivity [208]. An example of a ligand configuration is the M–N_4 molecule, featuring a four-coordinated metal arrangement resembling phthalocyanine or porphyrin. Based on their dimensions, as shown in **Fig. 17**, carbon materials can be divided into three-dimensional, two-dimensional, and one-dimensional (3D, 2D, and 1D, respectively) substrates.

CNTs have a distinctive 1D configuration, hollow geometry, and ballistic carrier transfer, with comparatively intact walls, so they can significantly enhance the mass conversion of reactants and products, particularly at elevated current densities [29]. Wang et al. [186] documented that an atomically distributed Fe–C–O configuration, when embedded on

defective CNTs and coordinated with both C and O, demonstrated a remarkable H_2O_2 selectivity exceeding 95%. Calculation analyses revealed that the central Fe atoms tend to combine with C and O in the CNT vacancies to develop stable Fe–C–O configurations, as opposed to mere adsorption on the CNT surface. Moreover, the $2e^-$ ORR performance of CNTs can be substantially improved by loading OFGs onto them. To illustrate the impact of oxygen coordination on metal center atoms, Chen et al. [155] compared the $2e^-$ ORR properties of different CNT substrates. Oxygen-containing moieties on CNTs were eliminated through reducing heat processing to produce CoPc (cobalt phthalocyanine) anchored on CNT-H (hydrogen-treated CNTs), denoted as CoPc-CNT-H. The Co content on the CNT-H substrate was merely 0.17%, which was less than on CoPc-OCNT (0.30%) and CoPc-CNT (0.48%). Consequently, the CoPc-CNT-H exhibited poor H_2O_2 electrosynthesis performance. Despite the increased Co content of CoPc-CNT, its FE for H_2O_2 generation was lower compared with CoPc-OCNT, particularly at higher currents. It was deduced that the presence of modestly clustered CoPc moieties in CoPc-CNT resulted from limited interaction between cobalt sites and an inadequate quantity of oxygenated moieties on the CNT. This observation underscored the essential role of adequate oxygen modification in enhancing the catalytic properties of metal centers.

It is believed that the almost completely exposed surface atoms in 2D carbon supports are responsible for significantly enhancing the efficiency of utilizing atomic metal centers. Consequently, a 2D substrate featuring a consistent surface configuration serves as an optimal foundation for the formation of precisely defined M–N–C SAECs [209]. Many researchers are particularly interested in M–N₄ SAECs supported on graphene. Firstly, graphene-backed M–N–C SAECs can be seen as metallic cores encircled by ligands with a porphyrin-like character. Secondly, due to having a great deal of dangling bonds, the lattice fringes in graphene substrates might offer greater adjustability than the basal plane [210]. This flexibility could be advantageous for optimizing catalytic properties. Zhang et al. [211] immobilized individual Co species onto oxidized graphene oxide, creating active Co–O–C motifs (named Co₁@GO) that exhibited notable performance for H_2O_2 production. They conveyed that the impressive performance of Co₁@GO for H_2O_2 generation stemmed from the collaborative effect between the individually oxygen-bonded Co atoms and the neighboring C–O bonds.

3D porous carbon materials are typically defined by their well-developed pore structures, which can consist of macropores (diameter > 50 nm), mesopores (2 nm < diameter < 50 nm), and/or micropores (diameter < 2 nm) [212]. When using 3D carbon structures as supports for

M–N–C SAECs in electrochemical reactions, it is crucial that these structures exhibit high porosity and a well-distributed pore size [213]. The defects, particularly sp^3 -C, are considered sites for oxygen sorption and reduction. In addition, the large surface volume and 3D stratified porous shape of the electrocatalyst guarantee efficient exposure of the reactive sites, along with alleviation of mass transfer and diffusion resistance [214]. Wu and colleagues [215] developed stratified Ni-based SAECs through carbon dot impregnation and regulated MOF pyrolysis. These Ni–N–C SAECs harnessed a 3D self-supporting framework, accordingly harvesting a $2e^-$ ORR potential of 0.78 V at 1.0 mA cm^{-2} and an optimal H_2O_2 production rate of $325 \text{ mmol g}_{\text{cat}}^{-1} \text{ h}^{-1}$ with a lifespan of 30 h.

In summary, 1D CNTs are favored for their unique hollow structure and superior electronic conduction properties, making them commonly used substrates for dispersing metal atoms. 2D carbon-based materials (e.g., graphene), with fully exposed planar structures, offer optimal efficiency in utilizing reactive species. 3D carbon substrates (such as 3D MOFs and carbon black), leveraging defect structures on surfaces as active embedding sites for single metal atoms, are increasingly used in M–N–C SAECs. In addition, the hydrophilicity of the substrate greatly affects the ORR selectivity, as outlined in **Table 4**. For the $2e^-$ ORR, the utilization of hydrophobic carbon supports, such as fluorinated or hydrocarbon-functionalized surfaces, effectively mitigates H_2O_2 decomposition by reducing its interfacial capture, ultimately enhancing selectivity. The resulting hydrophobic microenvironment stabilizes OOH^* intermediates via subtle intermolecular forces while also optimizing the adsorption of O_2 at the gas–liquid–solid tripartite interface [7]. Conversely, for the $4e^-$ ORR, a hydrophilic substrate catalyzes rapid mass transfer of the reactants and facilitates O–O bond cleavage by forming an ultrathin hydrated layer, which diminishes the charge transfer resistance and accelerates the reaction kinetics [216]. In a word, when selecting carbon substrates for anchoring separated atoms, it is essential to not only evaluate the properties of carbon materials but also comprehensively account for the structural characteristics of metal atoms and the impacts that modification methods have on the carbon substrates.

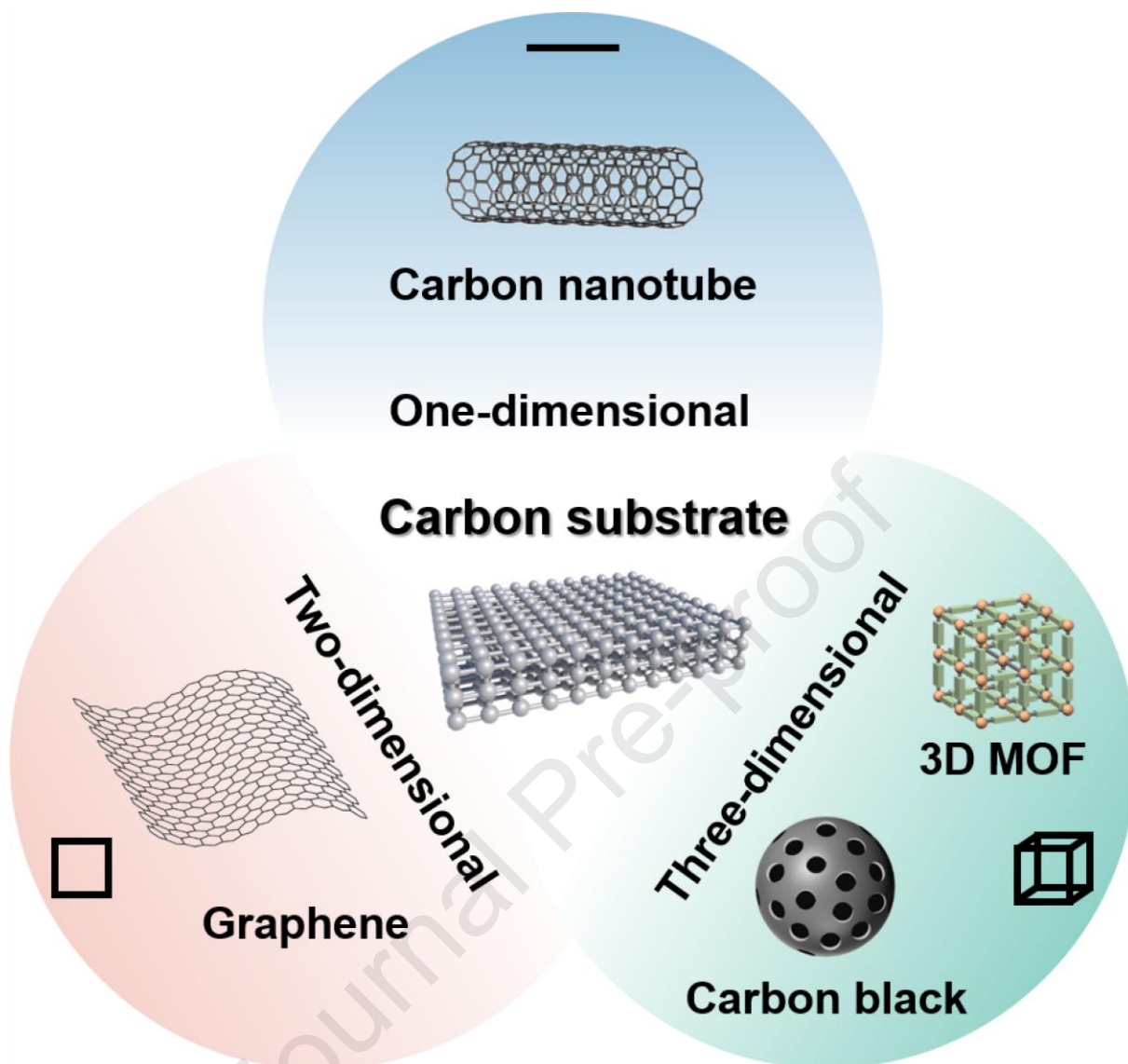


Fig. 17. Schematic illustration of carbon substrates for H_2O_2 -producing M–N–C SAECs using the 2e^- ORR.

5.3. Optimization of coordination environment to improve M–N–C SAEC activity

5.3.1. Modification of the first coordination surroundings

The hybridization between metal d-orbitals and ligand p-orbitals determines the spatial and energetic distribution of antibonding states (e.g., OOH^* –metal interactions). Stronger sp^3 -d hybridization can stabilize OOH^* intermediates while preventing excessive adsorption that could trigger O–O cleavage [217]. As illustrated in **Fig. 18**, it is recognized that optimizing the coordinative environments (including the structures, categories, and quantities of bonded atoms) is beneficial for modulating the catalytic properties. Unlike in the typical M–N₄ structure featuring even bond strengths, electron precipitation in the M–O configuration efficiently reduces the d-band center of the metal, which is favorable for the 2e^- route, as it reduces the

adhesion ability of OOH^* [178].

Within M–N–C SAECs, the ORR properties are primarily influenced by the atomic arrangement of the M–N_x units. Shen et al. [218] documented that Co-based SAECs featured a penta-coordinated Co–N–C arrangement (O–Co–N₂C₂, shown in **Table 1**). The selectivity of the acquired Co–N–C SAEC for H₂O₂ was more than 90%. A sophisticated X-ray characterization methodology and calculation analyses were employed to explore the partial configuration and coordination surroundings of individual Co atoms, which shed light on the recombination of charge distributions in the Co single atom, indicating that the O–Co–N₂C₂ inherently facilitated the reduction of O₂ to H₂O₂ better than the common Co–N₄ configuration. In addition to O atoms, Wu et al. [219] explored the efficacy of generating H₂O₂ using Co SAECs coordinated with various heteroatoms (designated as Co₁S₁N₃, Co₁N₁N₃, and Co₁P₁N₃, shown in **Table 1**) and found that the S-coordinated Co was optimal for catalysis. In a recent study conducted by Liu et al. [167], a range of ultralow metal-content M–N–C SAECs featuring an asymmetric Co–C/N/O arrangement were synthesized. In contrast to the widely acknowledged square-planar symmetric Co–N₄ configuration, the asymmetric Co–C/N/O configurations demonstrated a propensity for enhanced dipole-forbidden 1s to 3d electron transitions at the pre-edge position, attributed to heightened 3d and 4p orbital hybridization. Furthermore, the characteristic square-planar symmetry signature at the shoulder peak position was absent across all asymmetric configurations. Relative to the Co–N₄ configuration, all of the asymmetric configurations exhibited reduced adsorption affinity for OOH^* intermediates, leading to exceptional mass activity ($6.1 \times 10^5 \text{ A g}_{\text{Co}}^{-1}$ at 0.5 V vs. RHE) and an elevated H₂O₂ production rate ($4.72 \text{ mol g}_{\text{cat.}}^{-1} \text{ h}^{-1} \text{ cm}^{-2}$) in neutral environments.

A recent study has also revealed that the coordination of S and O atoms with Pb metal sites could significantly alter the electronic structure of the center metal atoms to form the PbS₄O₂ moiety, leading to a reduction in the adsorption energy for the OOH^* intermediates and facilitating the achievement of over 90% FE in alkaline electrolytes within a voltage range of 0.4–0.6 V_{RHE} [154]. It is important to mention that the sites for incorporating reactive intermediates may not be individual metal entities. For example, Qiao and coworkers [49] described Co-based SAECs with N, O double coordination that demonstrated exceptional performance for the 2e[−] ORR. The computations indicated that the preferred location for OOH^* adsorption on the Co–N₂O₂ configuration was the carbon atom next to the coordinated O atom, rather than the single Co atom.

5.3.2. Modification of the second coordination surroundings

The ligand-to-metal charge transfer (LMCT) effect governs the electron density redistribution between ligands and metal centers in M–N–C SAECs, thereby influencing the d-band position of the metal site. For instance, electron-withdrawing ligands can enhance LMCT, weakening OOH* adsorption by lowering the metal's d-band center. This modulation is critical for suppressing O–O bond dissociation and promoting 2e⁻ ORR selectivity [206]. The local ligand surroundings of M–N–C SAECs will be reconstructed by replacing or inserting other non-metallic components with isolated pairs of electrons (like B, N, P, O, and S) into the pristine ligand configuration at the high coordination layer [220,221]. This contributes dynamic electrons in the central atoms, modifies the electronic configuration of the reactive center, and influences the coordinated intensity of the intermediates [179]. S atoms have been used to adjust the high coordination layer of M–N–C SAECs. Wei et al. [139] devised a universal two-phase method for producing hollow carbon-supported Zn–N₂O₂–S SAECs, distinguished by an imbalanced Zn–N₂O₂ component influenced by S atoms in higher coordination spheres.

Incorporating electron-poor H* or electron-abundant O* has distinct impacts on the charge status and combining energy of the ORR intermediates in M–N–C groups. In a recent study, a 2D COF featuring dithiine-linked phthalocyaninato cobalt, designated as CoPc-S-COF, was synthesized [222]. The incorporation of S atoms, characterized by their substantial atomic radius and possession of two lone-pair electrons within the C–S–C linkage, induced a wavy layered architecture and augmented the electron density at the Co center within CoPc–S–COF. This structural modification facilitated greater exposure of Co sites, thereby enhancing the COF's catalytic proficiency. Concurrently, the electronic modification selectively promoted the 2e⁻ ORR pathway while inhibiting the H₂O₂ decomposition capacity of the same Co center. As a result, CoPc–S–COF exhibited a H₂O₂ selectivity exceeding 95%. It is worth noting that the charge status disparities of the Co atom might explain the influence of electron-abundant and electron-deficient species on the combining energy of OOH*. Drawing on theoretical insights, researchers created Co₁–NG(O) featuring electron-enriched oxygen entities around the Co sites, which demonstrated preferential production of H₂O₂ in 0.1 M HClO₄ solution [48].

The tuning of OFGs at the high coordination sphere of a M–N–C SAEC structure is also essential for selectively facilitating the 2e⁻ ORR pathway. Zhang and coworkers [94] developed a Co and N co-doped CNTs compound called CoN@CNTs. They discovered that suitable handling could efficiently modulate the OFGs around distributed Co atoms, presenting a viable

approach to enhance H_2O_2 production. A two-step electrochemical approach, encompassing both electrochemical oxidation and reduction, was implemented to alter the OFGs on CoN@CNT , resulting in a notable selectivity exceeding 90% and an onset potential of 0.7 V. Characterization analyses corroborated that the cooperative interactions between the Co-N_4 configuration and the neighboring C-O-C moiety were pivotal in the O_2 to H_2O_2 reduction process. Tuning the electronic structure of Mn-N-C SAECs with OFGs at high coordination spheres can effectively improve the selectivity for the 2e^- ORR. In a study conducted by Dong et al. [52], carbons rich in boundaries, supporting active Mn(II) centers and selectively endowed with OFGs, were meticulously designed and prepared. The Mn-based SAECs showed a FE for the 2e^- ORR of 100% and a H_2O_2 production rate of $15.1 \text{ mol g}_{\text{cat.}}^{-1} \text{ h}^{-1}$ at 0.1 V_{RHE} in 1 M KOH electrolyte. The DFT results indicated that the Mn center with C-O-C and OH groups showed the lowest ΔG (-0.96 eV) for the 2e^- ORR pathway among all of the models, illustrating that the existence of C-O-C and OH groups induced an electron-deficient condition at the individual Mn site, resulting in more modest shifts in the Mn valence.

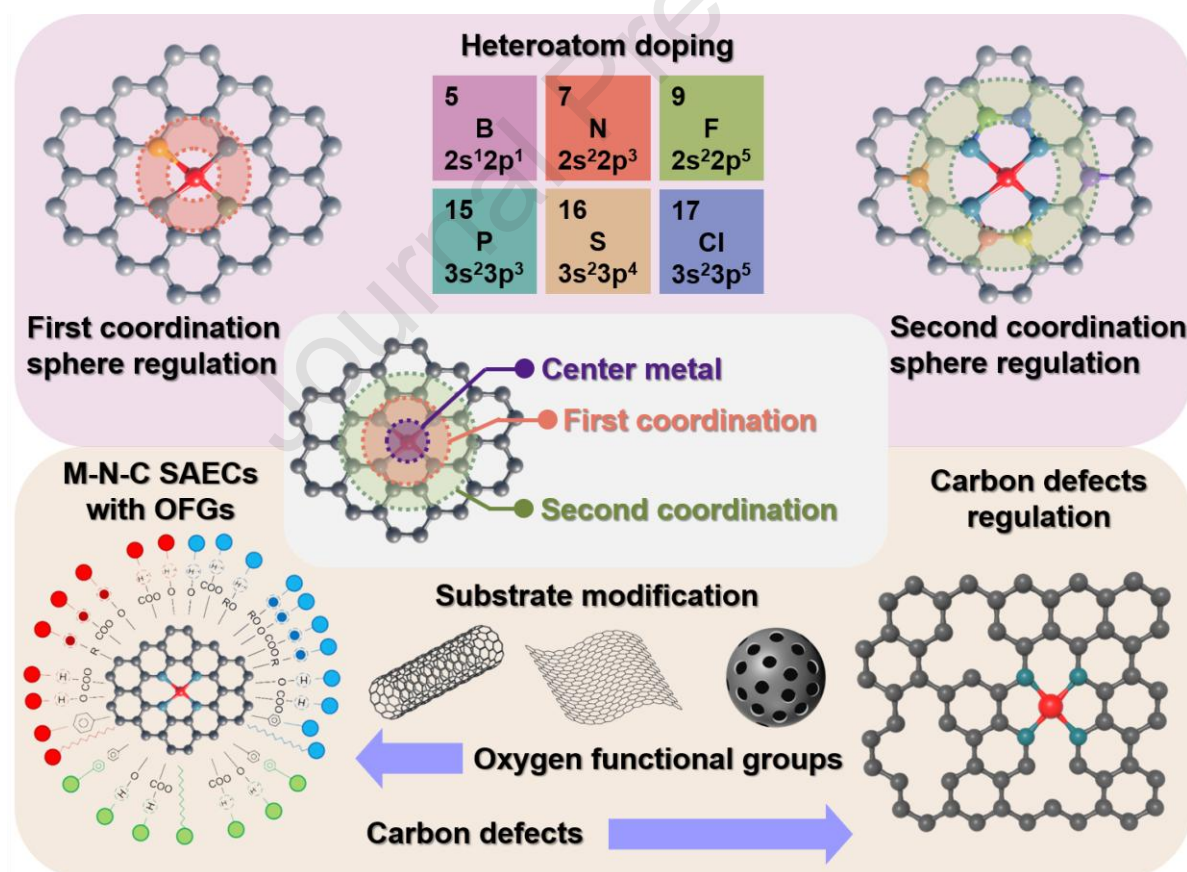


Fig. 18. Coordination environment engineering strategies for constructing advanced M-N-C SAEC electrocatalysts for the 2e^- ORR.

5.3.3. Alteration of the coordination numbers

Adjusting the number of ligand atoms in M–N–C SAEs is a viable approach to enhance the catalysts' properties. Usually, the metal core in M–N_x–C SAEs is bonded to four N atoms, forming a thermodynamically steady structure. This ligand arrangement may not exhibit the most favorable combining properties for oxidized intermediates [50,119]. The pyrolysis temperature is a commonly employed approach for adjusting coordination numbers. Taking the example of the Co–N₅ configuration (shown in **Table 1**), modifying the ligand number presents a practical approach to improve the barrier for O₂ adhesion, leading to desirable properties for the 2e[−] ORR. In particular, Shao and colleagues [164] reported an innovative approach for crafting the Co–N₅ configuration to guide H₂O₂ generation. As illustrated in **Fig. 19a**, a homogeneous blend of Co cations, triquinoxalinyne, NaCl, and carbon black underwent pyrolysis at 700 °C, resulting in the formation of the Co–N₅ configuration. **Fig. 19b** indicates a ligand number of 5.2 for the Co atoms. The optimal SAE exhibited a favorable performance for H₂O₂ production, with an elevated FE of 96% under neutral conditions. According to the calculation results, the Co–N₅ configuration favored the 2e[−] ORR, which was primarily attributed to it presenting a lower kinetic barrier than Co–N₄ (**Fig. 19c**). Specifically, the activation and reduction of *O₂ at the Co–N₅ site are thermodynamically more beneficial than at the Co–N₄ site, thus enhancing electrocatalytic H₂O₂ generation.

In recent research, the concurrent adjustment of OFGs and ligand numbers in a Co–N–C SAE was effectively achieved through a microwave irradiation processing approach, as shown in **Fig. 19d** [119]. Microwave irradiation has been utilized to synthesize Co–N₂–C/HO catalyst, promoting the alleviation of atom movement/agglomeration in contrast to a conventional elevated temperature heating strategy [118,223]. Structural analysis verified that the ligand number of the center Co atom was approximately 2.0. Collaborative tests and a set of computational results also confirmed that the catalyst's exceptional property could be ascribed to the synergistic impact of the low-coordinated Co–N₂ structure and the adjacent epoxy moieties. In general, the restricted and undersaturated coordination surroundings of M–N–C SAEs enhance 2e[−] ORR performance by providing versatility and adjustability in the required reactions. However, the long-term durability of these low-coordinated M–N_x sites during the reaction process still requires further exploration.

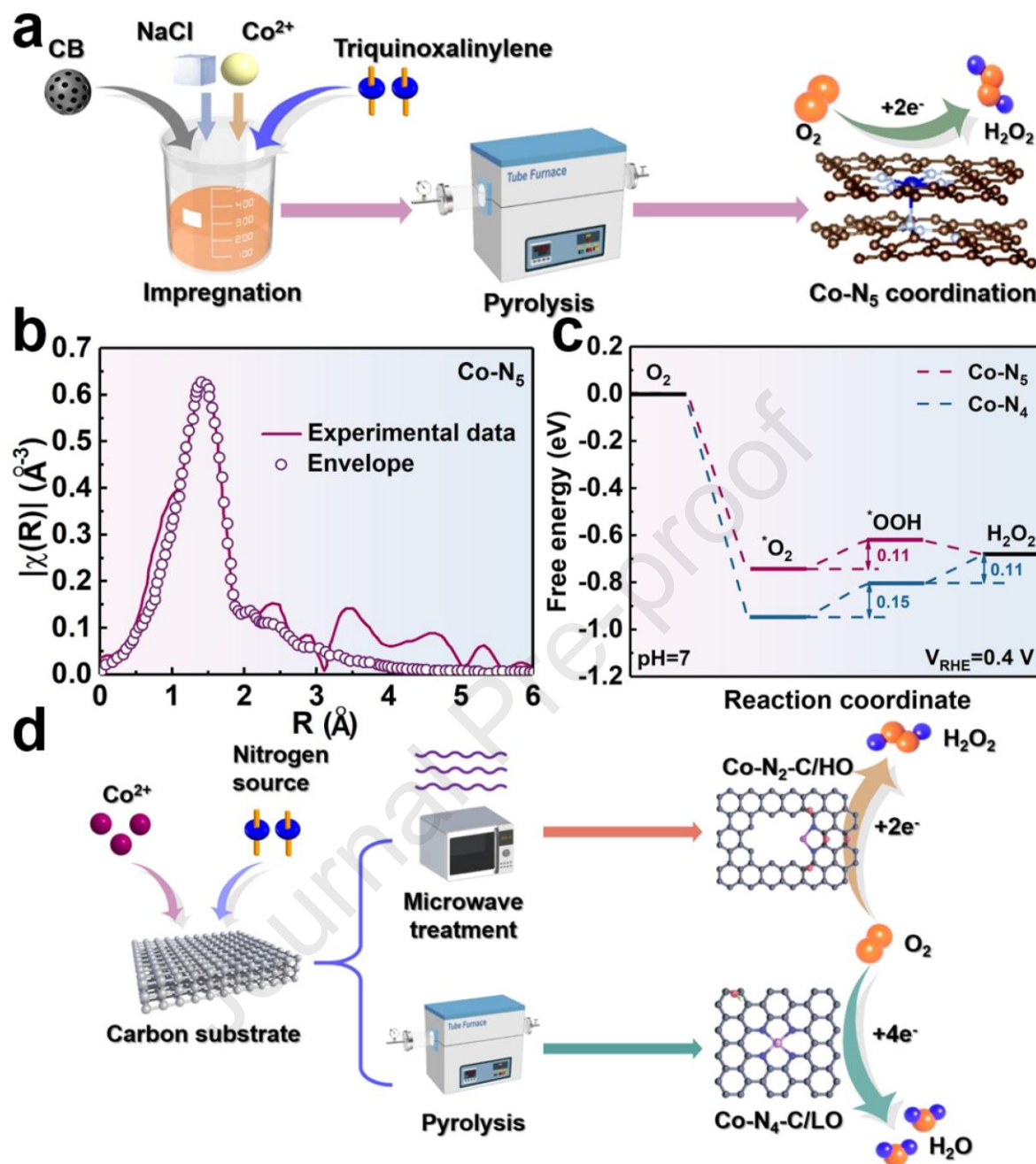


Fig. 19. (a) Schematic synthesis of a nitrogen-coordinated cobalt single-atom catalyst (Co-N-C). (b) FT-EXAFS fitting curve of Co-N-C in R space. (c) Gibbs free energy diagram of the $2e^-$ ORR pathway on the Co-N₅ and Co-N₄ structures; reprinted with permission [164], Copyright 2021, Royal Society of Chemistry. (d) Schematic diagram of the synthesis routes to Co-N₄-zC/LO and Co-N₂-C/HO; reprinted with permission [119], Copyright 2022, Wiley.

In summary, single metal atoms anchored on carbon supports can establish strong chemical bonds with surrounding atoms in the first coordination sphere. The directional modulation of the neighboring atoms proves instrumental for enhancing the selectivity of M-N-C SAECs. As summarized in **Table 4**, crafting asymmetric coordination configurations for metal active sites

(such as M–N₂O₂, M–N₃S, etc.) holds promise for enhancing 2e[−] ORR selectivity. The introduction of O or S atoms alters the electron assignment surrounding metal atoms, thereby mitigating the adhesion of intermediate OOH* and ultimately enhancing the selectivity of the 2e[−] ORR. These asymmetric frameworks effectively reduce the simultaneous, parallel adsorption of O₂, compelling it to adopt an end-on adsorption configuration and hindering O–O bond cleavage. Conversely, high coordination symmetry structures favor the 4e[−] ORR, as they bolster metal–carrier interactions, stabilize intermediary species of O* and OH*, and facilitate the sequential disruption of the O–O bond. In addition, incorporating heteroatoms with lone pairs of electrons and functional groups into M–N–C SAEC structures changes the electron distribution and affects the catalytic active sites of the high coordination shells. Plus, the ligand number of the core metal atom can be altered by regulating the pyrolysis conditions and using microwave assistance, thus improving the catalytic activity.

Table 4. Comparison of the M–N–C SAECs used in the 2e[−] and 4e[−] ORR in terms of the selection of metal center sites, carbon substrates, and the coordination configurations of M–N–C SAECs.

Reaction	Center metal site	Carbon substrates	Coordination configurations
2e [−] ORR	Lower oxidation states (like Co and Ni)	Hydrophobic substrates to protect O–O bond	Asymmetric coordination configuration to boost O ₂ end- on adsorption
4e [−] ORR	Higher oxidation states (like Fe and Mn)	Hydrophilic substrates to facilitate O–O bond cleavage	Symmetric coordination configuration to boost O ₂ side- on adsorption

5.4. Aqueous electrolytes for H₂O₂ production

5.4.1. Alkaline electrolytes

Electrolytes not only affect the performance of catalysts but also influence the lifespan of reactors [224,225]. In particular, factors such as the pH, electrolyte concentration, and solvent varieties jointly influence the effectiveness and production rate of electrochemically generated H₂O₂. It was observed that M–N–C SAECs demonstrated greater catalytic efficiency in an alkaline electrolyte than in one with a low pH (as shown in **Table 5**), because a high OH[−] content can inhibit side reactions, such as the hydrogen evolution reaction (HER), and increase the selectivity for the 2e[−] ORR (**Fig. 20**) [80]. With respect to Fe–N–C SAECs, it was observed that the pH level markedly affected the chemical conditions of the surface and the availability of Fe–N_x moieties [226]. When the pH was less than 10.5, protons on the surface of Fe–N–C

SAECs, such as protonated nitrogen and carbon groups, could neutralize the OH^- ions that were specifically adsorbed, aiding in generating H_2O via the 4e^- ORR pathway. Conversely, when the pH levels were higher than 10.5, Fe-N_x sites could attract surplus OH^- ions, which was advantageous for synthesizing H_2O_2 . Overall, weak oxygen attachment on the surface of M–N–C SAECs resulted in a significant reliance on the electrocatalytic efficiency as determined by the electrolyte's pH.

A major challenge is the self-decomposition of H_2O_2 due to its instability in alkaline media. Given its acid dissociation constant ($\text{pK}_a = 11.7$), H_2O_2 exists primarily as HO_2^- in conditions where the pH exceeds 11.7, as illustrated in **Fig. 20**. Chelating agents like ethylene diamine tetra acetic acid are necessary to prevent this decomposition, thereby increasing operational costs. Another significant issue is the suboptimal performance, durability, and ionic conductivity of typical AEMs in H_2O_2 electrolyzers.

5.4.2. Acid electrolytes

Although the encouraging progress in developing M–N–C SAECs for the electrocatalytic formation of H_2O_2 in alkaline environments has received considerable research attention, H_2O_2 decomposes quickly upon the accumulation of HO_2^- ($\text{H}_2\text{O}_2 + \text{HO}_2^- \rightarrow \text{H}_2\text{O} + \text{O}_2 + \text{OH}^-$) in alkaline media [186,227,228]. Therefore, the electrochemical production of H_2O_2 is more appropriate for practical applications in acidic and neutral media. Researching Co–N–C SAECs, Lu and colleagues [165] synthesized an individual graphene electrode decorated by Co atoms that demonstrated desirable performance for the 2e^- ORR; with a H_2O_2 production rate of $4 \text{ mol g}_{\text{cat.}}^{-1} \text{ h}^{-1}$ and a FE of 100%, it was able to maintain stable operation for 6 h in a flow cell with 0.1 M HClO_4 electrolyte. Their acid production makes Co–N–C SAECs highly viable for a variety of downstream utilities involving on-site H_2O_2 production, such as the Fenton reaction for pollutant degradation.

Apart from modifying a catalyst's intricate structure to enhance its 2e^- ORR selectivity in acidic electrolytes, adjusting the catalyst loading can also impact its catalytic efficiency across varying pH solutions. In a study conducted by Zhang and co-workers [163], they prepared a Co–N–C SAEC with the Co– N_4 moiety and carbon black as the carbon substrate. This SAEC demonstrated ideal 2e^- ORR performance in an acid electrolyte (80% selectivity and $5.04 \text{ mol g}_{\text{cat.}}^{-1} \text{ h}^{-1}$ production rate in 0.5 M H_2SO_4). This was because the robust interaction between the pyridinic N within the Co– N_4 active sites and the H^+ diminished the electron density on the central Co atom, subsequently attenuating the binding energy of HOO^* [229] and thereby

facilitating H_2O_2 generation. Additionally, they found that when the Co–N–C SAEC loading was $25 \mu\text{g cm}^{-2}$ or even less, the H_2O_2 yield exceeded 80%, but if the catalyst loading increased to $400 \mu\text{g cm}^{-2}$ the H_2O_2 yield decreased to 25% in 0.5 M H_2SO_4 ; this was also observed, to a lesser extent, in alkaline and neutral electrolytes. These results indicated that reducing the catalyst loading, specifically by employing a thin CL, diminishes the likelihood of electrochemical/chemical decomposition of newly formed H_2O_2 within the CL.

5.4.3. Neutral electrolytes

Neutral electrolytes (e.g., K_2SO_4 , Na_2SO_4 , and NaCl) have gained attention for their use in H_2O_2 production due to their environmentally benign characteristics and reduced corrosiveness, and the potential to decrease electrolyzer operating costs [164,230,231]. Furthermore, neutral H_2O_2 offers a sustainable and versatile option for real-world scenarios involving the direct employment of the produced H_2O_2 in biochemical systems [7,186,232]. Using NaCl electrolyte for H_2O_2 electrosynthesis can effectively reduce the operating cost of the reactor, since it can be replaced by seawater. Furthermore, the use of NaCl as an electrolyte facilitates the production of Cl_2 at the anode. This concurrent generation of Cl_2 and H_2O_2 presents a valuable industrial opportunity, given the high commercial value of both chemicals [164]. Despite the promising aspects of utilizing neutral electrolytes for H_2O_2 electrosynthesis, reports on M–N–C SAECs demonstrating high activity in such conditions are scarce.

In summary, alkaline electrolytes (like KOH) effectively inhibit the side reactions and boost the $2e^-$ ORR for H_2O_2 production. However, in high pH solutions, H_2O_2 tends to decompose, necessitating the use of stabilizers to maintain its stability, which in turn raises production costs. Conversely, acidic electrolytes like HClO_4 and H_2SO_4 significantly improve H_2O_2 stabilization, but a high concentration of H^+ may lead to the occurrence of undesired side reactions (like the HER) at the cathode, highlighting a critical trade-off, as illustrated in **Fig. 20**. Hence, there is an imminent need to advance the development of M–N–C SAECs tailored for efficient H_2O_2 production, and specifically for use in acidic environments. For practical applications, neutral electrolytes such as NaCl and Na_2SO_4 offer considerable advantages. Notably, the utilization of seawater as a neutral electrolyte can dramatically reduce operational costs, presenting a sustainable and cost-effective solution for H_2O_2 production on a larger scale. It is important to develop M–N–C SAEC-catalyzed H_2O_2 generation in neutral electrolytes. Each type of electrolyte has its strengths and restrictions, and the selection should also consider the particular demands of the H_2O_2 usage scenarios.

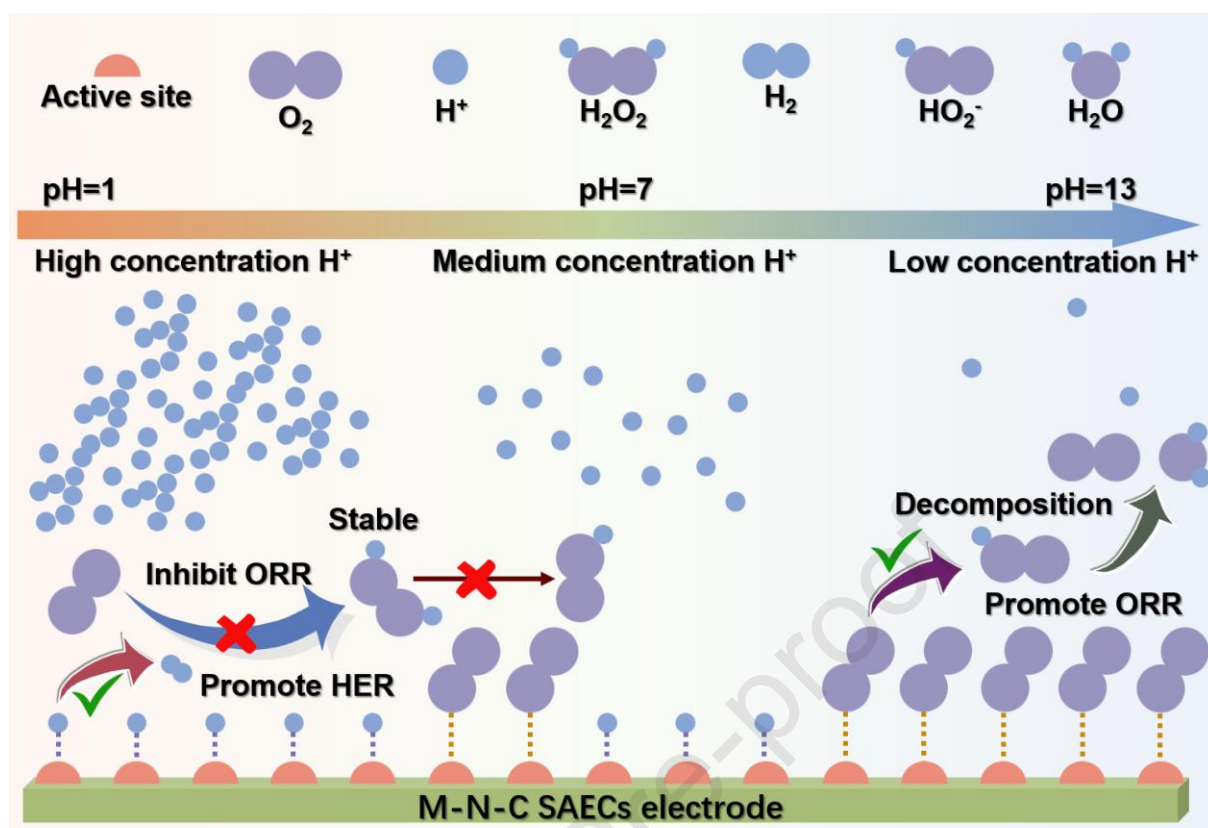


Fig. 20. The $2e^-$ ORR mechanism in different pH electrolytes.

Table 5. The electrochemical catalytic performance of M–N–C SAECs for H₂O₂ production via the 2e[−] ORR.

Electrocatalysts	Substrate	Metal content (wt%)	Electrolyte	Reactor	Selectivity	H ₂ O ₂ generation rate (mol g _{cat.} ^{−1} h ^{−1})	Ref.
CB@Co-N-C	Carbon black	1.2	0.5 M H ₂ SO ₄	Flow cell	54–74% (0.2–0.6 V _{RHE})	5.0	[163]
Co-N-C	Carbon black	1.0	0.5 M NaCl	Flow cell	58–93% (0.2–0.55 V _{RHE})	4.5	[164]
CoN ₄ /VG	Graphene	—	0.1 M HClO ₄	Flow cell	65–90% (0.3–0.6 V _{RHE})	4.0	[165]
CoTPP@RGO-160	Graphene	1.14	0.5 M H ₂ SO ₄	Flow cell	88–99% (0.05–0.45 V _{RHE})	21	[166]
CoNCB	Carbon black	0.05	1M PBS	Flow cell	71–97% (0.2–0.8 V _{RHE})	1.18	[167]
CoPc-OCNT	OCNT	0.3	0.1 M KOH	Flow cell	80–97% (0.3–0.65 V _{RHE})	11.5	[155]
Co HSACs	CNT	3.4	0.5 M KOH	Flow cell	92–95% (0.5–0.8 V _{RHE})	9.6	[168]
Co-N ₅ -O-C	Carbon black	1.4	1.0 M KOH	Flow cell	80–85% (0.3–0.8 V _{RHE})	11.3	[169]
CoN ₄ -PC	Aerogel	0.5	1.0 M KOH	Flow cell	90–96% (0.1–0.7 V _{RHE})	11.2	[170]
CoPc-CNT(O)	OCNT	1.0	SE	Flow cell	84–96% (0.2–0.6 V _{RHE})	26.1	[51]
CoPorF/CNT	CNT	0.2	SE	Flow cell	86–88% (0.2–0.53 V _{RHE})	10.8	[171]
Co-N ₃ O	ZIF-8	0.76	1 M KOH	Flow cell	86–87% (0.05–0.65 V _{RHE})	14.2	[172]
Ni-N ₂ O ₂ /C	Carbon black	2.0	0.1 M KOH	H-type cell	89–96% (0.1–0.5 V _{RHE})	5.9	[92]
Ni-TCPP(Co)	TCPP	6.78	1 M KOH	Flow cell	90–97% (0.0–0.8 V _{RHE})	18.2	[173]

Electrocatalysts	Substrate	Metal content (wt%)	Electrolyte	Reactor	Selectivity	H ₂ O ₂ generation rate (mol g _{cat.} ⁻¹ h ⁻¹)	Ref.
Ni-SAC	Carbon cloth	1.59	0.1 M KOH	Flow cell	43–70% (0.0–0.8 V _{RHE})	7.3	[174]
Ni-N ₃ S	ZIF-8	0.93	1 M KOH	Flow cell	82–92% (0.05–0.65 V _{RHE})	17.5	[172]
Ni-SACs@OCB	Carbon black	4.83	0.1 M KOH	H-type cell	85–99% (0.2–0.7 V _{RHE})	0.0985	[175]
FeN ₂ O ₂ /HNC	HNC	4.5	0.1 M KOH	H-type cell	85–89% (0.2–0.8 V _{RHE})	0.825	[176]
FeSAs/ACs-BCC	Bacterial cellulose	0.5	0.1 M KOH	Flow cell	89–96% (0.2–0.7 V _{RHE})	12.5	[112]
FeSA-NS/C-700	MIL-88	0.48	0.1 M KOH	Flow cell	71–91% (0.3–0.6 V _{RHE})	5.0	[153]
Fe-O/C	Graphitic carbon	1.2	1 M KOH	H-type cell	95–98% (0.4–0.7 V _{RHE})	33.5	[177]
CSH-600	ZIF-8	4.4	0.1 M KOH	Flow cell	83–96% (0.1–0.65 V _{RHE})	6.9	[139]
ZnO ₃ C	MOF-5	0.7	0.1 M KOH	H-type cell	74–87% (0.2–0.7 V _{RHE})	0.35	[178]
Mo ₁ /OSG–H	Graphene	10.0	0.1 M KOH	RRDE	90–95% (0.35–0.75 V _{RHE})	—	[179]
Pb SA/OSC	Carbon black	1.2	1.0 M KOH	Flow cell	90–97% (0.3–0.75 V _{RHE})	6.9	[154]
Mn-NO-C _H	Bacterial cellulose	—	1.0 M KOH	Flow cell	86–98% (0.0–0.6 V _{RHE})	15.1	[52]
BiOS _{SA} /Bi _{clu}	CAU-17	0.1	0.1 M KOH	H-type cell	85–97% (0.4–0.7 V _{RHE})	5.8×10 ⁻⁴	[180]
Sb-NSCF	Carbon nanofiber	10.32	1.0 M KOH	Flow cell	90–98% (0.4–0.7 V _{RHE})	7.46	[181]

6. Reactor design and regulation for H₂O₂ production

6.1. Reaction generator

Besides the significance of M–N–C SAECs highlighted earlier, the development of novel cell designs is also essential to bridge the performance disparity between the laboratory and industrial scales. The FE of cells for electrocatalytic H₂O₂ generation through the 2e[−] ORR is measurable using **Equation** (17). Similarly, the related energy efficiency (electricity-to-H₂O₂ efficiency, λ_{EE cell}%) can be calculated using **Equation** (18) [57].

$$\text{FE of cell } (\lambda_{\text{FE cell}}\%) = \frac{2 \times n \times F}{C} \quad (17)$$

$$\text{Efficiency of cell } (\lambda_{\text{EE cell}}\%) = \frac{(E_{\text{anode}}^0 - E_{\text{cathode}}^0) \times \lambda_{\text{FE cell}}}{V_{\text{cell}}} \quad (18)$$

where n is generated H₂O₂, mol; F is the Faraday constant, 96485 C mol^{−1}; C is the sum of charge passing through, C; E_{anode}⁰ is the theoretical potential of the anodic reaction, V; E_{cathode}⁰ is the theoretical potential of the cathodic reaction, V; and V_{cell} is the uncompensated cell voltage, V.

6.1.1. Rotating ring disk electrode

As shown in **Fig. 21a**, the RRDE within a tri-electrode system presents a potent and direct approach for quantifying H₂O₂ production from the 2e[−] ORR. Unlike catalytic assessments in actual electrochemical setups, RRDE experiments are more straightforward to fine-tune and typically produce highly accurate outcomes in a laboratory environment. The ORR occurs on the disk electrode, as indicated in **Equations** (19) and (20) [233]. H₂O₂ formed at the disk electrode undergoes radial transfer to the adjacent Pt ring electrode due to the induced conveyance from the electrode's rotation. Following this, H₂O₂ is re-oxidized to O₂ on the ring electrode, as expressed in **Equation** (21) [88]. The selectivity of the disk and ring currents, indicating the efficiency of H₂O₂ production and subsequent oxidation, can be quantified using the FE, as shown in **Equation** (22).

Disk:



Ring:



$$\text{FE (\%)} \lambda_{\text{Faradaic}} = 100 \times \frac{I_{\text{R/N}}}{I_{\text{D}}} \quad (22)$$

The electrochemical properties of heterogeneous M–N–C SAECs for the ORR to H_2O_2 are typically investigated by applying the RRDE method [74,234]. The molar fraction indicating H_2O_2 selectivity is ascertainable by recording the O_2 reduction current on the disk and the H_2O_2 oxidation current on the Pt or Au ring of the RRDE, as expressed in **Equation** (23). The n value can also be calculated using the RRDE test; see section 2.3 for details. While the RRDE method is commonly employed to assess the inherent performance of M–N–C SAECs, RRDE results typically represent catalysts' maximum potential and differ significantly from the conditions witnessed in actual devices. In practice, sample preparation has a substantial influence on the catalytic activity of a RRDE, and the O_2 mass transfer rate is limited, so the electrolytes need to be pre-saturated with O_2 .

$$\text{H}_2\text{O}_2 \text{ selectivity (\%)} = 200 \times \frac{I_{\text{R/N}}}{I_{\text{D}} + I_{\text{R/N}}} \quad (23)$$

where I_{R} represents the current of the ring, I_{D} denotes the current of the disk, and N signifies the collection efficiency in the RRDE. N refers to the efficiency at which the platinum ring collects, as defined by measuring the redox reaction of hexacyanoferrate ($[\text{Fe}(\text{CN})_6]_3^- / [\text{Fe}(\text{CN})_6]_4^-$) $[\text{Fe}(\text{CN})_6]_4^-$.

6.1.2. H-type electrochemical cell

The counter electrode, which receives a specific oxidation potential, requires isolation from the working electrode to prevent the immediate oxidation of the generated H_2O_2 . A H-type cell, as illustrated in **Fig. 21b**, which uses an ion exchange membrane (IEM) to divide the working and counter electrode compartments from each other, is appropriate for this application. It is commonly utilized in laboratory settings and consists of an anode chamber and a cathode chamber, divided by an IEM such as Nafion. This membrane facilitates the transfer of H^+ ions while effectively obstructing the migration of H_2O_2 to the anode side. In 2003, Yamanaka and colleagues [235] initiated groundbreaking research that integrated the electrochemical production of H_2O_2 with H-type IEM fuel cells. In this setup, the protons were generated through the release of O_2 from water within the anode chamber, removing the necessity for H_2 and thereby diminishing the additional transport expenses and safety issues associated with H_2

handling. In 2018, Yamanaka et al. [113] discovered that using Co–N_x–C SAECs as the cathode catalyst in this setup resulted in the H₂O₂ concentration reaching up to 18.7 wt%. The design of the H-type cell effectively prevented the oxidation of newly formed H₂O₂ [236]. In traditional H-type cells, enhancing the electron transfer efficiency is achievable by elevating the current density. However, at a certain threshold, the 2e[−] ORR activity becomes constrained by the mass transfer efficiency of the O₂ in electrolytes. This limitation arises from the relatively low solubility of O₂ in water at room temperature (only 8 mg/L). Beyond this point, the insufficient supply of O₂ due to its limited solubility leads to a reduction in the kinetics of the 2e[−] ORR, illustrating the critical balance between enhancing current density and ensuring the adequate mass transfer of reactants in electrochemical systems [237,238].

To increase the mass transfer of O₂, gas diffusion electrodes (GDEs) have been widely utilized. As shown in **Fig. 21c**, the gas diffusion layer (GDL), commonly composed of a hydrophobic layer combined with a carbon base, serves as the substrate for the cathodic CL to form GDEs and boost O₂ diffusion. This configuration efficiently concentrates O₂ near the electrode surface, facilitating rapid mass transfer and increasing the reaction rate, thus enhancing the current density and production efficiency of H₂O₂ [239]. This strategy effectively addresses the challenge of limited O₂ solubility in water, contributing to more efficient electrochemical processes. GDEs have also been used in H-type cells for the electrosynthesis of H₂O₂. Wu and co-workers [176] prepared an (O, N)-coordinated Fe SAEC as a cathode for H₂O₂ generation, achieving an impressive yield of 300 mM at a current density of 60 mA cm^{−2} for 50 h. This performance significantly outstrips that of traditional electrodes, with the yield from the GDE nearly tripling that of conventional setups, thereby underscoring the GDE's superior design in H-type cell configurations. Despite the GDE's enhanced efficiency in H-type cells, which facilitates a breakthrough in overcoming application barriers, challenges remain, especially concerning the accumulation of H₂O₂ near the cathode area. This concentration peak near the working electrode, induced by the continuous oxygen gas flow stirring the electrolytes in standard cells, not only disrupts the cell's dynamic conditions but also contributes to the conversion of H₂O₂ back into H₂O [76,84,240]. Such dynamics suggest limitations in the H-type cell's viability for long-duration, high-current-density operation.

6.1.3. Electrochemical flow cell

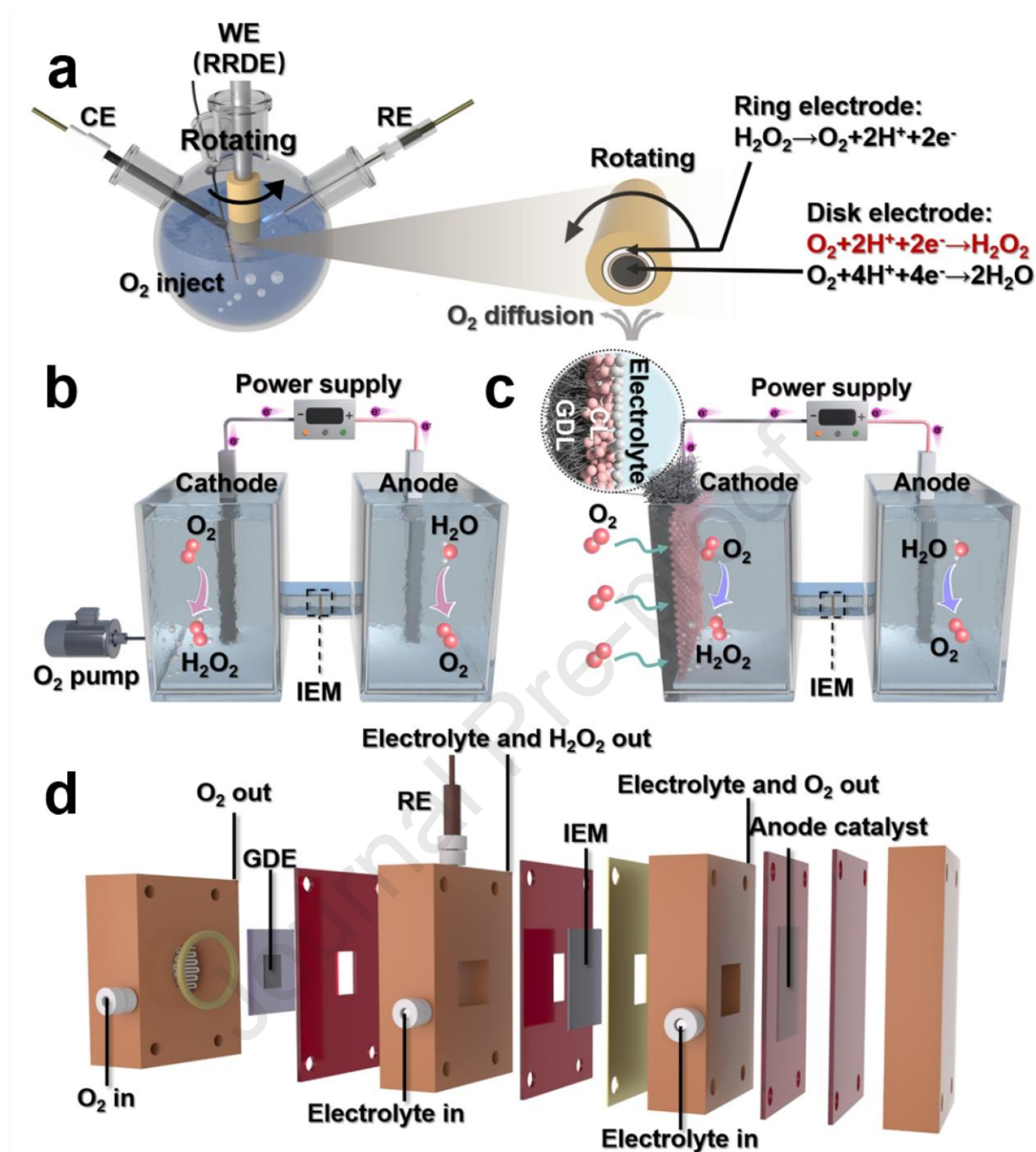


Fig. 21. Schematics of (a) a RRDE setup in a three-electrode electrochemical cell; (b) a H-type ion exchange membrane electrochemical cell, (c) an H-type ion exchange membrane electrochemical cell equipped with a GDE, and (d) an electrochemical flow cell.

Flow cells with GDEs function by persistently directing O_2 to the cathode for H_2O_2 formation and simultaneously expelling byproducts via a steadily circulating aqueous electrolyte, which can effectively address the above issue. Continuous flow cells, as illustrated in **Fig. 21d**, which consistently move reactants and products to and from GDEs, present optimal setups for surpassing the gas diffusion and H_2O_2 accumulation challenges inherent in traditional reactors [241]. Furthermore, a single unit can be effortlessly constructed in the lab, whereas

larger assemblies can be created by layering several units together, significantly reducing the time needed to move from research to real-world applications [242]. When Co–N–C SAECs were integrated into a flow cell with a membrane and GDEs, they achieved maximum H₂O₂ yields (11.53 mol g_{cat.}⁻¹ h⁻¹ under a current density of 300 mA cm⁻² and with a FE of 96–100% in 1 M KOH) [155].

Based on the conventional flow cell, a unique membrane-based cell was developed. This cell incorporated a cation exchange membrane (CEM), a porous solid electrolyte (SE) (for instance, microspheres of styrene-divinylbenzene copolymer functionalized with sulfonic acid groups), and an anion exchange membrane (AEM). It was demonstrated to successfully facilitate the direct electrocatalytic generation of pure H₂O₂ solutions without aqueous electrolytes [243]. In this process, anodic reactants such as pure H₂ and cathodic ingredients like pure O₂ were introduced into the respective electrocatalysts via the stream channels within the anode and cathode, as illustrated in **Fig. 22a**. Additionally, a centrally positioned porous SE facilitated the combination of ions formed within both the anode (e.g., H⁺) and the cathode (e.g., HO₂⁻) compartments, resulting in the formation of clean H₂O₂. Ultimately, the produced H₂O₂ was dissolved and carried away from the cell by deionized water flowing in the intermediate layer. Researchers also demonstrated that the pure O₂ and H₂ fed through the cathode and anode could be replaced by air and water, respectively, to further simplify the devices. When M–N–C SAECs were used in this reactor, the H₂O₂ production was dramatically improved. Liu et al. [171] created a range of β -substituted Co–N–C SAECs for H₂O₂ production, reaching a maximum H₂O₂ productivity of 10.76 mol g_{cat.}⁻¹ h⁻¹ under a current density of 288 mA cm⁻² and a FE of over 90%. This system maintained a current density of 50 mA cm⁻² for 48 hours in a SE flow cell. Recently, Lee et al. [51] employed a 1.2 mm gap in the SE and noted a pure H₂O₂ productivity of 26.1 mol h⁻¹ g_{cat.}⁻¹ using CoPc-CNT(O) SAECs.

However, such a system suffers from AEM stability problems, and the ohmic losses increase due to the presence of two membranes and a solid porous layer. To address existing drawbacks, researchers proposed a new strategy involving immediate exposure to the cathode electrode with a solid proton-conducting porous layer, which in turn was in contact with the CEM [244,245]. The structure allows protons generated at the anode to reach the cathode easily, effectively obviating the necessity for an AEM, as shown in **Fig. 22a**, which simplifies and stabilizes the system. Li et al. [244] introduced an improved SE single membrane system that overcame the obstacles posed by AEM integration. This system demonstrated robust 2e⁻ ORR performance, achieving a current density of 389 mA cm⁻² (approximately 6.53 mmol cm⁻² h⁻¹)

with 90% FE for H₂O₂ production, and it maintained its integrity during a 50-hour durability assessment. In conclusion, one significant benefit of the SE system lies in its elimination of the need for further separation and purification of the generated H₂O₂, making it highly promising for scaled-up production.

6.1.4. Other unique reactor configurations

In addition to the foregoing most prevalent device designs, researchers have engineered a range of innovative reactor configurations that exhibit exceptional performance for the 2e⁻ ORR. These advances significantly enhance the prospects for the industrial-scale electrosynthesis of H₂O₂ [166,246,247]. Departing from traditional SE cell configurations, Zhang et al. [246] introduced a novel SE reactor that incorporates two proton exchange membranes (PEMs), creating a tri-chamber structure to optimize the cation shielding effect for enhanced H₂O₂ production. As shown in **Fig. 22b**, this device features a cathode and an anode separated by a thin SE layer, flanked by two identical PEMs. The cathode compartment receives a continuous flow of mixed O₂ and H₂O streams for the 2e⁻ ORR, while the anode compartment circulates water for the OER. A dilute cation solution traverses this SE layer, introducing cations that enhance the 2e⁻ ORR at the cathode. This design falls under the category of cation-modulated interface engineering, aimed at enhancing the catalytic efficiency for converting O₂ into H₂O₂ at rates pertinent to industrial applications in highly acidic environments. Introducing trace amounts of alkali metal cations into acidic solutions markedly enhances the selectivity and stability of H₂O₂ production, particularly at ORR current densities exceeding 400 mA cm⁻².

The membrane electrode assembly (MEA) is a critical component used predominantly in electrochemical devices such as fuel cells and electrolyzers. A standard MEA consists of a cathode, electrolyte membrane, and anode, which are hot-pressed to ensure intimate contact among the components. Motivated by advances in MEA technology, research in the 1990s initiated efforts to synthesize H₂O₂ using a PEM setup [248]. As illustrated in **Fig. 22c**, the conventional PEM configuration comprises two GDEs (an anode and a cathode), a PEM that divides the electrodes, and channels for delivering the reactant to each electrode. MEA reactors provide three principal benefits: an advanced assembly process developed from extensive use in electrolyzed water systems and fuel cell technologies; improved 2e⁻ ORR efficiency facilitated by the consistent delivery of reactants and extraction of products through well-designed flow arrangements; and the generation of H₂O₂ devoid of salt contaminants, owing to their operation without a liquid electrolyte, rendering them highly suitable for industrial

applications [249,250]. In a study conducted by Chen et al. [166], the MEA was constructed using the catalyst-coated membrane technique. The MEA electrolyzer, coupled with an optimized Co–N–C SAEC, consistently and reliably generated a high-concentration, approximately 7 wt% pure H₂O₂ aqueous solution at 400 mA cm⁻² for over 200 hours, maintaining a cell voltage of about 2.1 V. However, traditional MEA electrolyzers continue to encounter obstacles such as intermittent H₂O₂ production and issues with product stability because of changes in the pH environment. Furthermore, prevalent challenges with ion exchange membranes, including inadequate mechanical durability, membrane deterioration, and high costs, coupled with the necessity for enhanced gas diffusion and utilization efficiency in GDEs, are vital areas for advancing the development of MEA electrolyzers for applications beyond H₂O₂ electrosynthesis.

In traditional reaction cells, H₂O₂ is typically produced solely through the 2e⁻ ORR at the cathode, where the anode's energy is not completely harnessed, leading to energy wastage. To address these limitations, researchers have designed a reaction apparatus that enables the simultaneous production of H₂O₂ at both cathode and anode [247,251]. As illustrated in **Fig. 22d**, the cathode and anode of the reactor are equipped with identical catalysts coated on a GDL. O₂ is introduced at the cathode side, initiating a 2e⁻ ORR that produces H₂O₂, which is then transported by the continuously flowing electrolyte. Simultaneously, the electrolyte circulating on the anode side facilitates the 2e⁻ WOR on the catalyst, also generating H₂O₂ that accumulates progressively. Throughout this process, the cathode and anode efficiently produce the desired product, achieving a combined FE of up to 200% for the reaction and ensuring optimal energy utilization. In a recent study, an integrated 2e⁻ ORR/2e⁻ WOR electrolysis system utilizing a unique oxygen-defect bismuth catalyst exhibited superior performance in the co-electrosynthesis of H₂O₂, achieving an impressive cell FE of 154.8% and an exceptionally high H₂O₂ production rate of 4.3 mmol cm⁻² h⁻¹ [247]. While paired-electrosynthesis systems effectively harness electrical energy to synthesize the desired product, the 2e⁻ WOR at the anode competes with the 4e⁻ WOR process, which produces O₂, reducing H₂O₂ yields. Consequently, there is a critical need to develop innovative M–N–C SAECs characterized by enhanced 2e⁻ ORR/2e⁻ WOR selectivity. Achieving this research objective could significantly expedite the industrial production of electrically generated H₂O₂.

To summarize, the merits and challenges of the above-mentioned reactors are compared in **Table 6**. The RRDE method, effective for lab-scale H₂O₂ quantification from the 2e⁻ ORR, faces O₂ mass transfer and sample preparation challenges, limiting its real-world application.

The H-type cell, with IEM-separated chambers, prevents H_2O_2 decomposition at the anode. GDE integration solves O_2 mass transfer. However, H_2O_2 accumulation at the cathode leads to reduction, affecting the FE under high currents. The electrochemical flow cell with GDEs overcomes these limitations, offering superior rates, transport, and scalability for H_2O_2 electrosynthesis, but the output H_2O_2 contains electrolyte impurities. An SE-enhanced flow cell further simplifies separation and purification, promising large-scale use after the AEM and SE stability issues are overcome. Innovative designs, like dual PEM SE reactors and traditional MEA electrolyzers, broaden industrialization prospects. Nevertheless, gas–liquid homologation is often challenged by low H_2O_2 concentrations. The paired-electrosynthesis system maximizes electrical energy utilization, achieving a 200% FE limit, yet the challenge of selecting appropriate electrolytes and electrocatalysts remains. Overall, the SE-based flow cell demonstrates significant potential for industrial implementation, primarily stemming from its enhanced product purity compared to conventional configurations. While AEM durability remains a critical challenge in this configuration, SE selection emerges as the critical factor governing reactor performance and operational longevity. Paired-electrosynthesis systems capable of harnessing both cathodic and anodic energy streams concurrently represent another viable pathway for scaled production, though investigations into their catalytic components and electrolyte optimization remain limited and require further exploration.

Table 6. The merits and challenges of various reaction generators for H_2O_2 electrosynthesis.

Reactors	Merits	Challenges
RRDE	Direct approach for quantifying H_2O_2 production	Can only be used at laboratory scale
H-type cell	Prevents H_2O_2 from migrating to the anode side	H_2O_2 will decompose after excessive accumulation at the cathode
Flow cell	Brings out H_2O_2 product in time to prevent decomposition	The product contains electrolyte impurities
SE-based flow cell	Produces pure H_2O_2	Unstable reaction system caused by AEM and SE
MEA	Simple reaction configuration and pure product	Low concentration of H_2O_2 product
Paired system	Simultaneous utilization of cathode and anode to achieve 200% FE	Difficult to design and select electrocatalysts and electrolytes

6.2. Practical applications and integrated systems

While H₂O₂ electrosynthesis offers opportunities for on-site utilization, its applicability is limited by concentration constraints and electrolyte effects. Besides, in a typical 2e⁻ ORR-based H₂O₂ electrosynthesis system, the anode undergoes the OER, the substantial overpotential of which demands considerable energy to overcome. Consequently, there is a need for integrated electrochemical systems that can concurrently produce valuable products at both electrodes. This section explores the potential applications and underlying principles of electrochemical H₂O₂ production. We also discuss the development of integrated systems combining H₂O₂ generation with other applications.

6.2.1. Electro-Fenton reactor

The onsite production of H₂O₂ in electrochemical systems facilitates the degradation of organic pollutants and disinfection, primarily through the electro-Fenton process, which involves adding Fe²⁺ to the electrolyte. Alternatively, as shown in **Fig. 22e**, the anode can be substituted with an Fe electrode. This setup offers a promising avenue for rapid water purification by leveraging an *in situ* iron source. The Fe electrode loses electrons to generate Fe²⁺ during the electrochemical process (**Equation (24)**), which then reacts with the H₂O₂ produced at the cathode to generate •OH radicals, as shown in **Equation (25)**. The generated reactive •OH species effectively break down organic contaminants within the electrolyte into the smaller molecules H₂O and CO₂, as illustrated in **Equation (26)**. There have been numerous studies on the use of electrogenerated H₂O₂ for decomposing various organic contaminants in wastewater [186,252–254]. In a recent study, a free standing Co–N–C SAEC was successfully prepared [252]. A high-performance Co SAC supported on well-aligned carbon nanofibers was utilized in an electro-Fenton process and exhibited an impressive rate constant of $4.89 \times 10^{-4} \text{ s}^{-1}$ for the removal of methylene blue, attributed to its outstanding 2e⁻ ORR activity. Jing et al. [255] developed cobalt-embedded oxygen-enriched mesoporous carbon nanosheets (MesoC–Co), which demonstrated exceptional H₂O₂ generation performance under acidic conditions. The system employed RhB and methyl orange as representative contaminants for electro-Fenton treatment evaluation. Experiments were conducted in an oxygen-saturated acidic environment containing 25 mg L⁻¹ organic contaminants and 0.8 mM Fe²⁺ ions, utilizing a three-electrode H-cell configuration with MesoC–Co serving as the cathode and maintained at 0.45 V vs. RHE. Notably, the optimized electro-Fenton system achieved the complete decomposition of both contaminants within 80 minutes of operation. The electro-Fenton

process can be enhanced with UV or solar light, boosting the degradation efficiency by increasing the regeneration rate of Fe^{2+} [256]. However, the requirement for Fe^{2+} ions restricts the electrolyte pH to a range of 2.8 to 3.5 [257]. To broaden the pH range, other transition metal ions, such as Cu, Ce, Cr, Co, and Mn, have been explored as alternatives. Additionally, ultraviolet radiation and ozone can generate $\cdot\text{OH}$ radicals for degradation without imposing electrolyte restrictions or affecting the electrochemical system, making them ideal for *in situ* degradation within reactors [258].



Electrochemically generated H_2O_2 can function as an effective disinfectant and antibacterial agent. Its onsite producibility, along with its environmentally friendly nature, make it an advantageous method for sterilizing surfaces, water, and medical instruments. Wang et al. [186] examined the disinfection efficacy of electrochemically generated H_2O_2 . *Escherichia coli* was introduced into the solution, and the disinfection process was assessed by tracking the bacterial concentration. The results indicated that 43% of the bacteria were inactivated within 5 minutes, and almost 100% were eliminated after 120 minutes, with no bacterial regrowth observed.

6.2.2. Metal- H_2O_2 batteries

H_2O_2 is an optimal energy carrier and green fuel, boasting the highest energy density in comparison with other popular clean fuels like hydrogen and ammonia [73]. Its liquid state facilitates easy handling and transport. As a carbon-free energy source, it operates without CO_2 emissions. These appealing advantages suggest its significant potential for use in energy conversion technologies, pointing to an increase in global demand for this valuable chemical.

Zinc-air batteries are exemplary sustainable systems due to their affordability, safety, and high energy density [259]. However, the 4e^- ORR suffers from sluggish kinetics and necessitates complex, costly catalysts to enhance the process [260,261]. Sun et al. [262] reported a rechargeable Zn-air battery utilizing Zn peroxide chemistry. As shown in **Fig. 22f**, the cathode reaction involves the 2e^- ORR and still requires an oxygen supply. Although the theoretical voltage of the 2e^- ORR is lower compared to H_2O_2 reduction and the 4e^- ORR, the zinc peroxide chemistry offers improved reversibility and cycling performance. The authors

also emphasized the importance of designing multifunctional electrocatalysts to enhance battery efficiency. M–N–C SAECs with exceptional $2e^-$ ORR activity and selectivity are considered ideal candidates. Recently, Li et al. [263] presented 2D mesoporous M–N–C SAECs featuring symmetry-breaking FeN_2S_2 catalytic sites (shown in **Table 1**) integrated with a matrix that enhances mass and electron transfer (referred to as meso-FeNSC) for rechargeable $2e^-$ neutral zinc–air batteries. The accessible FeN_2S_2 sites optimize the dynamic electronic and geometric structures, thereby enhancing the crucial $2e^-$ ORR. Consequently, the $2e^-$ neutral zinc–air batteries exhibit a significantly improved discharge potential of approximately 1.2 V and a lifespan of 400 hours at 0.2 mA cm^{-2} .

6.2.3. Coupled systems

Conventional electrolytic cells for H_2O_2 electrosynthesis typically harness only the cathodic $2e^-$ ORR, leading to energy waste at the anode. Thus, maximizing the anodic reaction alongside the cathodic $2e^-$ ORR is crucial for industrial applications. Seawater, the most abundant resource on Earth, has recently been the subject of extensive research in energy-related fields. Using seawater as an electrolyte is a promising strategy for reducing costs and enhancing on-site H_2O_2 production along coastlines. However, its application in electrocatalytic energy conversion systems is still in the preliminary phase. A significant challenge is the competition between chloride ions and oxygen for catalyst active sites, hindering the $2e^-$ ORR process. Shao and colleagues [164] improved a Co–N–C SAEC with high chloride tolerance. Their electrosynthesis system performs effectively in simulated seawater, achieving a high FE of 95.6% and an H_2O_2 production rate of $4.5\text{ mol g}^{-1}\text{ h}^{-1}$. Additionally, as shown in **Fig. 22g**, the coupled anodic reaction produces Cl_2 gas, providing extra economic benefits for the electrolyzer. In a membrane-free reaction system, the anode can participate in ozonation, as shown in **Equation (27)**, or chlorination, as expressed in **Equations (28) and (29)**, coupling with the H_2O_2 generated at the cathode to produce various reactive oxygen species like $\cdot OH$, as shown in **Equation (30)**, and singlet oxygen (1O_2), as illustrated in **Equation (31)**, which are effective for degrading pollutants or eliminating microorganisms [27,264–266]. These approaches are greener and more efficient than traditional electro-Fenton processes, as they require no metal input for H_2O_2 activation.





In summary, the emerging technology of H_2O_2 electrosynthesis holds significant potential for various industrial applications; for instance, integrated electro-Fenton reactors can effectively remove pollutants and pathogens from water. Additionally, it serves as an energy carrier for the cathode in metal- H_2O_2 cells. Maximizing anode energy utilization during the cathodic 2e^- ORR is also promising for industrial implementation. By selecting appropriate electrocatalysts, electrosynthesis can produce Cl_2 (using seawater as the electrolyte) or ozone at the anode and H_2O_2 at the cathode. Coupling cathodic H_2O_2 with anodic products offers a promising strategy to enhance energy efficiency.

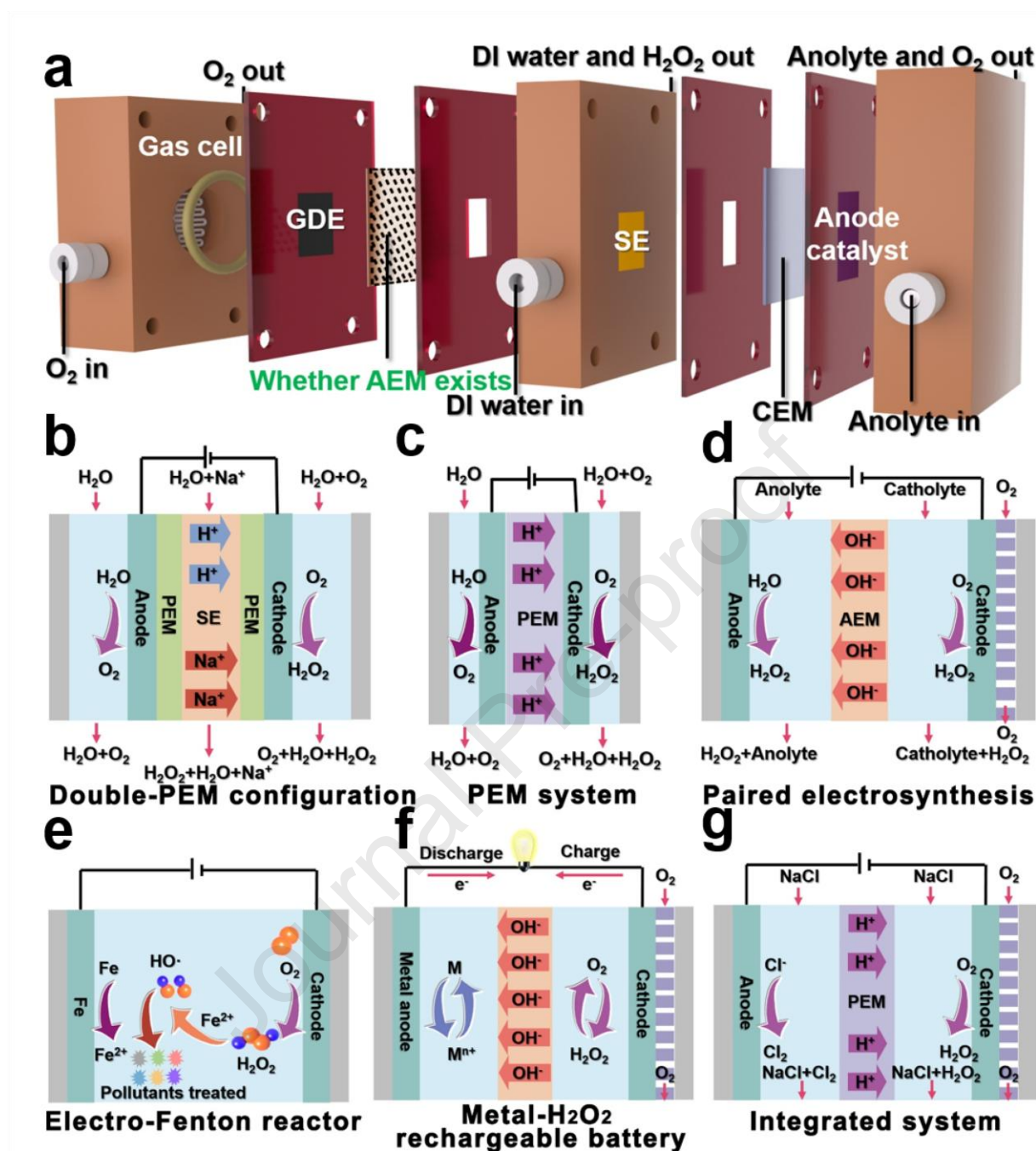


Fig. 22. Schematic illustration of the typical electrochemical devices for H_2O_2 production. (a) SE cell configuration (single PEM or AEM-PEM system). (b) SE cell with double PEM configuration. (c) PEM electrolyzer. (d) An AEM-separated two-chamber flow cell for paired electrosynthesis of H_2O_2 . (e) Electro-Fenton system for onsite pollutant degradation. (f) Rechargeable metal- H_2O_2 battery. (g) A flow cell to produce H_2O_2 and Cl_2 .

7. Conclusions

This review has presented a thorough overview of reaction mechanisms, reactivity descriptors, synthetic methods, characterization techniques, structure–performance correlations, optimization strategies, and reactor regulation for M–N–C SAECs for H_2O_2 production via the

$2e^-$ ORR. Their desirable cost and high selectivity for the $2e^-$ ORR make M–N–C SAECs preferable electrocatalysts over their noble-metal counterparts. The ideal $2e^-$ ORR reactivity of M–N–C SAECs is attributed not only to their 100% atom utilization efficiency but also to their special microstructures, which facilitate the Pauling-type O_2 adsorption configuration. The synthesis approaches significantly affect the microstructures and properties of M–N–C SAECs; in addition, the coordination configurations of the central metal sites within M–N–C SAECs and interfacial changes during the reaction can be determined through advanced characterization methods. Among the various M–N–C SAECs, Co–N–C SAECs have presented the most promising catalytic activity ($49 \text{ mol h}^{-1} \text{ g}_{\text{cat}}^{-1}$), the highest H_2O_2 selectivity (close to 100%), and the lowest H_2O_2 RR activity. In addition, tuning the ligand surroundings of the center metal sites, varying the coordination numbers, and doping with external heteroatoms or OFGs can further refine the catalytic performance of M–N–C SAECs. Recently, to achieve the industrial synthesis of H_2O_2 by electrochemical methods, substantial effort has been focused on the engineering and assembly of devices.

8. Future perspectives

Despite these significant advancements in M–N–C SAECs for the production of H_2O_2 from the $2e^-$ ORR and practical reactors, several challenges and areas for deeper exploration remain, as illustrated in **Fig. 23**.

8.1. Design and synthesis of M–N–C SAECs

While the bottom-up synthetic approach enables the precise modulation of M–N–C SAECs' structure by meticulously regulating reaction parameters, the stringent conditions present challenges for large-scale synthesis. Future endeavors should prioritize the precision of top-down synthesis methods for M–N–C SAECs, such as mechanical ball milling, to advance the industrial feasibility of this strategy. Co–N–C SAECs exhibit unparalleled catalytic activity but are often constrained by metal toxicity. Exploring alternative M–N–C SAECs that feature diverse metal activity centers, along with refining modification techniques, are promising avenues to mitigate toxicity concerns while maintaining or enhancing catalytic efficiency.

Optimizing metal atom loading is key for enhancing catalytic efficiency and H_2O_2 selectivity, necessitating novel synthesis methods and tight microstructure control. Maintaining the stability of metallic species within carbonaceous lattice structures is a critical determinant for achieving superior H_2O_2 concentration in M–N–C SAECs systems. Excessive leaching of

metal ions into the electrolytic medium inevitably induces H_2O_2 reduction reactions, thereby attenuating the accumulated H_2O_2 concentration. Consequently, meticulous regulation of both acid concentration and etching duration is essential. Higher concentrations or prolonged exposure lead to compromised active site density, while overly dilute acids or insufficient reaction periods induce accelerated dissolution, ultimately compromising catalyst performance and H_2O_2 yield. The role of higher coordination shells in M–N–C SAECs remains relatively unexplored, presenting an opportunity to significantly enhance catalytic activity through atomically precise manipulation of these coordination layers. Furthermore, beyond OFGs, the incorporation of fluorine-bearing functional moieties onto carbon-based substrates has proven effective in enhancing the hydrophobicity of GDE surfaces, thereby conferring resistance against flooding. Mastering the atomic-level control of these functional groups, supported by real-time atomic-scale characterization techniques like *in situ* XAFS and AC-HAADF/STEM, could optimize the catalyst–electrolyte interface, thereby boosting the efficiency of M–N–C SAECs in the 2e^- ORR for H_2O_2 generation.

8.2. Exploration of reaction mechanisms

Understanding the mechanisms governing the 2e^- ORR in M–N–C SAECs is crucial for advancing electrocatalysis. During the 2e^- ORR, the M–N–C SAECs on the electrode may undergo configuration transformations, such as migration and agglomeration, which influence the reaction dynamics. Advanced operando-characterized technologies such as *in situ* XAFS spectroscopy and *in situ* electron microscopy techniques, as well as combinations of multiple techniques, enable real-time examination of electron distribution and reaction pathways during the 2e^- ORR, which will unveil more comprehensive insights into the underlying reaction principles. Current studies predominantly focus on improving M–N–C SAEC activity and selectivity, yet the alternation of M–N–C SAEC configurations during long-term operation remains underexplored. Catalyst deactivation due to surface oxidation, active-site blockage, or dissolution (e.g., in acidic media) severely limits operational lifetimes. Thus, employing *in situ/operando* characterization to unravel degradation pathways under realistic electrochemical conditions is essential for understanding the deactivation mechanism of M–N–C SAECs, especially at industrial current densities. By comprehensively elucidating the deactivation mechanism, it becomes feasible to devise a tailored M–N–C SAEC protection strategy or, alternatively, to directly enhance the lifespan of M–N–C SAECs through straightforward regeneration methods.

Existing *in situ* methods face challenges when it comes to resolving transient intermediates that are critical for understanding the dynamic behavior of M–N–C SAECs during operation. To address this, the development and application of operando characterization strategies, such as time-resolved XAFS, transient IR/Raman spectroscopy, and electrochemical mass spectrometry, are essential for tracking short-lived intermediates and elucidating reaction pathways in real time. These techniques transcend the static limitations of conventional AC-HAADF/STEM (spatial resolution only), XPS (surface-restricted snapshots), and even routine XAFS (ensemble averaging). Looking ahead, advancing integrated, multimodal platforms that simultaneously capture atomic-scale imaging, electronic structure evolution, and surface chemistry monitoring will be critical for establishing definitive structure–activity relationships under realistic conditions.

While conventional characterization techniques provide critical atomic-scale structural and electronic insights, they remain fundamentally limited for probing dynamic micro-environmental factors, such as local pH gradients, ionic concentrations, and electric fields, which dictate catalytic behavior under operational conditions. Bridging this gap requires the adoption of interdisciplinary correlative approaches. For instance, *in situ* Raman spectroscopy with molecular pH probes can track proton activity near active sites; scanning electrochemical microscopy (SECM) enables the nanoscale mapping of interfacial reactivity; and electrochemical impedance spectroscopy (EIS), coupled with computational modeling, deciphers charge transport phenomena. Though still emerging, these techniques represent a promising frontier in M–N–C SAEC characterization, where understanding the solid–liquid interface is as vital as resolving atomic structures. Future progress should prioritize the integration of these advanced tools with existing methods to construct a holistic picture of catalyst microenvironments.

8.3. Modification of electrolytes and catalytic interface

The selection of electrolytes has a direct impact on the selectivity of electrosynthesized H_2O_2 . Although alkaline electrolytes have been widely investigated for the 2e^- ORR process catalyzed by M–N–C SAECs, the inherent susceptibility of H_2O_2 to hydrolytic degradation under alkaline conditions restricts the achievable H_2O_2 concentrations. This challenge often requires the use of stabilizing agents, which unfortunately increase both production costs and system complexity, thereby reducing the feasibility of such approaches for large-scale industrial applications. There is a pressing need to advance research into M–N–C SAECs suitable for

acidic or neutral conditions, including the development of catalysts that can directly utilize seawater as the electrolyte. Addressing the consumption of protons during the $2e^-$ ORR is also essential, as this influences the pH at the reaction interface and thereby affects the reaction efficiency. Furthermore, under high current densities, the exhaustion of cathodic protons induces a localized alkaline environment, which accelerates the hydrolytic instability of H_2O_2 and thereby hinders its accumulation. Future research could benefit from kinetic simulations to explore proton transfer processes and their role in $2e^-$ ORR dynamics.

Ion-conducting polymer electrolytes, including SEs, offer innovative alternatives, enabling the direct production of H_2O_2 solutions and avoiding subsequent purification processes. These novel electrolytes must balance several key attributes such as high conductivity, affordability, and robust resistance to cross-contamination between reactants and products. Challenges exist, such as AEM stability in a highly concentrated H_2O_2 solution and increased ohmic losses, but recent advancements like integrating a SE layer directly with the cathode have streamlined systems and improved their efficiency. As attention turns toward alternatives to AEMs, mitigating electrode flooding risks in M–N–C SAEC setups will be critical. The compression of cathode GDEs induced by SE expansion underscores the need for GDLs with enhanced mechanical robustness. Materials such as titanium felts and stainless steel mesh-reinforced carbon-based GDLs demonstrate superior structural integrity, thereby effectively mitigating electrode flooding risks.

8.4. Improvement of reaction generators

Achieving efficient H_2O_2 production requires precise reactor design in addition to the right catalysts. Having an in-depth understanding of and innovative approaches to electrode and electrolyzer design is essential for achieving efficient industrial-scale H_2O_2 synthesis. One key area for improvement is the optimization of electrode substrates, particularly for GDEs, to boost reactor durability and H_2O_2 production. Electrode flooding remains a critical challenge for GDEs, as it reduces the triple-phase boundary and consequently lowers the production of H_2O_2 . Key to addressing this challenge are binders, crucial components that regulate charge transfer dynamics and mechanical stability in modern batteries. For instance, integrating hydrophobic interfacial binders like fluorinated polymers (e.g., PTFE and PVDF) in cathodes optimized for the $2e^-$ ORR could substantially improve electrode integrity against flooding.

Laboratory-scale experiments commonly employ RRDE or H-type cells, which are limited by low current densities and inadequate mass transfer. Transitioning to GDEs effectively

circumvents O_2 mass transfer constraints in H-type cells. However, in such batch systems, the cathodic accumulation of H_2O_2 can induce self-decomposition, thereby preventing product concentration build-up. In contrast, continuous-flow cell architectures or MEA configurations enable real-time product evacuation and sustain industrial-level current densities and FEs. For instance, modulating the flow rate of the deionized water feed enables precise control over H_2O_2 concentrations, thereby accommodating the diverse operational demands of downstream applications. Consequently, advancing the durability of flow cell platforms (particularly SE variants) and optimizing catalytic electrolyte interfaces within MEA-based stacks are pivotal strategies for bridging the gap between laboratory-scale H_2O_2 electrosynthesis and industrial implementation.

Current H_2O_2 electrosynthesis systems predominantly rely on carbon-intensive electricity sources, inadvertently contributing to greenhouse gas emissions. Future reactor designs should prioritize the integration of renewable energy sources (solar, wind, tidal, and others) to support sustainable electricity generation while enabling eco-friendly H_2O_2 production. Furthermore, the development of dual-functional energy systems integrating 2e^- ORR architectures is an emerging direction in electrochemical engineering. Such integrated configurations, like fuel cell/metal–air battery, enable simultaneous high-purity H_2O_2 synthesis and direct power generation through the 2e^- ORR pathway, facilitating carbon-neutral energy conversion while meeting industrial demands.

8.5. Integrating simulation strategies in H_2O_2 electrosynthesis

The integration of artificial intelligence (AI) into the development of SAECs for H_2O_2 electrosynthesis is rapidly transforming the field, offering new opportunities for optimizing catalyst design, reaction mechanisms, and reactor efficiency. AI's capacity to process vast amounts of experimental data enables the identification of key parameters that influence catalyst performance, accelerating the discovery of high-performance materials for the 2e^- ORR. In particular, machine learning (ML) algorithms can predict the energy barriers of rate-determining steps and reaction pathways in the 2e^- ORR, facilitating the precise engineering of M–N–C SAECs and transforming empirical methods into data-driven processes. This capability enables more efficient catalyst screening and reactor design optimization. For instance, Yu et al. [267] leveraged advanced ML frameworks to forecast the performance metrics of nascent electrocatalyst candidates while expanding the conventional chemical design landscape. Their work underscores the transformative potential of integrating motif-guided catalyst engineering

with ML methodologies, enabling efficient navigation through uncharted regions of the chemical space and accelerating the identification of promising $2e^-$ ORR electrocatalysts. In the context of developing ORR DACs, Liu et al. [268] established a 2D ML descriptor framework incorporating interatomic geometric distance and intrinsic electronic magnetic moments as axes. The emergence of a constrained high-performance region within this descriptor space underscores the importance of synergistic geometric–electronic coupling in rational electrocatalyst design. Following computational predictions, a N-coordinated cobalt–manganese diatomic complex (Co-N-Mn/NC) was successfully synthesized and experimentally validated, exhibiting exceptional ORR electrocatalytic performance. Moreover, computational chemistry tools like COSMOL can simulate the interactions between catalyst surfaces and electrolytes, providing real-time predictions of how changes in reactor parameters—such as temperature, pressure, and electrolyte composition—affect the reaction process.

Despite the decentralized nature of H_2O_2 electrosynthesis using O_2 , water, and electricity, a comprehensive environmental assessment is lacking. AI helps to evaluate the environmental footprint of such systems using methodologies like life cycle assessment, refining assessment frameworks, and enhancing sustainability metrics. By integrating AI-driven approaches, researchers can better understand and mitigate environmental impacts, ensuring the sustainable development of electrochemical H_2O_2 synthesis technologies.

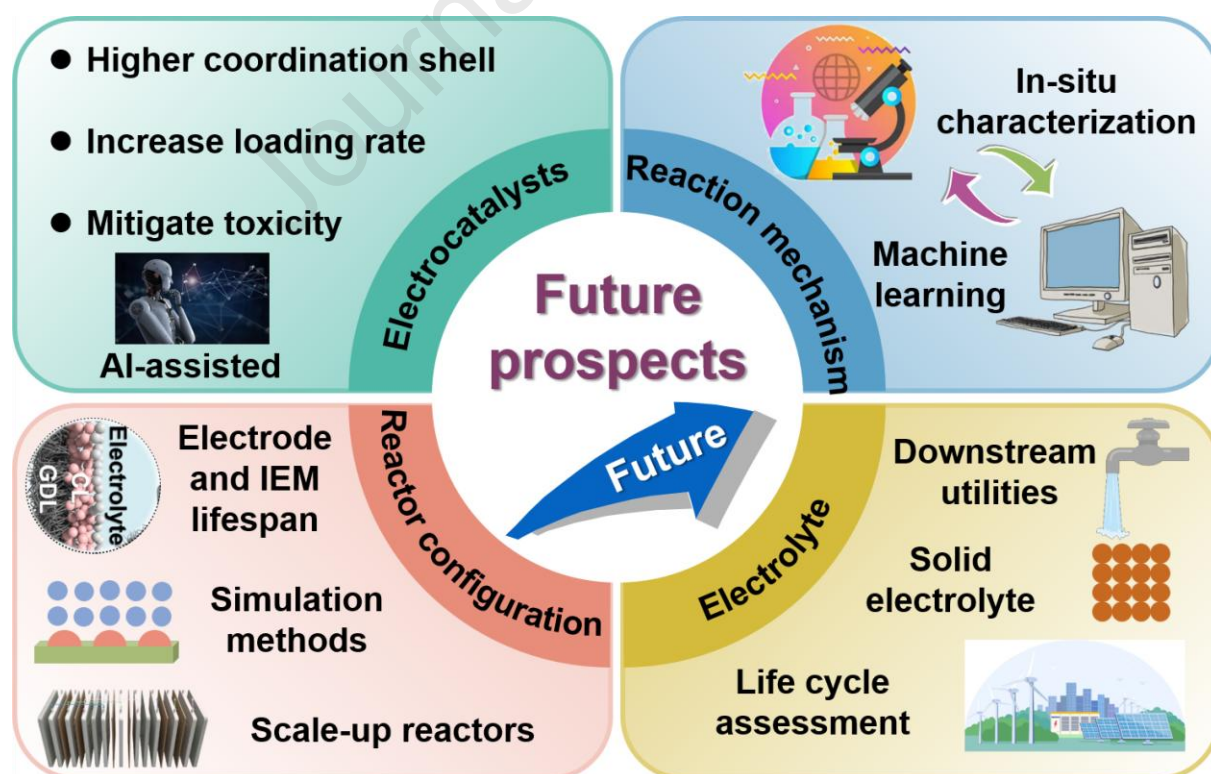


Fig. 23. Future prospects of the $2e^-$ ORR to produce H_2O_2 with M–N–C SEACs.

Acknowledgments

The authors gratefully acknowledge the financial support provided by the National key research and development program of China-Key technologies and system for intelligent control of water supply network (2022YFC3203800), the Science and Technology Plan Project of Beijing City (Z231100006623001), the National Natural Science Foundation of China (52270083), the Fundamental Research Funds for the Central Universities (531119200298) and the Special Research Fund of Natural Science (Special Post) of Guizhou University [grant number: (2023) 43].

Conflict of interest

The authors declare that they have no known competing financial interests or personal relationships that could have appeared to influence the work reported in this paper.

Author Contribution Statement

This review is meticulously crafted through a collaborative effort by a dedicated team of researchers to ensure thorough and extensive coverage. **Jingqin Ji** leads the charge in conducting the literature search, organizing the content into sections, and providing succinct summaries of each. Additionally, **Ji** is responsible for creating **Tables 1-6** by analyzing and comparing the $2e^-$ ORR properties of various recently reported M–N–C SAECs and reactors. **Hui Wang** meticulously revises all figures and tables, offering a clear and concise synthesis.

Yanlan Zhao plays a pivotal role in advocating for the importance of this review, compiling relevant literature, and encapsulating the mechanisms and common descriptors of ORR. **Zhao** also authors the content for **Sections 1 and 2**, complete with corresponding figures (**Figures 1-5**). **Yan Wang** focuses on scholarly works surrounding diverse metal active sites and carbon-based substrates, contributing to **Sections 5.1 and 5.2**, as well as the accompanying visual aids (**Figures 11-17**). **Kaifeng Wang** provides a comprehensive summary of the literature on the fabrication techniques and characterization methods of M–N–C SAECs, authoring **Sections 3 and 4** and generating pertinent figures (**Figures 6-10**). **Yuexin Cui** gathers information on modification techniques for M–N–C SAECs and conventional electrosynthesis of H_2O_2 devices, writing **Sections 5.3 and 6.1**, and producing the related figures (**Figures 18, 19, 21**). **Ridha Djellabi** brings together insights from the literature on electrochemical reaction systems for H_2O_2 production in industrial settings, as well as the influence of pH on the efficiency of the $2e^-$ ORR, to construct **Sections 5.4 and 6.2**, along with the figures (**Figures 20 and 22**). **Chuan Xia** encapsulates the essence of the entire manuscript,

highlighting potential opportunities and existing challenges within the field, and is responsible for **Sections 7-8** and **Figures 23**. **Xu Zhao** is instrumental in conceptualizing the overarching framework of the review and providing the necessary financial support. The leading professor, **Xiangming He**, supervises the entire project, collates the references, guides the writing process, and contributes valuable suggestions to enhance the quality of the review. All authors engage in thoughtful discussions and collectively contribute to the refinement and finalization of the manuscript.

References

- [1] D. Aboagye, R. Djellabi, F. Medina, S. Contreras, Radical-mediated photocatalysis for lignocellulosic biomass conversion into value-added chemicals and hydrogen: facts, opportunities and challenges, *Angew. Chem. Int. Ed.* 62 (2023) e202301909.
- [2] J. Ji, X. Yuan, Y. Zhao, L. Jiang, H. Wang, Mechanistic insights of removing pollutant in adsorption and advanced oxidation processes by sludge biochar, *J. Hazard. Mater.* 430 (2022) 128375.
- [3] R. Djellabi, D. Aboagye, M.G. Galloni, V. Vilas Andhalkar, S. Nouacer, W. Nabgan, S. Rtimi, M. Constantí, F. Medina Cabello, S. Contreras, Combined conversion of lignocellulosic biomass into high-value products with ultrasonic cavitation and photocatalytic produced reactive oxygen species—A review, *Bioresour. Technol.* 368 (2023) 128333.
- [4] H. Wang, E. Harkou, A. Constantinou, S.M. Al-Salemc, G. Manos, J. Tang, From photocatalysis to photon–phonon co-driven catalysis for methanol reforming to hydrogen and valuable by-products, *Chem. Soc. Rev.* 54 (2025) 2188–2207.
- [5] R. Ciriminna, L. Albanese, F. Meneguzzo, M. Pagliaro, Hydrogen peroxide: a key chemical for today’s sustainable development, *ChemSusChem* 9 (2016) 3374–3381.
- [6] J.M. Campos-Martin, G. Blanco-Brieva, J.L.G. Fierro, Hydrogen peroxide synthesis: An outlook beyond the anthraquinone process, *Angew. Chem. Int. Ed.* 45 (2006) 6962–6984.
- [7] Z. Deng, S.J. Choi, G. Li, X. Wang, Advancing H₂O₂ electrosynthesis: enhancing electrochemical systems, unveiling emerging applications, and seizing opportunities, *Chem. Soc. Rev.* 53 (2024) 8137–8181.
- [8] Z. Tang, N. Kong, X. Zhang, Y. Liu, P. Hu, S. Mou, P. Liljeström, J. Shi, W. Tan, J.S. Kim, Y. Cao, R. Langer, K.W. Leong, O.C. Farokhzad, W. Tao, A materials-science perspective on tackling COVID-19, *Nat. Rev. Mater.* 5 (2020) 847–860.
- [9] Hans-Joachim, R., and Georg, P. (1940). Production of hydrogen peroxide. U.S. Patent US2158525A.
- [10] J.S. Lim, Y.J. Sa, S.H. Joo, Catalyst design, measurement guidelines, and device integration for H₂O₂ electrosynthesis from oxygen reduction, *Cell Reports Phys. Sci.* 3 (2022) 100987.
- [11] S.J. Freakley, Q. He, J.H. Harthy, L. Lu, D.A. Crole, D.J. Morgan, E.N. Ntainjua, J.K. Edwards, A.F. Carley, A.Y. Borisevich, C.J. Kiely, G.J. Hutchings, Palladium-tin catalysts for the direct synthesis of H₂O₂ with high selectivity, *Science* 351 (2016) 965–968.
- [12] D.W. Flaherty, Direct synthesis of H₂O₂ from H₂ and O₂ on Pd catalysts: current understanding, outstanding questions, and research needs, *ACS Catal.* 8 (2018) 1520–1527.
- [13] S. Yang, A. Verdager-Casadevall, L. Arnarson, L. Silvioli, V. Čolić, R. Frydendal, J. Rossmeisl, I. Chorkendorff, I.E.L. Stephens, Toward the decentralized electrochemical production of H₂O₂: a focus on the catalysis, *ACS Catal.* 8 (2018) 4064–4081.
- [14] Y. Jiang, P. Ni, C. Chen, Y. Lu, P. Yang, B. Kong, A. Fisher, X. Wang, Selective electrochemical H₂O₂ production through two-electron oxygen electrochemistry, *Adv. Energy Mater.* 8 (2018) 17–19.
- [15] S. Siahrostami, A. Verdager-Casadevall, M. Karamad, D. Deiana, P. Malacrida, B. Wickman, M. Escudero-Escribano, E.A. Paoli, R. Frydendal, T.W. Hansen, I. Chorkendorff, I.E.L. Stephens, J. Rossmeisl, Enabling direct H₂O₂ production through rational electrocatalyst design, *Nat. Mater.* 12 (2013) 1137–1143.
- [16] Traube, M. (1887) Electrolytic preparation of hydrogen peroxide at the cathode. *Ber. Kgl. Akad. Wiss. Berlin* 1041, 185

- [17] M. Luo, Z. Zhao, Y. Zhang, Y. Sun, Y. Xing, F. Lv, Y. Yang, X. Zhang, S. Hwang, Y. Qin, J.Y. Ma, F. Lin, D. Su, G. Lu, S. Guo, PdMo bimetallic for oxygen reduction catalysis, *Nature* 574 (2019) 81–85.
- [18] X. Tian, X. Zhao, Y.Q. Su, L. Wang, H. Wang, D. Dang, B. Chi, H. Liu, E.J.M. Hensen, X.W. Lou, B.Y. Xia, Engineering bunched Pt-Ni alloy nanocages for efficient oxygen reduction in practical fuel cells, *Science* 366 (2019) 850–856.
- [19] J.S. Adams, A. Chemburkar, P. Priyadarshini, T. Ricciardulli, Y. Lu, V. Maliekkal, A. Sampath, S. Winikoff, A.M. Karim, M. Neurock, D.W. Flaherty, Solvent molecules form surface redox mediators in situ and cocatalyze O₂ reduction on Pd, *Science* 371 (2021) 626–632.
- [20] J. Gao, H. bin Yang, X. Huang, S.F. Hung, W. Cai, C. Jia, S. Miao, H.M. Chen, X. Yang, Y. Huang, T. Zhang, B. Liu, Enabling Direct H₂O₂ production in acidic media through rational design of transition metal single atom catalyst, *Chem* 6 (2020) 658–674.
- [21] A. Verdager-Casadevall, D. Deiana, M. Karamad, S. Siahrostami, P. Malacrida, T.W. Hansen, J. Rossmeisl, I. Chorkendorff, I.E.L. Stephens, Trends in the electrochemical synthesis of H₂O₂: enhancing activity and selectivity by electrocatalytic site engineering, *Nano Lett.* 14 (2014) 1603–1608.
- [22] L. Li, C. Tang, Y. Zheng, B. Xia, X. Zhou, H. Xu, S.Z. Qiao, Tailoring selectivity of electrochemical hydrogen peroxide generation by tunable pyrrolic-nitrogen-carbon, *Adv. Energy Mater.* 10 (2020) 2000789.
- [23] Z. Lu, G. Chen, S. Siahrostami, Z. Chen, K. Liu, J. Xie, L. Liao, T. Wu, Di. Lin, Y. Liu, T.F. Jaramillo, J.K. Nørskov, Y. Cui, High-efficiency oxygen reduction to hydrogen peroxide catalysed by oxidized carbon materials, *Nat. Catal.* 1 (2018) 156–162.
- [24] R.D. Ross, H. Sheng, Y. Ding, A.N. Janes, D. Feng, J.R. Schmidt, C.U. Segre, S. Jin, Operando elucidation of electrocatalytic and redox mechanisms on a 2D metal organic framework catalyst for efficient electrosynthesis of hydrogen peroxide in neutral media, *J. Am. Chem. Soc.* 144 (2022) 15845–15854.
- [25] M. Wang, N. Zhang, Y. Feng, Z. Hu, Q. Shao, X. Huang, Partially pyrolyzed binary metal–organic framework nanosheets for efficient electrochemical hydrogen peroxide synthesis, *Angew. Chem. Int. Ed.* 59 (2020) 14373–14377.
- [26] H.W. Kim, M.B. Ross, N. Kornienko, L. Zhang, J. Guo, P. Yang, B.D. McCloskey, Efficient hydrogen peroxide generation using reduced graphene oxide-based oxygen reduction electrocatalysts, *Nat. Catal.* 1 (2018) 282–290.
- [27] M.R. Haider, W.-L. Jiang, J.-L. Han, A. Mahmood, R. Djellabi, H. Liu, M.B. Asif, A.-J. Wang, Boosting hydroxyl radical yield via synergistic activation of electrogenerated HOCl/H₂O₂ in electro-fenton-like degradation of contaminants under chloride conditions, *Environ. Sci. Technol.* 57 (2023) 18668–18679.
- [28] X. Liu, L. Dai, Carbon-based metal-free catalysts, *Nat. Rev. Mater.* 1 (2016) 16064.
- [29] L. Dai, Y. Xue, L. Qu, H.J. Choi, J.B. Baek, Metal-free catalysts for oxygen reduction reaction, *Chem. Rev.* 115 (2015) 4823–4892.
- [30] Y. Jia, L. Zhang, L. Zhuang, H. Liu, X. Yan, X. Wang, J. Liu, J. Wang, Y. Zheng, Z. Xiao, E. Taran, J. Chen, D. Yang, Z. Zhu, S. Wang, L. Dai, X. Yao, Identification of active sites for acidic oxygen reduction on carbon catalysts with and without nitrogen doping, *Nat. Catal.* 2 (2019) 688–695.
- [31] H. Fei, J. Dong, Y. Feng, C.S. Allen, C. Wan, B. Voloskiy, M. Li, Z. Zhao, Y. Wang, H. Sun, P. An, W. Chen, Z. Guo, C. Lee, D. Chen, I. Shakir, M. Liu, T. Hu, Y. Li, A.I. Kirkland, X. Duan, Y. Huang, General synthesis and definitive structural identification of MN₄C₄ single-atom catalysts with tunable electrocatalytic activities, *Nat. Catal.* 1 (2018) 63–72.
- [32] H. Xu, S. Zhang, J. Geng, G. Wang, H. Zhang, Cobalt single atom catalysts for the efficient electrosynthesis of hydrogen peroxide, *Inorg. Chem. Front.* 8 (2021) 2829–2834.
- [33] X. Zhang, L. Truong-Phuoc, X. Liao, G. Tuci, E. Fonda, V. Papaefthymiou, S. Zafeirotas, G. Giambastiani, S. Pronkin, C. Pham-Huu, An open gate for high-density metal ions in N-doped carbon networks: powering Fe-N-C catalyst efficiency in the oxygen reduction reaction, *ACS Catal.* 11 (2021) 8915–8928.
- [34] L. Yang, D. Cheng, H. Xu, X. Zeng, X. Wan, J. Shui, Z. Xiang, D. Cao, Unveiling the high-activity origin of single-atom iron catalysts for oxygen reduction reaction, *Proc. Natl. Acad. Sci. U. S. A.* 115 (2018) 6626–6631.
- [35] B. Qiao, A. Wang, X. Yang, L.F. Allard, Z. Jiang, Y. Cui, J. Liu, J. Li, T. Zhang, Single-atom catalysis of CO oxidation using Pt₁/FeO_x, *Nat. Chem.* 3 (2011) 634–641.
- [36] R. Svensson, H. Grönbeck, Site communication in direct formation of H₂O₂ over single-atom Pd@Au nanoparticles, *J. Am. Chem. Soc.* 145 (2023) 11579–11588.

- [37] F. Zhang, Y. Zhu, C. Tang, Y. Chen, B. Qian, Z. Hu, Y.C. Chang, C.W. Pao, Q. Lin, S.A. Kazemi, Y. Wang, L. Zhang, X. Zhang, H. Wang, High-efficiency electrosynthesis of hydrogen peroxide from oxygen reduction enabled by a tungsten single atom catalyst with unique terdentate N_1O_2 coordination, *Adv. Funct. Mater.* 32 (2022) 2110224.
- [38] Z. Wei, B. Deng, P. Chen, T. Zhao, S. Zhao, Palladium-based single atom catalysts for high-performance electrochemical production of hydrogen peroxide, *Chem. Eng. J.* 428 (2022) 131112.
- [39] J. Zhang, H. Yang, B. Liu, Coordination engineering of single-atom catalysts for the oxygen reduction reaction: A Review, *Adv. Energy Mater.* 11 (2021) 2002473.
- [40] X. Li, L. Liu, X. Ren, J. Gao, Y. Huang, B. Liu, Microenvironment modulation of single-atom catalysts and their roles in electrochemical energy conversion, *Sci. Adv.* 6 (2020) eabb6833.
- [41] S.K. Kaiser, Z. Chen, D. Faust Akl, S. Mitchell, J. Pérez-Ramírez, Single-atom catalysts across the Periodic Table, *Chem. Rev.* 120 (2020) 11703–11809.
- [42] B. Tang, Q. Ji, X. Zhang, R. Shi, J. Ma, Z. Zhuang, M. Sun, H. Wang, R. Liu, H. Liu, C. Wang, Z. Guo, L. Lu, P. Jiang, D. Wang, W. Yan, Symmetry breaking of FeN_4 moiety via edge defects for acidic oxygen reduction reaction, *Angew. Chem. Int. Ed.* 64 (2025) e202424135.
- [43] J. Bai, Y. Lian, Y. Deng, M. Xiang, P. Xu, Q. Zhou, Y. Tang, Y. Su, Simultaneous integration of Fe clusters and NiFe dual single atoms in nitrogen-doped carbon for oxygen reduction reaction, *Nano Res.* 17 (2024) 2291–2297.
- [44] M.M. Montemore, M.A. Van Spronsen, R.J. Madix, C.M. Friend, O_2 Activation by Metal Surfaces: implications for bonding and reactivity on heterogeneous catalysts, *Chem. Rev.* 118 (2018) 2816–2862.
- [45] M.L. Pegis, C.F. Wise, D.J. Martin, J.M. Mayer, Oxygen reduction by homogeneous molecular catalysts and electrocatalysts, *Chem. Rev.* 118 (2018) 2340–2391.
- [46] S. Yang, J. Kim, Y.J. Tak, A. Soon, H. Lee, Single-atom catalyst of platinum supported on titanium nitride for selective electrochemical reactions, *Angew. Chem. Int. Ed.* 55 (2016) 2058–2062.
- [47] Y. Sun, L. Silviali, N.R. Sahraie, W. Ju, J. Li, A. Zitolo, S. Li, A. Bagger, L. Arnarson, X. Wang, T. Moeller, D. Bernsmeier, J. Rossmeisl, F. Jaouen, P. Strasser, Activity-selectivity trends in the electrochemical production of hydrogen peroxide over single-site metal-nitrogen-carbon catalysts, *J. Am. Chem. Soc.* 141 (2019) 12372–12381.
- [48] E. Jung, H. Shin, B.H. Lee, V. Efremov, S. Lee, H.S. Lee, J. Kim, W. Hooch Antink, S. Park, K.S. Lee, S.P. Cho, J.S. Yoo, Y.E. Sung, T. Hyeon, Atomic-level tuning of Co–N–C catalyst for high-performance electrochemical H_2O_2 production, *Nat. Mater.* 19 (2020) 436–442.
- [49] C. Tang, L. Chen, H. Li, L. Li, Y. Jiao, Y. Zheng, H. Xu, K. Davey, S.Z. Qiao, Tailoring acidic oxygen reduction selectivity on single-atom catalysts via modification of first and second coordination spheres, *J. Am. Chem. Soc.* 143 (2021) 7819–7827.
- [50] C. Xiao, L. Cheng, Y. Zhu, G. Wang, L. Chen, Y. Wang, R. Chen, Y. Li, C. Li, Super-coordinated nickel $N_4Ni_1O_2$ site single-atom catalyst for selective H_2O_2 electrosynthesis at high current densities, *Angew. Chem. Int. Ed.* 61 (2022) e202206544.
- [51] B.H. Lee, H. Shin, A.S. Rasouli, H. Choubisa, P. Ou, R. Dorakhan, I. Grigioni, G. Lee, E. Shirzadi, R.K. Miao, J. Wicks, S. Park, H.S. Lee, J. Zhang, Y. Chen, Z. Chen, D. Sinton, T. Hyeon, Y.E. Sung, E.H. Sargent, Supramolecular tuning of supported metal phthalocyanine catalysts for hydrogen peroxide electrosynthesis, *Nat. Catal.* 6 (2023) 234–243.
- [52] L.-Y. Dong, J.-S. Wang, T.-Y. Li, T. Wu, X. Hu, Y.-T. Wu, M.-Y. Zhu, G.-P. Hao, A.-H. Lu, Boundary-rich carbon-based electrocatalysts with manganese(II)-coordinated active environment for selective synthesis of hydrogen peroxide, *Angew. Chem. Int. Ed.* 63 (2024) e202317660.
- [53] X. Yang, Y. Zeng, W. Alnoush, Y. Hou, D. Higgins, G. Wu, Tuning two-electron oxygen-reduction pathways for H_2O_2 electrosynthesis via engineering atomically dispersed single metal site catalysts, *Adv. Mater.* 34 (2022) 2107954.
- [54] Z. Gao, Q. Zhu, Y. Cao, C. Wang, L. Liu, J. Zhu, Design strategies of carbon-based single-atom catalysts for efficient electrochemical hydrogen peroxide production, *J. Environ. Chem. Eng.* 11 (2023) 109572.
- [55] K.Y. Chen, Y.X. Huang, R.C. Jin, B.C. Huang, Single atom catalysts for use in the selective production of hydrogen peroxide via two-electron oxygen reduction reaction: mechanism, activity, and structure optimization, *Appl. Catal. B Environ.* 337 (2023) 122987.
- [56] M. Song, W. Liu, J. Zhang, C. Zhang, X. Huang, D. Wang, Single-atom catalysts for H_2O_2 electrosynthesis via two-electron oxygen reduction reaction, *Adv. Funct. Mater.* 33 (2023) 2212087.
- [57] Y. Tong, L. Wang, F. Hou, S.X. Dou, J. Liang, Electrocatalytic oxygen reduction to produce hydrogen peroxide: rational design from single-atom catalysts to devices, *Electrochem. Energy Rev.* 5 (2022) 7.

- [58] R. Shen, W. Chen, Q. Peng, S. Lu, L. Zheng, X. Cao, Y. Wang, W. Zhu, J. Zhang, Z. Zhuang, C. Chen, D. Wang, Y. Li, High-concentration single atomic Pt sites on hollow CuS_x for Selective O₂ Reduction to H₂O₂ in Acid Solution, *Chem* 5 (2019) 2099–2110.
- [59] Q. Chang, P. Zhang, A.H.B. Mostaghimi, X. Zhao, S.R. Denny, J.H. Lee, H. Gao, Y. Zhang, H.L. Xin, S. Siahrostami, J.G. Chen, Z. Chen, Promoting H₂O₂ production via 2-electron oxygen reduction by coordinating partially oxidized Pd with defect carbon, *Nat. Commun.* 11 (2020) 2178.
- [60] P. Strasser, M. Gliech, S. Kuehl, T. Moeller, Electrochemical processes on solid shaped nanoparticles with defined facets, *Chem. Soc. Rev.* 47 (2018) 715–735.
- [61] P. Strasser, Free electrons to molecular bonds and back: closing the energetic oxygen reduction (ORR)-oxygen evolution (OER) cycle using core-shell nanoelectrocatalysts, *Acc. Chem. Res.* 49 (2016) 2658–2668.
- [62] X. Deng, C. Zheng, Y. Li, Z. Zhou, J. Wang, Y. Ran, Z. Hu, F. Yang, L. Li, Conductive catalysis by subsurface transition metals, *Natl. Sci. Rev.* 11 (2024) nwae015.
- [63] X. Wang, Z. Kang, D. Wang, Y. Zhao, X. Xiang, H. Shang, B. Zhang, Electronic structure regulation of the Fe-based single-atom catalysts for oxygen electrocatalysis, *Nano Energy* 121 (2024) 109268.
- [64] C. Chen, J. Chai, M. Sun, T. Guo, J. Lin, Y. Zhou, Z. Sun, F. Zhang, L. Zhang, W. Chen, Y. Li, Asymmetrically coordinated ZnCoFe hetero-trimetallic atom catalyst enhances electrocatalytic oxygen reaction, *Energy Environ. Sci.* 17 (2024) 2298–2308.
- [65] W. Peng, F. Li, S. Kong, C. Guo, H. Wu, J. Wang, Y. Shen, X. Meng, M. Zhang, Recent advances in nickel-based catalysts in eCO₂RR for carbon neutrality, *Carbon Energy* 6 (2024) e498.
- [66] V. Tripković, E. Skúlason, S. Siahrostami, J.K. Nørskov, J. Rossmeisl, The oxygen reduction reaction mechanism on Pt (111) from density functional theory calculations, *Electrochim. Acta* 55 (2010) 7975–7981.
- [67] A. Kulkarni, S. Siahrostami, A. Patel, J.K. Nørskov, Understanding catalytic activity trends in the oxygen reduction reaction, *Chem. Rev.* 118 (2018) 2302–2312.
- [68] Y. Jiao, Y. Zheng, M. Jaroniec, S.Z. Qiao, Design of electrocatalysts for oxygen- and hydrogen-involving energy conversion reactions, *Chem. Soc. Rev.* 44 (2015) 2060–2086.
- [69] Y. Nie, L. Li, Z. Wei, Recent advancements in Pt and Pt-free catalysts for oxygen reduction reaction, *Chem. Soc. Rev.* 44 (2015) 2168–2201.
- [70] E. Yeager, Dioxygen electrocatalysis: mechanisms in relation to catalyst structure, *J. Mol. Catal.* 38 (1986) 5–25.
- [71] S. Chen, A. Kucernak, Electrocatalysis under conditions of high mass transport: investigation of hydrogen oxidation on single submicron Pt particles supported on carbon, *J. Phys. Chem. B* 108 (2004) 13984–13994.
- [72] J. Wang, Z. Huang, W. Liu, C. Chang, H. Tang, Z. Li, W. Chen, C. Jia, T. Yao, S. Wei, Y. Wu, Y. Li, Design of N-coordinated dual-metal sites: a stable and active Pt-free catalyst for acidic oxygen reduction reaction, *J. Am. Chem. Soc.* 139 (2017) 17281–17284.
- [73] S. Fukuzumi, Y. Yamada, K.D. Karlin, Hydrogen peroxide as a sustainable energy carrier: Electrocatalytic production of hydrogen peroxide and the fuel cell, *Electrochim. Acta* 82 (2012) 493–511.
- [74] J.S. Jirkovský, I. Panas, E. Ahlberg, M. Halasa, S. Romani, D.J. Schiffrin, Single atom hot-spots at Au-Pd nanoalloys for electrocatalytic H₂O₂ production, *J. Am. Chem. Soc.* 133 (2011) 19432–19441.
- [75] X. Zhao, Y. Liu, Origin of selective production of hydrogen peroxide by electrochemical oxygen reduction, *J. Am. Chem. Soc.* 143 (2021) 9423–9428.
- [76] C. Xia, S. Back, S. Ringe, K. Jiang, F. Chen, X. Sun, S. Siahrostami, K. Chan, H. Wang, Confined local oxygen gas promotes electrochemical water oxidation to hydrogen peroxide, *Nat. Catal.* 3 (2020) 125–134.
- [77] X. Tan, H. Li, W. Zhang, K. Jiang, S. Zhai, W. Zhang, N. Chen, H. Li, Z. Li, Square-pyramidal Fe-N₄ with defect-modulated O-coordination: two-tier electronic structure fine-tuning for enhanced oxygen reduction, *Chem Catal.* 2 (2022) 816–835.
- [78] I. Johnson, J. Han, M. Chen, 3D nanoporous graphene based single-atom electrocatalysts for energy conversion and storage, *Accounts Mater. Res.* 3 (2022) 1011–1021.
- [79] Z.H. Zhu, B. Yu, W. Sun, S. Chen, Y. Wang, X. Li, L.P. Lv, Triazine organic framework derived Fe single-atom bifunctional electrocatalyst for high performance zinc air batteries, *J. Power Sources* 542 (2022) 231583.
- [80] N. Han, W. Zhang, W. Guo, H. Pan, B. Jiang, L. Xing, H. Tian, G. Wang, X. Zhang, J. Fransaer,

- Designing oxide catalysts for oxygen electrocatalysis: insights from mechanism to application, *Nano-Micro Lett.* 15 (2023) 185.
- [81] J. Gao, B. Liu, Progress of electrochemical hydrogen peroxide synthesis over single atom catalysts, *ACS Mater. Lett.* 2 (2020) 1008–1024.
- [82] K. Liu, G. Wu, G. Wang, Role of local carbon structure surrounding FeN₄ Sites in boosting the catalytic activity for oxygen reduction, *J. Phys. Chem. C* 121 (2017) 11319–11324.
- [83] C. Costentin, S. Drouet, M. Robert, J.M. Savéant, Turnover numbers, turnover frequencies, and overpotential in molecular catalysis of electrochemical reactions. cyclic voltammetry and preparative-scale electrolysis, *J. Am. Chem. Soc.* 134 (2012) 11235–11242.
- [84] Z. Chen, S. Chen, S. Siahrostami, P. Chakthranont, C. Hahn, D. Nordlund, S. Dimosthenis, J.K. Nørskov, Z. Bao, T.F. Jaramillo, Development of a reactor with carbon catalysts for modular-scale, low-cost electrochemical generation of H₂O₂, *React. Chem. Eng.* 2 (2017) 239–245.
- [85] M. Campos, W. Siriwatcharapiboon, R.J. Potter, S.L. Horswell, Selectivity of cobalt-based catalysts towards hydrogen peroxide formation during the reduction of oxygen, *Catal. Today* 202 (2013) 135–143.
- [86] A. Moraes, M.H.M.T. Assumpção, F.C. Simões, V.S. Antonin, M.R.V. Lanza, P. Hammer, M.C. Santos, Surface and catalytical effects on treated carbon materials for hydrogen peroxide electrogeneration, *Electrocatalysis* 7 (2016) 60–69.
- [87] X. Shi, S. Siahrostami, G.L. Li, Y. Zhang, P. Chakthranont, F. Studt, T.F. Jaramillo, X. Zheng, J.K. Nørskov, Understanding activity trends in electrochemical water oxidation to form hydrogen peroxide, *Nat. Commun.* 8 (2017) 701.
- [88] C. Xia, J.Y. (Timothy) Kim, H. Wang, Recommended practice to report selectivity in electrochemical synthesis of H₂O₂, *Nat. Catal.* 3 (2020) 605–607.
- [89] L. Fu, S.J. You, F.L. Yang, M.M. Gao, X.H. Fang, G.Q. Zhang, Synthesis of hydrogen peroxide in microbial fuel cell, *J. Chem. Technol. Biotechnol.* 85 (2010) 715–719.
- [90] F. Calle-Vallejo, A. Krabbe, J.M. García-Lastra, How covalence breaks adsorption-energy scaling relations and solvation restores them, *Chem. Sci.* 8 (2016) 124–130.
- [91] R. Zhou, Y. Zheng, M. Jaroniec, S.Z. Qiao, Determination of the electron transfer number for the oxygen reduction reaction: from theory to experiment, *ACS Catal.* 6 (2016) 4720–4728.
- [92] Y. Wang, R. Shi, L. Shang, G.I.N. Waterhouse, J. Zhao, Q. Zhang, L. Gu, T. Zhang, High-efficiency oxygen reduction to hydrogen peroxide catalyzed by nickel single-atom catalysts with tetradentate N₂O₂ coordination in a three-phase flow cell, *Angew. Chem. Int. Ed.* 59 (2020) 13057–13062.
- [93] Q. Zhang, M. Zhou, G. Ren, Y. Li, Y. Li, X. Du, Highly efficient electrosynthesis of hydrogen peroxide on a superhydrophobic three-phase interface by natural air diffusion, *Nat. Commun.* 11 (2020) 1731.
- [94] Q. Zhang, X. Tan, N.M. Bedford, Z. Han, L. Thomsen, S. Smith, R. Amal, X. Lu, Direct insights into the role of epoxy groups on cobalt sites for acidic H₂O₂ production, *Nat. Commun.* 11 (2020) 4181.
- [95] Y.H. Wang, M.L. Pegis, J.M. Mayer, S.S. Stahl, Molecular cobalt catalysts for O₂ reduction: low-overpotential production of H₂O₂ and comparison with iron-based catalysts, *J. Am. Chem. Soc.* 139 (2017) 16458–16461.
- [96] A.N. Oldacre, A.E. Friedman, T.R. Cook, A self-assembled cofacial cobalt porphyrin prism for oxygen reduction catalysis, *J. Am. Chem. Soc.* 139 (2017) 1424–1427.
- [97] T. He, A.R. Puente-Santiago, S. Xia, M.A. Ahsan, G. Xu, R. Luque, Experimental and theoretical advances on single atom and atomic cluster-decorated low-dimensional platforms towards superior electrocatalysts, *Adv. Energy Mater.* 12 (2022) 2200493.
- [98] M. Pang, M. Yang, H. Zhang, Y. Shen, Z. Kong, J. Ye, C. Shan, Y. Wang, J. An, W. Li, X. Gao, J. Song, Synthesis techniques, mechanism, and prospects of high-loading single-atom catalysts for oxygen reduction reactions, *Nano Res.* 17 (2024) 9371–9396.
- [99] X. Liao, J. Hou, Y. Wang, H. Zhang, Y. Sun, X. Li, S. Tang, K. Kato, M. Yamauchi, Z. Jiang, An active, selective, and stable manganese oxide-supported atomic Pd catalyst for aerobic oxidation of 5-hydroxymethylfurfural, *Green Chem.* 21 (2019) 4194–4203.
- [100] M. Yan, H. Yang, Z. Gong, J. Zhu, C. Allen, T. Cheng, Sulfur-tuned main-group Sb–N–C catalysts for selective 2-electron and 4-electron oxygen reduction, *Adv. Mater.* 36 (2024) 2402963.
- [101] J. Liu, Catalysis by supported single metal atoms, *ACS Catal.* 7 (2017) 34–59.
- [102] X. Jin, R. Wang, L. Zhang, R. Si, M. Shen, M. Wang, J. Tian, J. Shi, Electron configuration modulation of nickel single atoms for elevated photocatalytic hydrogen evolution, *Angew. Chem. Int. Ed.* 59 (2020) 6827–6831.

- [103] G. Chen, P. Liu, Z. Liao, F. Sun, Y. He, H. Zhong, T. Zhang, E. Zschech, M. Chen, G. Wu, J. Zhang, X. Feng, Zinc-mediated template synthesis of Fe-N-C electrocatalysts with densely accessible Fe-N_x active sites for efficient oxygen reduction, *Adv. Mater.* 32 (2020) 1907399.
- [104] K. Yuan, D. Lützenkirchen-Hecht, L. Li, L. Shuai, Y. Li, R. Cao, M. Qiu, X. Zhuang, M.K.H. Leung, Y. Chen, U. Scherf, Boosting oxygen reduction of single iron active sites via geometric and electronic engineering: nitrogen and phosphorus dual coordination, *J. Am. Chem. Soc.* 142 (2020) 2404–2412.
- [105] B.H. Lee, S. Park, M. Kim, A.K. Sinha, S.C. Lee, E. Jung, W.J. Chang, K.S. Lee, J.H. Kim, S.P. Cho, H. Kim, K.T. Nam, T. Hyeon, Reversible and cooperative photoactivation of single-atom Cu/TiO₂ photocatalysts, *Nat. Mater.* 18 (2019) 620–626.
- [106] M. Yoo, Y.S. Yu, H. Ha, S. Lee, J.S. Choi, S. Oh, E. Kang, H. Choi, H. An, K.S. Lee, J.Y. Park, R. Celestre, M.A. Marcus, K. Nowrouzi, D. Taube, D.A. Shapiro, W.C. Jung, C. Kim, H.Y. Kim, A tailored oxide interface creates dense Pt single-atom catalysts with high catalytic activity, *Energy Environ. Sci.* 13 (2020) 1231–1239.
- [107] S. Hejazi, S. Mohajernia, B. Osuagwu, G. Zoppellaro, P. Andryskova, O. Tomanec, S. Kment, R. Zbořil, P. Schmuki, On the controlled loading of single platinum atoms as a Co-catalyst on TiO₂ anatase for optimized photocatalytic H₂ generation, *Adv. Mater.* 32 (2020) 1908505.
- [108] L. Zhang, Y. Jia, G. Gao, X. Yan, N. Chen, J. Chen, M.T. Soo, B. Wood, D. Yang, A. Du, X. Yao, Graphene defects trap atomic Ni species for hydrogen and oxygen evolution reactions, *Chem* 4 (2018) 285–297.
- [109] J. Wan, W. Chen, C. Jia, L. Zheng, J. Dong, X. Zheng, Y. Wang, W. Yan, C. Chen, Q. Peng, D. Wang, Y. Li, Defect effects on TiO₂ nanosheets: stabilizing single atomic site Au and promoting catalytic properties, *Adv. Mater.* 30 (2018) 1705369.
- [110] H. Wei, K. Huang, D. Wang, R. Zhang, B. Ge, J. Ma, B. Wen, S. Zhang, Q. Li, M. Lei, C. Zhang, J. Irawan, L.M. Liu, H. Wu, Iced photochemical reduction to synthesize atomically dispersed metals by suppressing nanocrystal growth, *Nat. Commun.* 8 (2017) 1049.
- [111] Y. Huang, J. Xiong, Z. Zou, Z. Chen, Emerging strategies for the synthesis of correlated single atom Catalysts, *Adv. Mater.* 37 (2024) 2312182.
- [112] H. Xu, S. Zhang, X. Zhang, M. Xu, M. Han, L.R. Zheng, Y. Zhang, G. Wang, H. Zhang, H. Zhao, Atomically dispersed iron regulating electronic structure of iron atom clusters for electrocatalytic H₂O₂ production and biomass upgrading, *Angew. Chem. Int. Ed.* 62 (2023) e202314414.
- [113] T. Iwasaki, Y. Masuda, H. Ogihara, I. Yamanaka, Direct synthesis of pure H₂O₂ aqueous solution by CoTPP/ketjen-black electrocatalyst and the fuel cell reactor, *Electrocatalysis* 9 (2018) 236–242.
- [114] X. Wang, Y. Zhang, J. Wu, Z. Zhang, Q. Liao, Z. Kang, Y. Zhang, Single-atom engineering to ignite 2D transition metal dichalcogenide based catalysis: fundamentals, progress, and beyond, *Chem. Rev.* 122 (2022) 1273–1348.
- [115] J. Yang, W.H. Li, K. Xu, S. Tan, D. Wang, Y. Li, Regulating the tip effect on single-atom and cluster catalysts: forming reversible oxygen species with high efficiency in chlorine evolution reaction, *Angew. Chem. Int. Ed.* 61 (2022) e202200366.
- [116] Y. Tian, M. Li, Z. Wu, Q. Sun, D. Yuan, B. Johannessen, L. Xu, Y. Wang, Y. Dou, H. Zhao, S. Zhang, Edge-hosted Atomic Co–N₄ sites on hierarchical porous carbon for highly selective two-electron oxygen reduction reaction, *Angew. Chem. Int. Ed.* 61 (2022) e202213296.
- [117] I. Bilecka, M. Niederberger, Microwave chemistry for inorganic nanomaterials synthesis, *Nanoscale* 2 (2010) 1269–1528.
- [118] H. Fei, J. Dong, C. Wan, Z. Zhao, X. Xu, Z. Lin, Y. Wang, H. Liu, K. Zang, J. Luo, S. Zhao, W. Hu, W. Yan, I. Shakir, Y. Huang, X. Duan, Microwave-assisted rapid synthesis of graphene-supported single atomic metals, *Adv. Mater.* 30 (2018) 1802146.
- [119] H. Gong, Z. Wei, Z. Gong, J. Liu, G. Ye, M. Yan, J. Dong, C. Allen, J. Liu, K. Huang, R. Liu, G. He, S. Zhao, H. Fei, Low-coordinated Co-N-C on oxygenated graphene for efficient electrocatalytic H₂O₂ production, *Adv. Funct. Mater.* 32 (2022) 2106886.
- [120] S. Wei, A. Li, J.C. Liu, Z. Li, W. Chen, Y. Gong, Q. Zhang, W.C. Cheong, Y. Wang, L. Zheng, H. Xiao, C. Chen, D. Wang, Q. Peng, L. Gu, X. Han, J. Li, Y. Li, Direct observation of noble metal nanoparticles transforming to thermally stable single atoms, *Nat. Nanotechnol.* 13 (2018) 856–861.
- [121] H. Zhou, Y. Zhao, J. Xu, H. Sun, Z. Li, W. Liu, T. Yuan, W. Liu, X. Wang, W.C. Cheong, Z. Wang, X. Wang, C. Zhao, Y. Yao, W. Wang, F. Zhou, M. Chen, B. Jin, R. Sun, J. Liu, X. Hong, T. Yao, S. Wei, J. Luo, Y. Wu, Recover the activity of sintered supported catalysts by nitrogen-doped carbon atomization, *Nat. Commun.* 11 (2020) 335.

- [122] M. Zhang, Y.G. Wang, W. Chen, J. Dong, L. Zheng, J. Luo, J. Wan, S. Tian, W.C. Cheong, D. Wang, Y. Li, Metal (hydr)oxides@polymer core-shell strategy to metal single-atom materials, *J. Am. Chem. Soc.* 139 (2017) 10976–10979.
- [123] M. Liu, L. Wang, K. Zhao, S. Shi, Q. Shao, L. Zhang, X. Sun, Y. Zhao, J. Zhang, Atomically dispersed metal catalysts for the oxygen reduction reaction: synthesis, characterization, reaction mechanisms and electrochemical energy applications, *Energy Environ. Sci.* 12 (2019) 2890–2923.
- [124] Z. Li, D. Wang, Y. Wu, Y. Li, Recent advances in the precise control of isolated single-site catalysts by chemical methods, *Natl. Sci. Rev.* 5 (2018) 673–689.
- [125] J. Wang, Z. Li, Y. Wu, Y. Li, Fabrication of single-atom catalysts with precise structure and high metal loading, *Adv. Mater.* 30 (2018) 1801649.
- [126] M. Moliner, J.E. Gabay, C.E. Kliewer, R.T. Carr, J. Guzman, G.L. Casty, P. Serna, A. Corma, Reversible transformation of Pt nanoparticles into single atoms inside high-silica chabazite zeolite, *J. Am. Chem. Soc.* 138 (2016) 15743–15750.
- [127] J. Jones, H. Xiong, A.T. DeLaRiva, E.J. Peterson, H. Pham, S.R. Challa, G. Qi, S. Oh, M.H. Wiebenga, X.I.P. Hernández, Y. Wang, A.K. Datye, Thermally stable single-atom platinum-on-ceria catalysts via atom trapping, *Science* 353 (2016) 150–154.
- [128] Y. Qu, B. Chen, Z. Li, X. Duan, L. Wang, Y. Lin, T. Yuan, F. Zhou, Y. Hu, Z. Yang, C. Zhao, J. Wang, C. Zhao, Y. Hu, G. Wu, Q. Zhang, Q. Xu, B. Liu, P. Gao, R. You, W. Huang, L. Zheng, L. Gu, Y. Wu, Y. Li, Thermal emitting strategy to synthesize atomically dispersed Pt metal sites from bulk Pt metal, *J. Am. Chem. Soc.* 141 (2019) 4505–4509.
- [129] Y. Qu, Z. Li, W. Chen, Y. Lin, T. Yuan, Z. Yang, C. Zhao, J. Wang, C. Zhao, X. Wang, F. Zhou, Z. Zhuang, Y. Wu, Y. Li, Direct transformation of bulk copper into copper single sites via emitting and trapping of atoms, *Nat. Catal.* 1 (2018) 781–786.
- [130] L. Chang, X. Liu, J. Luo, C.Y. Lee, J. Zhang, X. Fan, W. Zhang, Physiochemical coupled dynamic nanosphere lithography enabling multiple metastructures from single mask, *Adv. Mater.* 36 (2024) 2310469.
- [131] Y. Guo, Q. Zhu, Z. Wang, Y. Ye, J. Hu, J. Shang, B. Li, Z. Du, Minutes-fast production of vacancy-enriched MXenes as an efficient platform for single-atom electrocatalysts, *Adv. Energy Mater.* 14 (2024) 2304149.
- [132] X. Fan, W. Chen, L. Xie, X. Liu, Y. Ding, L. Zhang, M. Tang, Surface-enriched single-Bi-atoms tailoring of Pt nanorings for direct methanol fuel cells with ultralow-Pt-loading, *Adv. Mater.* 36 (2024) 2313179.
- [133] J. Hu, W. Shang, C. Xin, J. Guo, X. Cheng, S. Zhang, S. Song, W. Liu, F. Ju, J. Hou, Y. Shi, Uncovering dynamic edge-sites in atomic Co–N–C electrocatalyst for selective hydrogen peroxide production, *Angew. Chem. Int. Ed.* 62 (2023) e202304754.
- [134] Y. Hu, B. Li, C. Yu, H. Fang, Z. Li, Mechanochemical preparation of single atom catalysts for versatile catalytic applications: A perspective review, *Mater. Today* 63 (2023) 288–312.
- [135] A.C.M. Loy, S.Y. Teng, B.S. How, X. Zhang, K.W. Cheah, V. Butera, W.D. Leong, B.L.F. Chin, C.L. Yiin, M.J. Taylor, G. Kyriakou, Elucidation of single atom catalysts for energy and sustainable chemical production: synthesis, characterization and frontier science, *Prog. Energy Combust. Sci.* 96 (2023) 101074.
- [136] Y. Peng, P.D. Nellist, S.J. Pennycook, HAADF-STEM imaging with sub-angstrom probes: a full Bloch wave analysis, *J. Electron Microsc.* 53 (2004) 257–266.
- [137] R. Chen, S. Chen, L. Wang, D. Wang, Nanoscale metal particle modified single-atom catalyst: synthesis, characterization, and application, *Adv. Mater.* 36 (2024) 2304713.
- [138] S. Zhang, Z. Tao, M. Xu, L. Kan, C. Guo, J. Liu, L. He, M. Du, Z. Zhang, Single-atom Co–O₄ sites embedded in a defective-rich porous carbon layer for efficient H₂O₂ electrosynthesis, *Small* 23 (2024) 2310468.
- [139] G. Wei, Y. Li, X. Liu, J. Huang, M. Liu, D. Luan, S. Gao, X.W. Lou, Single-atom zinc sites with synergetic multiple coordination shells for electrochemical H₂O₂ production, *Angew. Chem. Int. Ed.* 62 (2023) e202313914.
- [140] W. Ma, J. Mao, X. Yang, C. Pan, W. Chen, M. Wang, P. Yu, L. Mao, Y. Li, A single-atom Fe–N₄ catalytic site mimicking bifunctional antioxidative enzymes for oxidative stress cytoprotection, *Chem. Commun.* 55 (2019) 159–162.
- [141] J.A. Small, The analysis of particles at low accelerating voltages (≤ 10 kV) with energy dispersive X-ray spectroscopy (EDS), *J. Res. Natl. Inst. Stand. Technol.* 107 (2002) 555–566.

- [142]K. Qi, X. Cui, L. Gu, S. Yu, X. Fan, M. Luo, S. Xu, N. Li, L. Zheng, Q. Zhang, J. Ma, Y. Gong, F. Lv, K. Wang, H. Huang, W. Zhang, S. Guo, W. Zheng, P. Liu, Single-atom cobalt array bound to distorted 1T MoS₂ with ensemble effect for hydrogen evolution catalysis, *Nat. Commun.* 10 (2019) 1038.
- [143]H. Zhang, G. Liu, L. Shi, J. Ye, Single-atom catalysts: emerging multifunctional materials in heterogeneous catalysis, *Adv. Energy Mater.* 8 (2018) 1701343.
- [144]C.H.M. Van Oversteeg, H.Q. Doan, F.M.F. De Groot, T. Cuk, In situ X-ray absorption spectroscopy of transition metal based water oxidation catalysts, *Chem. Soc. Rev.* 46 (2017) 102–125.
- [145]E. Vorobyeva, E. Fako, Z. Chen, S.M. Collins, D. Johnstone, P.A. Midgley, R. Hauert, O. V. Safonova, G. Vilé, N. López, S. Mitchell, J. Pérez-Ramírez, Atom-by-atom resolution of structure–function relations over low-nuclearity metal catalysts, *Angew. Chem. Int. Ed.* 58 (2019) 8724–8729.
- [146]D. Pacilé, M. Papagno, A.F. Rodríguez, M. Grioni, L. Papagno, C. Girit, J.C. Meyer, G.E. Begtrup, A. Zettl, Near-edge X-ray absorption fine-structure investigation of graphene, *Phys. Rev. Lett.* 101 (2008) 066806.
- [147]T. Zheng, K. Jiang, N. Ta, Y. Hu, J. Zeng, J. Liu, H. Wang, Large-scale and highly selective CO₂ electrocatalytic reduction on nickel single-atom catalyst, *Joule* 3 (2019) 265–278.
- [148]A.M. Venezia, X-ray photoelectron spectroscopy (XPS) for catalysts characterization, *Catal. Today* 77 (2003) 359–370.
- [149]S. Louisia, M.T.M. Koper, R. V Mom, Prospects for electrochemical X-ray photoelectron spectroscopy as a powerful electrochemical interface characterization technique, *Curr. Opin. Electrochem.* 45 (2024) 101462.
- [150]D. Song, J. Li, Q. Cai, In situ diffuse reflectance FTIR study of CO adsorbed on a cobalt catalyst supported by silica with different pore sizes, *J. Phys. Chem. C* 111 (2007) 18970–18979.
- [151]S. Chen, W.H. Li, W. Jiang, J. Yang, J. Zhu, L. Wang, H. Ou, Z. Zhuang, M. Chen, X. Sun, D. Wang, Y. Li, MOF encapsulating N-heterocyclic carbene-ligated copper single-atom site catalyst towards efficient methane electrosynthesis, *Angew. Chem. Int. Ed.* 61 (2022) e202114450.
- [152]L. Zhang, X. Yang, Q. Yuan, Z. Wei, J. Ding, T. Chu, C. Rong, Q. Zhang, Z. Ye, F.Z. Xuan, Y. Zhai, B. Zhang, X. Yang, Elucidating the structure-stability relationship of Cu single-atom catalysts using operando surface-enhanced infrared absorption spectroscopy, *Nat. Commun.* 14 (2023) 8311.
- [153]Y. Li, J. Chen, Y. Ji, Z. Zhao, W. Cui, X. Sang, Y. Cheng, B. Yang, Z. Li, Q. Zhang, L. Lei, Z. Wen, L. Dai, Y. Hou, Single-atom iron catalyst with biomimetic active center to accelerate proton spillover for medical-level electrosynthesis of H₂O₂ disinfectant, *Angew. Chem. Int. Ed.* 62 (2023) e202306491.
- [154]X. Zhou, Y. Min, C. Zhao, C. Chen, M.K. Ke, S.L. Xu, J.J. Chen, Y. Wu, H.Q. Yu, Constructing sulfur and oxygen super-coordinated main-group electrocatalysts for selective and cumulative H₂O₂ production, *Nat. Commun.* 15 (2024) 193.
- [155]P. Cao, X. Quan, X. Nie, K. Zhao, Y. Liu, S. Chen, H. Yu, J.G. Chen, Metal single-site catalyst design for electrocatalytic production of hydrogen peroxide at industrial-relevant currents, *Nat. Commun.* 14 (2023) 172.
- [156]R. Liu, Z. Wei, L. Peng, L. Zhang, A. Zohar, R. Schoepner, P. Wang, C. Wan, D. Zhu, H. Liu, Z. Wang, S.H. Tolbert, B. Dunn, Y. Huang, P. Sautet, X. Duan, Establishing reaction networks in the 16-electron sulfur reduction reaction, *Nature* 626 (2024) 98–104.
- [157]Y. Aniskevich, J.H. Yu, J.Y. Kim, S. Komaba, S.T. Myung, Tracking sodium cluster dynamics in hard carbon with a low specific surface area for sodium-ion batteries, *Adv. Energy Mater.* 14 (2024) 2304300.
- [158]W. Hua, T. Liu, Z. Zheng, H. Yuan, L. Xiao, K. Feng, J. Hui, Z. Deng, M. Ma, J. Cheng, D. Song, F. Lyu, J. Zhong, Y. Peng, Pulse electrolysis turns on CO₂ methanation through N-confused cupric porphyrin, *Angew. Chem. Int. Ed.* 63 (2024) e202315922.
- [159]J.F. Li, Y.F. Huang, Y. Ding, Z.L. Yang, S.B. Li, X.S. Zhou, F.R. Fan, W. Zhang, Z.Y. Zhou, D.Y. Wu, B. Ren, Z.L. Wang, Z.Q. Tian, Shell-isolated nanoparticle-enhanced Raman spectroscopy, *Nature* 464 (2010) 392–395.
- [160]D. Graham, The next generation of advanced spectroscopy: surface enhanced Raman scattering from metal nanoparticles, *Angew. Chem. Int. Ed.* 49 (2010) 9325–9327.
- [161]Z. Chen, S. Jiang, G. Kang, D. Nguyen, G.C. Schatz, R.P. Van Duyne, Operando characterization of iron phthalocyanine deactivation during oxygen reduction reaction using electrochemical tip-enhanced Raman spectroscopy, *J. Am. Chem. Soc.* 141 (2019) 15684–15692.
- [162]T. Zhao, J. Wang, Y. Wei, Z. Zhuang, Y. Dou, J. Yang, W.-H. Li, D. Wang, From lab-scale to industrialization: atomically M-N-C catalysts for oxygen reduction reaction, *Energy Environ. Sci.* 18

- (2025) 3462–3501.
- [163] Y.X. Du, Q. Yang, W.T. Lu, Q.Y. Guan, F.F. Cao, G. Zhang, Carbon black-supported single-atom Co-N-C as an efficient oxygen reduction electrocatalyst for H₂O₂ production in acidic media and microbial fuel cell in neutral media, *Adv. Funct. Mater.* 33 (2023) 2300895.
- [164] Q. Zhao, Y. Wang, W.H. Lai, F. Xiao, Y. Lyu, C. Liao, M. Shao, Approaching a high-rate and sustainable production of hydrogen peroxide: Oxygen reduction on Co-N-C single-atom electrocatalysts in simulated seawater, *Energy Environ. Sci.* 14 (2021) 5444–5456.
- [165] Z. Lin, Q. Zhang, J. Pan, C. Tsounis, A.A. Esmailpour, S. Xi, H.Y. Yang, Z. Han, J. Yun, R. Amal, X. Lu, Atomic Co decorated free-standing graphene electrode assembly for efficient hydrogen peroxide production in acid, *Energy Environ. Sci.* 15 (2022) 1172–1182.
- [166] Y. Chen, C. Zhen, Y. Chen, H. Zhao, Y. Wang, Z. Yue, Q. Wang, J. Li, M.D. Gu, Oxygen functional groups regulate cobalt-porphyrin molecular electrocatalyst for acidic H₂O₂ electrosynthesis at industrial-level current, *Angew. Chem. Int. Ed.* 63 (2024) e202407163.
- [167] L. Liu, L. Kang, J. Feng, D.G. Hopkinson, C.S. Allen, Y. Tan, H. Gu, I. Mikulska, V. Celorrio, D. Gianolio, T. Wang, L. Zhang, K. Li, J. Zhang, J. Zhu, G. Held, P. Ferrer, D. Grinter, J. Callison, M. Wilding, S. Chen, I. Parkin, Atomically dispersed asymmetric cobalt electrocatalyst for efficient hydrogen peroxide production in neutral media, *Nat. Commun.* 15 (2024) 4079.
- [168] W. Fan, Z. Duan, W. Liu, R. Mehmood, J. Qu, Y. Cao, X. Guo, J. Zhong, F. Zhang, Rational design of heterogenized molecular phthalocyanine hybrid single-atom electrocatalyst towards two-electron oxygen reduction, *Nat. Commun.* 14 (2023) 1426.
- [169] W. Zhang, J.W. Choi, S. Kim, T.T. Le, S. Nandy, C.K. Hwang, S.Y. Paek, A. Byeon, K.H. Chae, S.Y. Lee, S.H. Kim, H. Song, J. Kim, J. Oh, J.W. Lee, S.S. Han, J.M. Kim, Penta nitrogen coordinated cobalt single atom catalysts with oxygenated carbon black for electrochemical H₂O₂ production, *Appl. Catal. B Environ.* 331 (2023) 122712.
- [170] J. Liu, Z. Wei, Z. Gong, M. Yan, Y. Hu, S. Zhao, G. Ye, H. Fei, Single-atom CoN₄ sites with elongated bonding induced by phosphorus doping for efficient H₂O₂ electrosynthesis, *Appl. Catal. B Environ.* 324 (2023) 122267.
- [171] C. Liu, Z. Yu, F. She, J. Chen, F. Liu, J. Qu, J.M. Cairney, C. Wu, K. Liu, W. Yang, H. Zheng, Y. Chen, H. Li, L. Wei, Heterogeneous molecular Co-N-C catalysts for efficient electrochemical H₂O₂ synthesis, *Energy Environ. Sci.* 16 (2022) 446–459.
- [172] W. Liu, R. Chen, Z. Sang, Z. Li, J. Nie, L. Yin, F. Hou, J. Liang, A generalized coordination engineering strategy for single-atom catalysts toward efficient hydrogen peroxide electrosynthesis, *Adv. Mater.* 36 (2024) 2406403.
- [173] Z. Li, J. Jia, Z. Sang, W. Liu, J. Nie, L. Yin, F. Hou, J. Liu, J. Liang, A computation-guided design of highly defined and dense bimetallic active sites on a two-dimensional conductive metal-organic framework for efficient H₂O₂ electrosynthesis, *Angew. Chem. Int. Ed.* 63 (2024) e202408500.
- [174] Y. Sun, K. Fan, J. Li, L. Wang, Y. Yang, Z. Li, M. Shao, X. Duan, Boosting electrochemical oxygen reduction to hydrogen peroxide coupled with organic oxidation, *Nat. Commun.* 15 (2024) 6098.
- [175] B. Yue, L. Lin, Y. Lei, H. Xie, Y. Si, Q. Yang, X. Liu, O. N coordination-mediated nickel single-atom catalysts for high-efficiency generation of H₂O₂, *ACS Appl. Mater. Interfaces* 15 (2023) 33665–33674.
- [176] Y. Wu, Y. Ding, X. Han, B. Li, Y. Wang, S. Dong, Q. Li, S. Dou, J. Sun, J. Sun, Modulating coordination environment of Fe single atoms for high-efficiency all-pH-tolerated H₂O₂ electrochemical production, *Appl. Catal. B Environ.* 315 (2022) 121578.
- [177] Z. Zhang, W. Chen, H.K. Chu, F. Xiong, K. Zhang, H. Yan, F. Meng, S. Gao, B. Ma, X. Hai, R. Zou, Fe-O₄ motif activated graphitic carbon via oxo-bridge for highly selective H₂O₂ electrosynthesis, *Angew. Chem. Int. Ed.* 63 (2024) e202410123.
- [178] Y. Jia, Z. Xue, J. Yang, Q. Liu, J. Xian, Y. Zhong, Y. Sun, X. Zhang, Q. Liu, D. Yao, G. Li, Tailoring the electronic structure of an atomically dispersed zinc electrocatalyst: coordination environment regulation for high selectivity oxygen reduction, *Angew. Chem. Int. Ed.* 61 (2022) e202110838.
- [179] C. Tang, Y. Jiao, B. Shi, J.N. Liu, Z. Xie, X. Chen, Q. Zhang, S.Z. Qiao, Coordination tunes selectivity: two-electron oxygen reduction on high-loading molybdenum single-atom catalysts, *Angew. Chem. Int. Ed.* 59 (2020) 9171–9176.
- [180] P. Zhu, W. Feng, D. Zhao, P. Song, M. Li, X. Tan, T. Liu, S. Liu, W. Zhu, Z. Zhuang, J. Zhang, C. Chen, P-block bismuth nanoclusters sites activated by atomically dispersed bismuth for tandem boosting electrocatalytic hydrogen peroxide production, *Angew. Chem. Int. Ed.* 135 (2023) e202304488.
- [181] M. Yan, Z. Wei, Z. Gong, B. Johannessen, G. Ye, G. He, J. Liu, S. Zhao, C. Cui, H. Fei, Sb₂S₃-templated

- synthesis of sulfur-doped Sb-N-C with hierarchical architecture and high metal loading for H₂O₂ electrosynthesis, *Nat. Commun.* 14 (2023) 368.
- [182] X. Wang, Z. Li, Y. Qu, T. Yuan, W. Wang, Y. Wu, Y. Li, Review of metal catalysts for oxygen reduction reaction: from nanoscale engineering to atomic design, *Chem* 5 (2019) 1486–1511.
- [183] H.Y. Zhuo, X. Zhang, J.X. Liang, Q. Yu, H. Xiao, J. Li, Theoretical understandings of graphene-based metal single-atom catalysts: stability and catalytic performance, *Chem. Rev.* 120 (2020) 12315–12341.
- [184] W. Liu, C. Zhang, J. Zhang, X. Huang, M. Song, J. Li, F. He, H. Yang, J. Zhang, D. Wang, Tuning the atomic configuration of Co-N-C electrocatalyst enables highly-selective H₂O₂ production in acidic media, *Appl. Catal. B Environ.* 310 (2022) 121312.
- [185] X. Song, N. Li, H. Zhang, L. Wang, Y. Yan, H. Wang, L. Wang, Z. Bian, Graphene-supported single nickel atom catalyst for highly selective and efficient hydrogen peroxide production, *ACS Appl. Mater. Interfaces* 12 (2020) 17519–17527.
- [186] K. Jiang, S. Back, A.J. Akey, C. Xia, Y. Hu, W. Liang, D. Schaak, E. Stavitski, J.K. Nørskov, S. Siahrostami, H. Wang, Highly selective oxygen reduction to hydrogen peroxide on transition metal single atom coordination, *Nat. Commun.* 10 (2019) 3997.
- [187] J. Suntivich, H.A. Gasteiger, N. Yabuuchi, H. Nakanishi, J.B. Goodenough, Y. Shao-Horn, Design principles for oxygen-reduction activity on perovskite oxide catalysts for fuel cells and metal-air batteries, *Nat. Chem.* 3 (2011) 546–550.
- [188] X. Cheng, J. Hu, W. Shang, J. Guo, C. Xin, S. Zhang, S. Song, W. Liu, Y. Shi, Asymmetrically ligated single atomic nickel sites for efficient hydrogen peroxide electrosynthesis, *Nano Res.* 17 (2024) 1094–1100.
- [189] M. Zhang, J. Huang, C. Liang, X. Chen, P. Liao, Continuous electrosynthesis of pure H₂O₂ solution with medical-grade concentration by a conductive Ni-phthalocyanine-based covalent organic framework, *J. Am. Chem. Soc.* 146 (2024) 31034–31041.
- [190] H. Hu, Y. Meng, Y. Mei, P.X. Hou, C. Liu, H.M. Cheng, M. Shao, J.C. Li, Bifunctional oxygen electrocatalysts enriched with single Fe atoms and NiFe₂O₄ nanoparticles for rechargeable zinc–air batteries, *Energy Storage Mater.* 54 (2023) 517–523.
- [191] W. Xia, Z. Hou, J. Tang, J. Li, W. Chaikittisilp, Y. Kim, K. Muraoka, H. Zhang, J. He, B. Han, Y. Yamauchi, Materials informatics-guided superior electrocatalyst: A case of pyrolysis-free single-atom coordinated with N-graphene nanomesh, *Nano Energy* 94 (2022) 106868.
- [192] S. Kattel, G. Wang, Reaction pathway for oxygen reduction on FeN₄ embedded graphene, *J. Phys. Chem. Lett.* 5 (2014) 452–456.
- [193] C.H. Choi, W.S. Choi, O. Kasian, A.K. Mechler, M.T. Sougrati, S. Brüller, K. Strickland, Q. Jia, S. Mukerjee, K.J.J. Mayrhofer, F. Jaouen, Unraveling the nature of sites active toward hydrogen peroxide reduction in Fe-N-C catalysts, *Angew. Chem. Int. Ed.* 56 (2017) 8809–8812.
- [194] X. Li, H. Rong, J. Zhang, D. Wang, Y. Li, Modulating the local coordination environment of single-atom catalysts for enhanced catalytic performance, *Nano Res.* 13 (2020) 1842–1855.
- [195] X. Li, Y. Huang, B. Liu, Catalyst: single-atom catalysis: directing the way toward the nature of catalysis, *Chem* 5 (2019) 2733–2735.
- [196] J. Li, S. Chen, N. Yang, M. Deng, S. Ibraheem, J. Deng, J. Li, L. Li, Z. Wei, Ultrahigh-loading zinc single-atom catalyst for highly efficient oxygen reduction in both acidic and alkaline media, *Angew. Chem. Int. Ed.* 58 (2019) 7035–7039.
- [197] G. Wei, X. Liu, Z. Zhao, C. Men, Y. Ding, S. Gao, Constructing ultrahigh-loading unsymmetrically coordinated Zn-N₃O single-atom sites with efficient oxygen reduction for H₂O₂ production, *Chem. Eng. J.* 455 (2023) 140721.
- [198] J. Li, M. Chen, D.A. Cullen, S. Hwang, M. Wang, B. Li, K. Liu, S. Karakalos, M. Lucero, H. Zhang, C. Lei, H. Xu, G.E. Sterbinsky, Z. Feng, D. Su, K.L. More, G. Wang, Z. Wang, G. Wu, Atomically dispersed manganese catalysts for oxygen reduction in proton-exchange membrane fuel cells, *Nat. Catal.* 1 (2018) 935–945.
- [199] H. Shang, W. Sun, R. Sui, J. Pei, L. Zheng, J. Dong, Z. Jiang, D. Zhou, Z. Zhuang, W. Chen, J. Zhang, D. Wang, Y. Li, Engineering isolated Mn-N₂C₂ atomic interface sites for efficient bifunctional oxygen reduction and evolution reaction, *Nano Lett.* 20 (2020) 5443–5450.
- [200] Y. Gu, Y. Tan, H. Tan, Y. Han, D. Cheng, F. Lin, Z. Qian, L. Zeng, S. Zhang, R. Zeng, Y. Liu, H. Guo, M. Luo, S. Guo, Industrial electrosynthesis of hydrogen peroxide over p-block metal single sites, *Nat. Synth.* 4 (2025) 614–621.
- [201] L. Li, K. Yuan, Y. Chen, Breaking the scaling relationship limit: from single-atom to dual-Atom

- catalysts, *Accounts Mater. Res.* 3 (2022) 584–596.
- [202] Q. An, X. Qin, X. Sun, X. Zhang, Y. Zhang, J. Guo, J. Jiang, J. Zhang, B. Li, Y. Jiang, H. Zhang, X. Chen, Y. Li, K. Zheng, W. Cheng, D. Wang, Q. Liu, In situ identification of zinc sites as potential-dependent selectivity switch over dual-atom catalysts for H_2O_2 electrosynthesis, *J. Am. Chem. Soc.* 147 (2025) 11465–11476.
- [203] H. Huang, M. Sun, S. Li, S. Zhang, Y. Lee, Z. Li, J. Fang, Enhancing H_2O_2 electrosynthesis at industrial-relevant current in acidic media on diatomic cobalt sites, *J. Am. Chem. Soc.* 146 (2024) 9434–9443.
- [204] J. Du, G. Han, W. Zhang, L. Li, Y. Yan, Y. Shi, X. Zhang, L. Geng, Z. Wang, Y. Xiong, G. Yin, C. Du, CoIn dual-atom catalyst for hydrogen peroxide production via oxygen reduction reaction in acid, *Nat. Commun.* 14 (2023) 4766.
- [205] Y. Gao, B. Liu, D. Wang, Microenvironment engineering of single/dual-atom catalysts for electrocatalytic application, *Adv. Mater.* 35 (2023) 2209654.
- [206] M. Yang, W. Song, C. Chen, X. Yang, Z. Zhuang, H. Zhang, F. Wang, L. Yu, Atomically dispersed Co/Mo sites anchored on mesoporous carbon hollow spheres for highly selective oxygen reduction to hydrogen peroxide in acidic media, *Adv. Mater.* (2025) 2416401.
- [207] S. Yang, Y.J. Tak, J. Kim, A. Soon, H. Lee, Support effects in single-atom platinum catalysts for electrochemical oxygen reduction, *ACS Catal.* 7 (2017) 1301–1307.
- [208] Y. Peng, B. Lu, S. Chen, Carbon-supported single atom catalysts for electrochemical energy conversion and storage, *Adv. Mater.* 30 (2018) 1801995.
- [209] J.M. Thomas, R. Raja, D.W. Lewis, Single-site heterogeneous catalysts, *Angew. Chem. Int. Ed.* 44 (2005) 6456–6482.
- [210] W. Yuan, Y. Zhou, Y. Li, C. Li, H. Peng, J. Zhang, Z. Liu, L. Dai, G. Shi, The edge- and basal-plane-specific electrochemistry of a single-layer graphene sheet, *Sci. Rep.* 3 (2013) 2248.
- [211] B.W. Zhang, T. Zheng, Y.X. Wang, Y. Du, S.Q. Chu, Z. Xia, R. Amal, S.X. Dou, L. Dai, Highly efficient and selective electrocatalytic hydrogen peroxide production on Co-O-C active centers on graphene oxide, *Commun. Chem.* 5 (2022) 43.
- [212] J. Lee, J. Kim, T. Hyeon, Recent progress in the synthesis of porous carbon materials, *Adv. Mater.* 18 (2006) 2073–2094.
- [213] H.J. Qiu, Y. Ito, W. Cong, Y. Tan, P. Liu, A. Hirata, T. Fujita, Z. Tang, M. Chen, Nanoporous graphene with single-atom nickel dopants: an efficient and stable catalyst for electrochemical hydrogen production, *Angew. Chem. Int. Ed.* 54 (2015) 14031–14035.
- [214] D. San Roman, D. Krishnamurthy, R. Garg, H. Hafiz, M. Lamparski, N.T. Nuhfer, V. Meunier, V. Viswanathan, T. Cohen-Karni, Engineering three-dimensional (3d) out-of-plane graphene edge sites for highly selective two-electron oxygen reduction electrocatalysis, *ACS Catal.* 10 (2020) 1993–2008.
- [215] Y. Wu, H. Ma, Y. Feng, Z. Shi, Y. Yi, Y. Ding, J. Feng, W. Zhao, J. Sun, S. Dong, J. Sun, Harnessing optimized surface reconstruction of single-atom Ni-doped Ni-NiO/NC precatalysts toward robust H_2O_2 production, *ACS Appl. Mater. Interfaces* 14 (2022) 26803–26813.
- [216] H. Li, W. Wang, S. Xue, J. He, C. Liu, G. Gao, S. Di, S. Wang, J. Wang, Z. Yu, L. Li, Superstructure-assisted single-atom catalysis on tungsten carbides for bifunctional oxygen reactions, *J. Am. Chem. Soc.* 146 (2024) 9124–9133.
- [217] D. Zhu, H. Wu, W.-K. Fong, R.F. Tabor, J. Zhang, The ratio of sp^2 and sp^3 hybridized carbon determines the performance of carbon-based catalysts in H_2O_2 electrosynthesis from O_2 , *Angew. Chem. Int. Ed.* 64 (2025) e202500145.
- [218] H. Shen, N. Qiu, L. Yang, X. Guo, K. Zhang, T. Thomas, S. Du, Q. Zheng, J.P. Attfield, Y. Zhu, M. Yang, Boosting oxygen reduction for high-efficiency H_2O_2 electrosynthesis on oxygen-coordinated Co-N-C catalysts, *Small* 18 (2022) 2200730.
- [219] G. Wu, Z. Yang, T. Zhang, Y. Sun, C. Long, Y. Song, Enhancing electrocatalytic production of H_2O_2 by modulating coordination environment of cobalt center, *Bull. Korean Chem. Soc.* 42 (2021) 1155–1160.
- [220] L. Runze, W. Dingsheng, Understanding the structure-performance relationship of active sites at atomic scale, *Nano Res.* 15 (2022) 6888–6923.
- [221] E. Zhang, L. Tao, J. An, J. Zhang, L. Meng, X. Zheng, Y. Wang, N. Li, S. Du, J. Zhang, D. Wang, Y. Li, Engineering the local atomic environments of indium single-atom catalysts for efficient electrochemical production of hydrogen peroxide, *Angew. Chem. Int. Ed.* 61 (2022) e202117347.
- [222] Q. Zhi, R. Jiang, X. Yang, Y. Jin, D. Qi, K. Wang, Y. Liu, J. Jiang, Dithiine-linked metalphthalocyanine framework with undulated layers for highly efficient and stable H_2O_2 electroproduction, *Nat. Commun.*

- 15 (2024) 678.
- [223] Y. Yao, Z. Huang, P. Xie, L. Wu, L. Ma, T. Li, Z. Pang, M. Jiao, Z. Liang, J. Gao, Y. He, D.J. Kline, M.R. Zachariah, C. Wang, J. Lu, T. Wu, T. Li, C. Wang, R. Shahbazian-Yassar, L. Hu, High temperature shockwave stabilized single atoms, *Nat. Nanotechnol.* 14 (2019) 851–857.
- [224] I. Slobodkin, E. Davydova, M. Sananis, A. Breytus, A. Rothschild, Electrochemical and chemical cycle for high-efficiency decoupled water splitting in a near-neutral electrolyte, *Nat. Mater.* 23 (2024) 398–405.
- [225] M. Xia, H. Fu, K. Lin, A.M. Rao, L. Cha, H. Liu, J. Zhou, C. Wang, B. Lu, Hydrogen-bond regulation in organic/aqueous hybrid electrolyte for safe and high-voltage K-ion batteries, *Energy Environ. Sci.* 17 (2024) 1255–1265.
- [226] S. Rojas-Carbonell, K. Artyushkova, A. Serov, C. Santoro, I. Matanovic, P. Atanassov, Effect of pH on the activity of platinum group metal-free catalysts in oxygen reduction reaction, *ACS Catal.* 8 (2018) 3041–3053.
- [227] B.Q. Li, C.X. Zhao, J.N. Liu, Q. Zhang, Electrosynthesis of hydrogen peroxide synergistically catalyzed by atomic Co–N_x–C Sites and oxygen functional groups in noble-metal-free electrocatalysts, *Adv. Mater.* 31 (2019) 1808173.
- [228] Z. Qiang, J.H. Chang, C.P. Huang, Electrochemical generation of hydrogen peroxide from dissolved oxygen in acidic solutions, *Water Res.* 36 (2002) 85–94.
- [229] H.B. Tao, J. Zhang, J. Chen, L. Zhang, Y. Xu, J.G. Chen, B. Liu, Revealing energetics of surface oxygen redox from kinetic fingerprint in oxygen electrocatalysis, *J. Am. Chem. Soc.* 141 (2019) 13803–13811.
- [230] C. Dong, K.S. Lee, Y. Cho, S.P. Wang, X.W. Fan, F.Q. Bai, J.H. Park, K. Zhang, Precise synthesis of single-atom Mo, W, Nb coordinated with oxygen functional groups of graphene oxide for stable and selective two-electron oxygen reduction in neutral media, *J. Mater. Chem. A* 10 (2022) 9488–9496.
- [231] X. Wei, S. Song, N. Wu, X. Luo, L. Zheng, L. Jiao, H. Wang, Q. Fang, L. Hu, W. Gu, W. Song, C. Zhu, Synergistically enhanced single-atomic site Fe by Fe₃C@C for boosted oxygen reduction in neutral electrolyte, *Nano Energy* 84 (2021) 105840.
- [232] L. Zhang, L. Han, H. Liu, X. Liu, J. Luo, Potential-cycling synthesis of single platinum atoms for efficient hydrogen evolution in neutral media, *Angew. Chem. Int. Ed.* 56 (2017) 13694–13698.
- [233] U.A. Paulus, T.J. Schmidt, H.A. Gasteiger, R.J. Behm, Oxygen reduction on a high-surface area Pt/vulcan carbon catalyst: a thin-film rotating ring-disk electrode study, *J. Electroanal. Chem.* 495 (2001) 134–145.
- [234] E. Pizzutilo, O. Kasian, C.H. Choi, S. Cherevko, G.J. Hutchings, K.J.J. Mayrhofer, S.J. Freakley, Electrocatalytic synthesis of hydrogen peroxide on Au-Pd nanoparticles: from fundamentals to continuous production, *Chem. Phys. Lett.* 683 (2017) 436–442.
- [235] I. Yamanaka, T. Onizawa, S. Takenaka, K. Otsuka, Direct and continuous production of hydrogen peroxide with 93% selectivity using a fuel-cell system, *Angew. Chem. Int. Ed.* 42 (2003) 3653–3655.
- [236] H. Sheng, A.N. Janes, R.D. Ross, D. Kaiman, J. Huang, B. Song, J.R. Schmidt, S. Jin, Stable and selective electrosynthesis of hydrogen peroxide and the electro-Fenton process on CoSe₂ polymorph catalysts, *Energy Environ. Sci.* 13 (2020) 4189–4203.
- [237] Y. Xia, H. Shang, Q. Zhang, Y. Zhou, X. Hu, Electrogenation of hydrogen peroxide using phosphorus-doped carbon nanotubes gas diffusion electrodes and its application in electro-Fenton, *J. Electroanal. Chem.* 840 (2019) 400–408.
- [238] J.F. Pérez, J. Llanos, C. Sáez, C. López, P. Cañizares, M.A. Rodrigo, Electrochemical jet-cell for the in-situ generation of hydrogen peroxide, *Electrochem. Commun.* 71 (2016) 65–68.
- [239] X. Lu, M. Zhou, Y. Li, P. Su, J. Cai, Y. Pan, Improving the yield of hydrogen peroxide on gas diffusion electrode modified with tert-butyl-anthraquinone on different carbon support, *Electrochim. Acta* 320 (2019) 134552.
- [240] Y.C. Li, D. Zhou, Z. Yan, R.H. Gonçalves, D.A. Salvatore, C.P. Berlinguette, T.E. Mallouk, Electrolysis of CO₂ to syngas in bipolar membrane-based electrochemical cells, *ACS Energy Lett.* 1 (2016) 1149–1153.
- [241] E. Jung, H. Shin, W. Hooch Antink, Y.E. Sung, T. Hyeon, Recent advances in electrochemical oxygen reduction to H₂O₂: catalyst and cell design, *ACS Energy Lett.* 5 (2020) 1881–1892.
- [242] P. Millet, R. Ngameni, S.A. Grigoriev, N. Mbemba, F. Brisset, A. Ranjbari, C. Etiévant, PEM water electrolyzers: From electrocatalysis to stack development, *Int. J. Hydrogen Energy.* 35 (2010) 5043–5052.
- [243] C. Xia, Y. Xia, P. Zhu, L. Fan, H. Wang, Direct electrosynthesis of pure aqueous H₂O₂ solutions up to

- 20% by weight using a solid electrolyte, *Science* 366 (2019) 226–231.
- [244] B. Sabri Rawah, M. Albloushi, W. Li, Electro-synthesis of pure aqueous H_2O_2 on nitrogen-doped carbon in a solid electrolyte flow cell without using anion exchange membrane, *Chem. Eng. J.* 466 (2023) 143282.
- [245] Y. Zhao, N. Deng, Z. Fan, Z.T. Hu, L. Fan, J. Zhou, X. Huang, On-site H_2O_2 electro-generation process combined with ultraviolet: A promising approach for odorous compounds purification in drinking water system, *Chem. Eng. J.* 430 (2022) 132829.
- [246] X. Zhang, X. Zhao, P. Zhu, Z. Adler, Z.Y. Wu, Y. Liu, H. Wang, Electrochemical oxygen reduction to hydrogen peroxide at practical rates in strong acidic media, *Nat. Commun.* 13 (2022) 2880.
- [247] Q. Zhang, C. Cao, S. Zhou, W. Wei, X. Chen, R. Xu, X.T. Wu, Q.L. Zhu, Bifunctional oxygen-defect bismuth catalyst toward concerted production of H_2O_2 with over 150% cell faradaic efficiency in continuously flowing paired-electrosynthesis system, *Adv. Mater.* 36 (2024) 2408341.
- [248] K. Otsuka, I. Yamanaka, One step synthesis of hydrogen peroxide through fuel cell reaction, *Electrochim. Acta* 35 (1990) 319–322.
- [249] N. Yamada, T. Yaguchi, H. Otsuka, M. Sudoh, Development of trickle-bed electrolyzer for on-Site electrochemical production of hydrogen peroxide, *J. Electrochem. Soc.* 146 (1999) 2587–2591.
- [250] M. Tawalbeh, S. Alarab, A. Al-Othman, R.M.N. Javed, The operating parameters, structural composition, and fuel sustainability aspects of PEM fuel cells: a mini review, *Fuels* 3 (2022) 449–474.
- [251] C. Kim, S.O. Park, S.K. Kwak, Z. Xia, G. Kim, L. Dai, Concurrent oxygen reduction and water oxidation at high ionic strength for scalable electrosynthesis of hydrogen peroxide, *Nat. Commun.* 14 (2023) 5822.
- [252] C.K. Hwang, S. Kim, K.R. Yoon, T.T. Le, C. V. Hoang, J.W. Choi, W. Zhang, S.Y. Paek, C.H. Lee, J.H. Lee, K.H. Chae, S. Jeong, S.Y. Lee, B.K. Ju, S.H. Kim, S.S. Han, J.M. Kim, Arc plasma-deposited Co single-atom catalysts supported on an aligned carbon nanofiber for hydrogen peroxide electrosynthesis and an electro-Fenton process, *Carbon Energy* 6 (2024) e582.
- [253] L. Yang, H. Cheng, H. Li, G. Sun, S. Liu, T. Ma, L. Zhang, Atomic confinement empowered CoZn dual-single-atom nanotubes for H_2O_2 production in sequential dual-cathode electro-Fenton process, *Adv. Mater.* 36 (2024) 2406957.
- [254] K. Zhao, X. Quan, Y. Su, X. Qin, S. Chen, H. Yu, Enhanced chlorinated pollutant degradation by the synergistic effect between dechlorination and hydroxyl radical oxidation on a bimetallic single-atom catalyst, *Environ. Sci. Technol.* 55 (2021) 14194–14203.
- [255] L. Jing, Q. Tian, P. Su, H. Li, Y. Zheng, C. Tang, J. Liu, Mesoporous Co-O-C nanosheets for electrochemical production of hydrogen peroxide in acidic medium, *J. Mater. Chem. A* 10 (2022) 4068–4075.
- [256] L. Xin, J. Hu, Y. Xiang, C. Li, L. Fu, Q. Li, X. Wei, Carbon-based nanocomposites as Fenton-like catalysts in wastewater treatment applications: A review, *Materials* 14 (2021) 2643.
- [257] J. Feng, C. Chu, Z. Ma, Fenton and Fenton-like catalysts for electrochemical immunoassay: A mini review, *Electrochem. Commun.* 125 (2021) 106970.
- [258] W. Wu, L. Huang, Y. Li, M. Li, Y. Chen, Y. Yang, X. Chen, Y. Wu, L. Gu, X. Cao, On-site production of dilute H_2O_2 with zinc–air battery, *Adv. Mater. Technol.* 7 (2022) 2100708.
- [259] J. Fu, R. Liang, G. Liu, A. Yu, Z. Bai, L. Yang, Z. Chen, Recent progress in electrically rechargeable zinc–air batteries, *Adv. Mater.* 31 (2019) 1805230.
- [260] Z.W. She, J. Kibsgaard, C.F. Dickens, I. Chorkendorff, J.K. Nørskov, T.F. Jaramillo, Combining theory and experiment in electrocatalysis: Insights into materials design, *Science* 355 (2017) eaad4998.
- [261] B.Y. Xia, Y. Yan, N. Li, H. Bin Wu, X.W.D. Lou, X. Wang, A metal-organic framework-derived bifunctional oxygen electrocatalyst, *Nat. Energy* 1 (2016) 15006.
- [262] W. Sun, F. Wang, B. Zhang, M. Zhang, V. Küpers, X. Ji, C. Theile, P. Bieker, K. Xu, C. Wang, M. Winter, A rechargeable zinc-air battery based on zinc peroxide chemistry, *Science* 371 (2021) 46–51.
- [263] W. Zhang, J. Zhang, N. Wang, K. Zhu, C. Yang, Y. Ai, F. Wang, Y. Tian, Y. Ma, Y. Ma, X. Zhang, L. Duan, D. Chao, F. Wang, D. Zhao, W. Li, Two-electron redox chemistry via single-atom catalyst for reversible zinc–air batteries, *Nat. Sustain.* 7 (2024) 463–473.
- [264] H. Wang, J. Zhan, W. Yao, B. Wang, S. Deng, J. Huang, G. Yu, Y. Wang, Comparison of pharmaceutical abatement in various water matrices by conventional ozonation, peroxone ($\text{O}_3/\text{H}_2\text{O}_2$), and an electro-peroxone process, *Water Res.* 130 (2018) 127–138.
- [265] S. Sun, M. Qiao, G. Huang, J. Zhang, B. Yang, X. Zhao, An electrochlorination process integrating enhanced oxidation of phosphonate to orthophosphate and elimination: Verification of matrix

- chloridion-induced oxidation mechanism, *Water Res.* 249 (2024) 120735.
- [266]J. Zhang, X. Zhao, Y. Wang, R. Djellabi, Recovery of phosphorus from hypophosphite-laden wastewater: a single-compartment photoelectrocatalytic cell system integrating oxidation and precipitation, *Environ. Sci. Technol.* 54 (2020) 1204–1213.
- [267]G. Yu, D.H. Mok, H.Y. Jang, H.D. Jung, S. Siahrostami, S. Back, Leveraging machine learning and active motifs-based catalyst design for discovery of oxygen reduction electrocatalysts for hydrogen peroxide production, *J. Catal.* 442 (2025) 115906.
- [268]Y. Yang, X. Lin, Y. Lin, Z. Zhuo, The geometric-electronic coupled design of diatomic catalyst towards oxygen reduction reaction, *Nat. Commun.* 16 (2025) 5158.

- The principles underlying direct H₂O₂ production are examined.
- The synthesis approaches and characterization techniques for M–N–C SAECs are analyzed.
- The structural characteristics of M–N–C SAECs are explored.
- The optimizing reactors for enhancing H₂O₂ electrosynthesis are emphasized.
- Barriers in transitioning from laboratory to real-world applications are addressed with future perspectives.

The authors declare that they have no known competing financial interests or personal relationships that could have appeared to influence the work reported in this paper.